An improved estimation of the Mars rotation and orientation parameters from the Doppler observables of the InSight-RISE and ExoMars-LaRa landers

Master's Thesis

Carlos Fortuny Lombraña

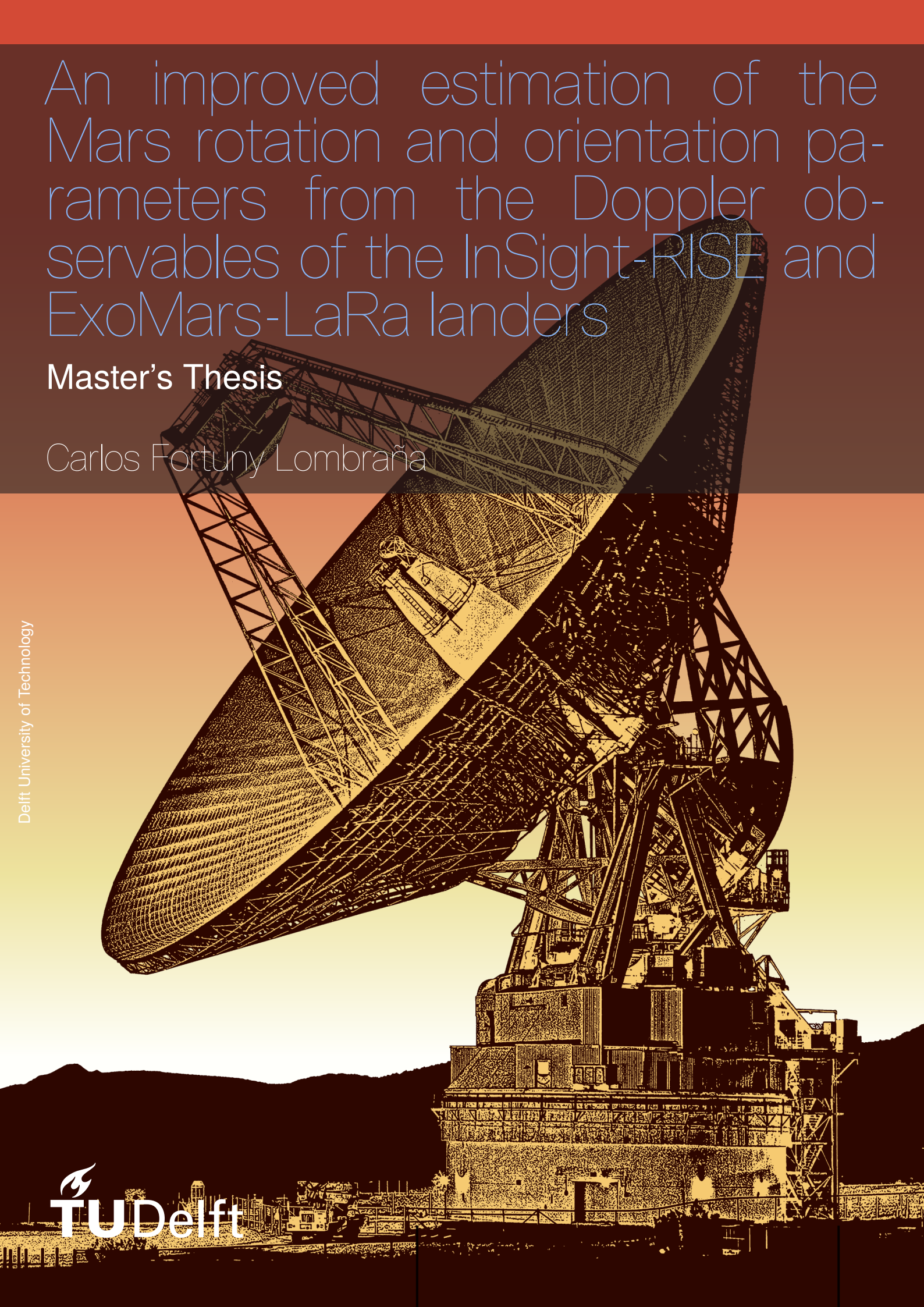

Delft University of Technology

TU Delft

An improved estimation of the Mars rotation and orientation parameters from the Doppler observables of the InSight-RISE and ExoMars-LaRa landers

Master's Thesis

by

Carlos Fortuny Lombraña

to obtain the degree of Master of Science
at the Delft University of Technology,
to be defended publicly on **Monday 26th September** at **9:30 AM**.

Student Number:	4651138	
Duration:	September, 2021 - September, 2022	
Institution:	Delft University of Technology	
Thesis Committee:	Dr. Ir. Stephanie Cazaux	Chair
	Dr. Ir. Jian Guo	Examiner
	Dr. Ir. Dominic Dirkx	Daily supervisor

An electronic version of this thesis is available at http://repository.tudelft.nl/.

Cover Image: Schematic representation of a NASA's Deep Space Network antenna taken from https://www.nasa.gov/directorates/heo/scan/services/networks/deep_space_network/students/resources/wallpaper/

TU Delft

Preface

This report marks the end of a very long journey in Delft. Here, I have loved my marvelous time surrounded by extraordinary people, and I am very very proud of all the knowledge I have acquired along this Dutch adventure.

All this *tough grind* owes much to the people with that I had the satisfaction to live and work with. Above all, I want to express my recognition to my supervisor, Dominic, for offering this fascinating opportunity. After an entire academic year of strong cooperation, I must confess that this research without your exceptional insights and guidance would have not been the same at all! Additionally, I really appreciate all the helpful feedback given and the time spent to double-check everything that I have written.

Moreover, I could not have completed this Master's thesis and achieved the M.Sc. Diploma without all those people who have contributed to the development of this dissertation: Giuseppe Cimo', Leonid Gurvits, Sebastien Le Maistre, and Marie Fayolle-Chambe. All of you have pushed and encouraged me to do better, and I am so thankful to have joined such a top-notch team. Thanks indeed for all the patience and valuable discussions we had.

Undoubtedly, this work would have not been the same with all my friends. I want to give a special thanks to all my lifelong *fellas*, my roommates, and Master's room group (Room 2.44 LR). In this Dutch chapter, we shared wonderful moments that I will always remember and never forget about them.

Last but not least, my father Joaquim, my mother Maria José, my sibling Marta, and all of my family members deserve particular love and honor for all the stimulation and support (in all possible ways that you can think of!) they brought to this hard work. I have no words, and I can not thank you enough for all this. I am beyond grateful!

Carlos Fortuny Lombraña
Delft, September 2022

Abstract

The Planetary Radio Interferometry and Doppler Experiment (PRIDE) technique has supported the exploitation of Doppler observations of planetary landers from Earth-based stations in many radio science experiments. The precise retrieval of the estimates of the Mars rotation and Orientation Parameters (MOPs) is an important application of the PRIDE technique and is the subject of this work. The MOPs that are retrieved can be related to four motions: the polar motion, variations of the rotation rate, precession, and nutation. More precisely, the MOPs analyzed consist of a total of 30 parameters that characterizes all the motion components, including: the core factor F, the free core nutation rate σ_{FCN}, 8 spin variation parameters (ϕ_m^c, ϕ_m^s) and 20 polar motion parameters ($X_{p_m}^{\ c}$, $X_{p_m}^{\ s}$, $Y_{p_m}^{\ c}$ and $Y_{p_m}^{\ s}$). Properties related to the internal structure of the Red planet can be deduced from these parameters.

The aim of this work is to reduce the MOPs uncertainty and thus help identify the interplay and signatures of the different parameters, which in turn will provide a better understanding of the state and composition of the Martian inner core. In this context, it is required a thorough assessment of the benefits of combining the Doppler observations from the InSight-RISE and ExoMars-LaRa landers using an extended network of Earth-based stations, including 10 extra receive-only radio telescopes. The analysis has been conducted with TUDAT astrodynamical toolkit, where a high-accuracy Mars rotation model can be adopted, in order to simulate the formal errors of the MOPs.

The results obtained can be summarized as follows. The considered two-lander geometry configuration allows a more precise retrieval of the MOPs, with a reduction of more than 92 % overall on the MOPs uncertainty compared to a single-lander configuration. The combined exploitation of the RISE and LaRa Doppler observations allows a more efficient retrieval of the full set of the MOPs, and particularly, the polar motion parameters. Furthermore, the accuracy of the MOPs is additionally increased in a configuration with the 10 extra receive-only stations. The MOPs accuracy improvements observed in this case are, on average, a 12 % for the core factor F, a 10 % for the free core nutation rate σ_{FCN}, about 25 % for the polar motion parameters at the Chandler frequency, a 5 % for the spin variations, and a 15 % for the other polar motion amplitudes.

Contents

Preface i

Abstract ii

List of Figures v

List of Tables viii

List of Symbols and Abbreviations ix

1 Introduction 1
- 1.1 Background . . . 1
- 1.2 Research Questions . . . 2
- 1.3 Report Outline . . . 2

2 Journal Article 3

3 Conclusion and Future Work 25
- 3.1 Conclusions . . . 25
- 3.2 Recommendations for Future Work . . . 27

A Verification and Validation 30
- A.1 Preliminary Analysis . . . 30
- A.2 Estimated Parameters as a Function of the Correlation and the Number of Stations . . . 32
- A.3 Implementation of the Gaussian Noise . . . 36
- A.4 Correlation Coefficient . . . 37
  - A.4.1 Cross-correlation Fixed at 0.47 *versus* Variable Cross-correlation . . . 37
  - A.4.2 Cross-correlation Fixed at 0.99 *versus* not adding PRIDE Stations . . . 38

B Additional Results 40
- B.1 Preliminary Analysis of LaRa Measurements . . . 40
- B.2 Resolution of the Estimated Parameters . . . 43
- B.3 ED045 Experiment . . . 46
  - B.3.1 BADARY . . . 47
  - B.3.2 CEDUNA . . . 48
  - B.3.3 EFLSBERG . . . 49
  - B.3.4 HARTRAO . . . 50
  - B.3.5 IRBENE . . . 51
  - B.3.6 MEDICINA . . . 51
  - B.3.7 ONSALA60 . . . 52
  - B.3.8 TIANMA65 . . . 54
  - B.3.9 WRT0 . . . 55
  - B.3.10 WETTZELL . . . 56
  - B.3.11 YEBES40M . . . 57

C TUDAT Implementations **59**
C.1 Maximum Elevation Angle Viability 59
C.1.1 observationViabilityCalculator.h 59
C.1.2 createObservationViability.h 60
C.1.3 observationViabilityCalculator.cpp 62
C.1.4 createObservationViability.cpp 62
C.1.5 unitTestObservationViabilityCalculators.cpp 63
C.1.6 expose_observation_setup.cpp 64

List of Figures

A.1 Earth azimuth as seen by RISE as a function of Earth days after InSight landing (27th of November 2018). . . . 31
A.2 Earth elevation as seen by RISE as a function of Earth days after InSight landing (27th of November 2018). . . . 31
A.3 Earth elevation as seen by RISE as a function of Earth azimuth as seen by RISE. . . . 32
A.4 Elevation angle at DSN transmitter as a function of Earth days after InSight landing (27th of November 2018). . . . 32
A.5 Formal errors of the initial position state evaluated at the end of the ExoMars mission as a function of the covariance coefficent and number of ground stations. . . . 33
A.6 Formal errors of the initial velocity state evaluated at the end of the ExoMars mission as a function of the covariance coefficient and number of ground stations. . . . 33
A.7 Formal errors of the core factor and free core nutation rate evaluated at the end of the ExoMars mission as a function of the covariance coefficient and number of ground stations. 34
A.8 Formal errors of the lander position evaluated at the end of the ExoMars mission as a function of the covariance coefficient and number of ground stations. . . . 34
A.9 Formal errors of the spin variation parameters evaluated at the end of the ExoMars mission as a function of the covariance coefficient and number of ground stations. . . . 34
A.10 Formal errors of the polar motion parameters evaluated at the end of the ExoMars mission as a function of the covariance coefficient and number of ground stations. . . . 35
A.11 Normalized partial derivatives of the design matrix with respect to the ExoMars lander position as a function of Earth days after ExoMars landing (assumed to be 3rd of January 2022). . . . 36
A.12 $1-\sigma$, RMSE and μ of the Doppler residual. . . . 37

B.1 Earth azimuth as seen by LaRa as a function of Earth days after ExoMars landing (assumed to be 3rd of January 2022). . . . 40
B.2 Earth elevation as seen by LaRa as a function of Earth days after ExoMars landing (assumed to be 3rd of January 2022). . . . 41
B.3 Earth elevation as seen by LaRa as a function of Earth azimuth as seen by LaRa. . . . 41
B.4 Elevation angle at DSN transmitter as a function of Earth days after ExoMars landing (assumed to be 3rd of January 2022). . . . 42
B.5 Elevation angle at the receiving antennas as a function of Earth days after ExoMars landing (assumed to be 3rd of January 2022). . . . 42
B.6 Time instances when the radio signal reflected is received by the receivers (assumed to be 3rd of January 2022). . . . 43
B.7 Total number of observations per receiving antenna. . . . 43
B.8 Evolution of the standard deviation of the uncertainties with respect to time. The reference time is set on the day when InSight lander arrived on the Martian surface. The black dashed line separates the RISE and LaRa radio science experiments. . . . 44
B.9 Final formal errors of the estimated parameters obtained from different sets of configurations. 46
B.10 Real measurements observed from Badary station at 01:30:06 UTC on the 22nd of February 2020. . . . 47

B.11 Real measurements observed from Badary station at 01:35:36 UTC on the 22nd of February 2020. . . . 47
B.12 Real measurements observed from Badary station at 01:50:06 UTC on the 22nd of February 2020. . . . 48
B.13 Real measurements observed from Badary station at 01:54:16 UTC on the 22nd of February 2020. . . . 48
B.14 Real measurements observed from Ceduna station at 01:50:05 UTC on the 22nd of February 2020. . . . 48
B.15 Real measurements observed from Ceduna station at 01:53:25 UTC on the 22nd of February 2020. . . . 48
B.16 Real measurements observed from Effelsberg station at 08:40:05 UTC on the 29th of May 2020. . . . 49
B.17 Real measurements observed from Effelsberg station at 09:00:05 UTC on the 29th of May 2020. . . . 49
B.18 Real measurements observed from Effelsberg station at 03:13:45 UTC on the 21st of October 2020. . . . 49
B.19 Real measurements observed from Effelsberg station at 03:25:05 UTC on the 21st of October 2020. . . . 49
B.20 Real measurements observed from Effelsberg station at 03:35:05 UTC on the 21st of October 2020. . . . 50
B.21 Real measurements observed from Hartrao station at 01:50:05 UTC on the 22nd of February 2020. . . . 50
B.22 Real measurements observed from Hartrao station at 01:54:15 UTC on the 22nd of February 2020. . . . 50
B.23 Real measurements observed from Hartrao station at 08:40:05 UTC on the 29th of May 2020. . . . 50
B.24 Real measurements observed from Irbene station at 08:40:05 UTC on the 29th of May 2020. . . . 51
B.25 Real measurements observed from Medicina station at 03:14:15 UTC on the 30th of May 2020. . . . 51
B.26 Real measurements observed from Medicina station at 03:25:05 UTC on the 30th of May 2020. . . . 51
B.27 Real measurements observed from Medicina station at 03:35:15 UTC on the 30th of May 2020. . . . 52
B.28 Real measurements observed from Medicina station at 03:56:05 UTC on the 22nd of October 2020. . . . 52
B.29 Real measurements observed from Medicina station at 04:03:55 UTC on the 22nd of October 2020. . . . 52
B.30 Real measurements observed from Onsala station at 03:14:15 UTC on the 21st of October 2020. . . . 52
B.31 Real measurements observed from Onsala station at 03:25:05 UTC on the 21st of October 2020. . . . 53
B.32 Real measurements observed from Onsala station at 03:35:05 UTC on the 21st of October 2020. . . . 53
B.33 Real measurements observed from Onsala station at 03:56:05 UTC on the 22nd of October 2020. . . . 53
B.34 Real measurements observed from Onsala station at 04:04:35 UTC on the 22nd of October 2020. . . . 53
B.35 Real measurements observed from Tian Ma station at 01:30:05 UTC on the 22nd of October 2020. . . . 54

B.36 Real measurements observed from Tian Ma station at 01:35:05 UTC on the 22nd of October 2020. . . . 54
B.37 Real measurements observed from Tian Ma station at 01:50:05 UTC on the 22nd of October 2020. . . . 54
B.38 Real measurements observed from Tian Ma station at 01:54:15 UTC on the 22nd of October 2020. . . . 54
B.39 Real measurements observed from Dwingeloo station at 03:14:15 UTC on the 21st of October 2020. . . . 55
B.40 Real measurements observed from Dwingeloo station at 03:25:06 UTC on the 21st of October 2020. . . . 55
B.41 Real measurements observed from Dwingeloo station at 03:35:16 UTC on the 21st of October 2020. . . . 55
B.42 Real measurements observed from Dwingeloo station at 03:56:06 UTC on the 22nd of October 2020. . . . 55
B.43 Real measurements observed from Dwingeloo station at 04:04:46 UTC on the 22nd of October 2020. . . . 56
B.44 Real measurements observed from Wettzell station at 03:14:15 UTC on the 30th of May 2020. . . . 56
B.45 Real measurements observed from Wettzell station at 03:25:05 UTC on the 30th of May 2020. . . . 56
B.46 Real measurements observed from Wettzell station at 03:35:15 UTC on the 30th of May 2020. . . . 56
B.47 Real measurements observed from Wettzell station at 03:56:05 UTC on the 22nd of October 2020. . . . 57
B.48 Real measurements observed from Wettzell station at 04:04:25 UTC on the 22nd of October 2020. . . . 57
B.49 Real measurements observed from Yebes station at 09:00:05 UTC on the 29th of May 2020. . . . 57
B.50 Real measurements observed from Yebes station at 03:56:05 UTC on the 22nd of October 2020. . . . 57
B.51 Real measurements observed from Yebes station at 04:04:35 UTC on the 22nd of October 2020. . . . 58

List of Tables

1 List of Latin Symbols. ix
2 List of Greek Symbols. ix
3 List of Sub- and Superscripts. x
4 List of Special Characters. x
5 List of Abbreviations. xi

A.1 Comparison of formal errors. 38
A.2 Comparison of formal errors. 39

B.1 The standard deviation of the uncertainties of the estimated parameters. 45

List of Symbols and Abbreviations

Symbols

Table 1: List of Latin Symbols.

Symbol	Definition	Unit
C	Polar moment of inertia	[m^4]
d	Distance	[m]
e	Dynamical flattening	[-]
f	Frequency	[Hz]
F	Core factor	[-]
H	Design matrix	[-]
I	Axial tilt	[rad]
m	Steepness	[-]
p	Prograde term	[-]
P	Covariance matrix	[-]
r	Retrograde term	[-]
$\mathbf{R}_\alpha$	Rotation matrix	[-]
R	Sidereal angle matrix	[-]
PN	Precession-nutation matrix	[-]
t	Time	[s]
w	Weighting factor	[-]
W	Weighting matrix	[-]
X	Amplitude component of the polar motion along the x-axis	[-]
Y	Amplitude component of the polar motion along the y-axis	[-]

Table 2: List of Greek Symbols.

Symbol	Definition	Unit
β	Compliance related to the contribution of the deformation at the core-mantle boundary	[-]
γ	Compliance related to the deformation of Mars	[-]
θ	Longitude	[rad]
λ	Latitude	[rad]
μ	Mean	[-]
$\mathbf{\Pi}$	Polar motion matrix	[-]
ρ	Correlation coefficient	[-]
1-σ	One standard deviation	[-]
σ	Observation weights	[-]
σ_{FCN}	Free core nutation rate	[rad/s]
ς	Noise as modified Allan deviation	[-]
τ	Integration time	[s]
ϕ	Sidereal angle	[rad]
ψ	Longitude	[rad]
χ	Formal error	[-]

Table 3: List of Sub- and Superscripts.

Sub- and Superscript	Definition
$\square^{c}$	Cosine term
$\square_{C}$	Chandler Wobble
$\square_{f}$	Fluid core
$\square_{k}$	Maximum number of time observations
$\square_{m}$	Order term
$\square_{n}$	Number of ground stations visible
$\square_{p}$	Polar motion
$\square^{s}$	Sine term
$\square_{\text{sun}}$	Solar plasma
$\square_{x}$	Around the x-axis
$\square_{y}$	Around the y-axis
$\square_{z}$	Around the z-axis

Table 4: List of Special Characters.

Special Characters	Definition
$\square'$	Non-rigid body
$\overline{\square}$	Normalized value
$\Delta\square$ and $\delta\square$	Change in the value
$\dot{\square}$	First derivative of the value
$\square^{\Re}$	Real term
$\square^{\Im}$	Imaginary term
$\overline{\blacksquare}_{0}$	A priori matrix
$\blacksquare^{T}$	Matrix transpose
$\lvert\blacksquare\rvert$	Magnitude of the vector
$\dot{\blacksquare}$	First derivative of the vector
$\vec{\blacksquare}$	3D vector

Abbreviations

Table 5: List of Abbreviations.

Abbreviation	Definition
DSN	Deep Space Network
DSS	Deep Space Station
ESA	European Space Agency
EVN	European VLBI Network
FCN	Free Core Nutation
GNSS	Global Navigation Satellite System
JIVE	Joint Institute for VLBI in Europe
LaRa	Lander Radioscience
LOS	Line Of Sight
MOP	Mars rotation and Orientation Parameter
NASA	National Aeronautics and Space Administration
PRIDE	Planetary Radio Interferometry and Doppler Experiment
RF	Radio Frequency
RISE	Rotation and Interior Structure Experiment
RMSE	Root-Mean-Square Error
PLL	Phase Lock Loop
SEP	Sun-Earth-Probe
SNR	Signal-to-Noise Ratio
VLBI	Very-Long-Baseline Interferometry
TUDAT	TU Delft Astrodynamics Toolbox

1 Introduction

1.1. Background

Having a deep understanding of the interior and dynamics of an outer planet would provide crucial knowledge of its origin and evolution. Since probing the deep interior of a planet with in situ measurements is unworkable, a non-invasive retrieval technique must be used. One of the most effective approaches remains that of analyzing the Doppler of the radio retransmissions from a transponder, which can be launched on-board a spacecraft or on a lander vehicle. The kinematics of the transponder is under the influence of the planet's gravitational field. Therefore, Doppler measurements made with an Earth-based ground station interrogating the remote transponder with a radio signal allows the retrieval of precise geodetic observations of the planet, such as the rotational parameters and ephemerides. A well developed radio tracking technique, called Planetary Radio Interferometry and Doppler Experiment (PRIDE), has proven to maximize the science return of deep-space planetary missions. The PRIDE experiment is an initiative of the Joint Institute for VLBI in Europe (JIVE) and is based on ultra-accurate phased-referencing VLBI and radial Doppler observations (Duev et al. 2012). Since the beginning of this century, several international missions have already exploited the PRIDE technique, such as Venus Express and Mars Express ESA's missions. Results obtained during these missions show that the PRIDE technique can improve the quality of the geodetic data and thus be of benefit for a wide range of scientific applications, as reported in Bocanegra-Bahamon et al. (2019) and Pallichadath et al. (2020). It is worth mentioning that the interest in the PRIDE technique has increased substantially over the years due to the publication of Duev et al. (2012), where very effective pre- and post-processing algorithms were successfully validated with real Doppler observation data.

Up to now, the scientific community has not yet established the status of the matter of the inner core of Mars, whether it is liquid or solid (Rivoldini et al. 2011). Only the state of the outer core is known, which is liquid like the outer core of the Earth and Venus. A reduction in the uncertainty of the parameters that define the rotational dynamics of Mars, would provide more knowledge regarding the Mars' inner core. In June 2023, the ExoMars lander was expected to touch down on the surface of Mars. ExoMars is a cooperative mission between the European Space Agency (ESA) and Roscosmos and, unfortunately, the recent invasion in Ukraine has led to the decision to postpone the launch until a replacement of the Russian lander vehicle is found. One of the main scientific goals of this mission is to understand the inner core structure and the processes that take place inside the Red planet. For the ExoMars lander, the Royal Observatory of Belgium (ROB) has developed the Lander Radioscience (LaRa) instrument for a space geodesy experiment, which is aimed at the precise retrieval of the Mars rotation and Orientation Parameters (MOPs) (Dehant et al. 2020). A sister instrument is the Rotation and Interior Structure Experiment (RISE), which is installed on-board the NASA's InSight lander. The American lander arrived on the surface of Mars in November 2018 and is set to power down by December 2022 (Folkner et al. 2018).

Recent studies, as for instance that in Peters et al. (2020), show that the science return of the PRIDE technique is enhanced by combining both RISE and LaRa Doppler observations. Additionally, the results shown in Filice (2019), which are based on numerical simulations of the InSight RISE experiment

made prior to its launch, indicate that the accuracy of the MOPs is improved when using an extended network of receive-only Earth based stations. Since this analysis was performed without any real Doppler observation data from the InSight mission and, therefore, a follow-on assessment using real InSight Doppler observations has become a priority. In this context, the focus of this thesis is to address this scientific gap by:

> Improving a PRIDE-based method that makes a more realistic assessment of the MOPs inaccuracies by exploiting jointly the Doppler observations from NASA's InSight and ESA's ExoMars landers.

The main objective of this work is to reduce the MOPs uncertainty using a covariance-based method combining the Doppler observations data from the two Martian landers. This research aims to improve the performance of the PRIDE technique in preparation for the ExoMars mission, which is scheduled to launch in the near future. Additionally, based on the findings made in Filice (2019), the proposed simulation analysis considers the configuration with multiple receive-only Earth-based stations. When several receive-only stations are taken into account in a simulation analysis, the full set of cross-correlation coefficients of the Doppler observables from all stations must be determined. A comprehensive analysis of the five observation passes of the InSight lander collected by a network of radio telescopes managed by JIVE was used to compute the cross-correlations.

1.2. Research Questions

Based on the scientific gap and main objective of this thesis introduced in Section 1.1, the main research question that this project should answer is the following:

> How much can the uncertainty of the estimated parameters from RISE and LaRa observables be reduced by using the PRIDE technique?

In order to answer it in a meaningful way, formulating a number of research subquestions would help to comprehend precisely the topics involved in the study and to avoid deviating from the main objective. Hence, its sub-questions are found below:

1. How is the correlation coefficient of the Doppler observables made at the Earth-based ground stations calculated?
2. How is the interplay between MOPs on the observables in a single-lander configuration and two-lander configuration?
3. What is the improvement of the accuracy of the MOPs by combining RISE and LaRa instrument measurements?
4. What is the improvement of the accuracy of the MOPs by implementing additional receive-only antennas?

1.3. Report Outline

This thesis report is organized as follows. First, the thesis work is presented in Chapter 2 as a journal-style scientific paper. Then, key conclusions and recommendations for potential future work are discussed in Chapter 3. This is followed by a number of appendices where additional information is presented in order to complement the information presented in the journal paper. The first appendix, Appendix A, reports the verification and validation tests that have been conducted along the thesis. Since not all of the results can be shown in a journal paper, Appendix B contains additional results. These results include the analysis of the real open-loop data from the ED045 experiments measured in 2020 year by different JIVE radio telescopes. Lastly, the implementations added to the astrodynamical toolkit of the department are given in Appendix C.

2

Journal Article

An improved estimation of the Mars rotation and orientation parameters from the combined Doppler observables of the InSight-RISE and ExoMars-LaRa landers

C. Fortuny Lombraña* and D. Dirkx†
Delft University of Technology, Kluyverweg 1, 2629 HS Delft, The Netherlands

ABSTRACT

Context. The radio science studies on the RISE and LaRa instruments onboard, respectively, the InSight and ExoMars landers, have facilitated the development of the Planetary Radio Interferometry and Doppler Experiment (PRIDE) technique. The analysis of the Doppler observables from Earth-based radio telescopes using the PRIDE technique allows an improved estimation the Mars rotation and Orientation Parameters (MOPs). This study intends to further performance improvement of the PRIDE technique in preparation of the ExoMars mission, which is set to launch in a near-future.

Aims. Based on numerical simulations, we aim to develop a processing technique that reduces the uncertainty of the MOPs, which in turn allows a more precise determination of the state and composition of the inner core of Mars. With this, we intend to fully understand the interplay and the signature of the different MOPs. We want to exploit all available PRIDE-based Doppler observations including real and simulated datasets, respectively, from the InSight-RISE and ExoMars-LaRa experiments.

Methods. We perform a covariance analysis to simulate the MOPs uncertainty using an ensemble of 13 Earth-based ground stations and two Martian landers. We complete an in-depth analysis of the Doppler observables from the ED045 RISE radio science experiment, assessing thoroughly the behaviour of the cross-correlations of all pairs of ground stations. Based on the high-accuracy Mars rotation model of the TUDAT astrodynamical toolkit, we develop a novel MOPs retrieval processing scheme that exhibits an improved performance.

Results. In a two-lander configuration, we estimated a reduction of more than 92 % overall on the MOPs uncertainty compared to a single-lander configuration. Further, in a configuration exploiting the available set of 10 supplementary receive-only Earth-based PRIDE stations, the accuracy of the MOPs is additionally improved. More specifically, on average, a 12 % increase for the core factor F, a 10 % for the free core nutation rate σ_{FCN}, about 25 % for the polar motion parameters at the Chandler frequency, a 5 % for the spin variations, and a 15 % for the other polar motion amplitudes.

Conclusions. Our main findings are consistent with the hypothesis and previous analyses that the two-lander geometry configuration allows for a more precise retrieval of the MOPs, with an improvement of the accuracy by almost a factor of 2 with respect to a single-lander case. We have observed that a combined use of RISE and LaRa Doppler observations leads to a more efficient and accurate estimation of the full set of the MOPs and, particularly, the polar motion parameters. On top of this, we have noted that the exploitation of the available set of 10 receive-only Earth-based stations boosts additionally the accuracy in the estimation of the MOPs, indicating that this is the preferred data processing configuration.

Keywords— Radio Astronomy, Radio Tracking, PRIDE Technique, Mars Rotation and Orientation, Planetary Geodesy, Covariance Analysis.

1. Introduction

EXPLORING the deep layers of the Red planet can reveal valuable insights into its origin and dynamic evolution (Cottaar et al. 2021). Having a thorough understanding of its internal structure provides crucial information not only on the mass redistribution but also on the Mars rotation and Orientation Parameters (MOPs). Interplanetary radio tracking is one of the techniques that has been used to retrieve the MOPs (Dehant et al. 2020). Although there have been many interplanetary missions to Mars, only a few of them involved a lander which allowed to use radio tracking techniques to retrieve the MOPs from the Doppler observations. However, the precise determination of the MOPs associated with precession and nutation of Mars is still partly open and new a more precise retrieval

*MSc Spaceflight Student (Corresponding Author)
†Assistant Professor, Department of Astrodynamics and Space Missions

techniques are needed (Kahan et al. 2021).

NASA's Insight and ESA's ExoMars are two major interplanetary missions aimed to study the deep interior of the Red planet (Peters et al. 2020). These missions integrate a lander vehicle with a radio transponder that can be sounded from Earth-based ground stations. The radio transponder on the InSight lander vehicle, which will end its operations in December 2022, is the Rotation and Interior Structure Experiment (RISE) instrument (Buccino et al. 2022). The sister onboard system that is conceived for the ExoMars mission is the Lander Radioscience (LaRa) instrument (Dehant et al. 2020). Both instruments are designed to provide precise measurements of the Doppler shifts observed from Earth-based stations, which are used to retrieve accurate estimates of the MOPs. After one Martian year of RISE observations, the effects of liquid core on the nutation of Mars have been noticed for the first time (Le Maistre, Rivoldini, et al. 2021).

Interplanetary radio tracking is primarily used for navigation (i.e., determining and propagating the space vehicle position and velocity) and telemetry (i.e., acquiring and transmitting data recorded by the instruments), but it can also be employed to carry out scientific experiments, such as radio science experiments through Doppler and Very Long Baseline Interferometry (VLBI) observables (Bocanegra-Bahamon 2019). In this work, Doppler observables are the primary source of data, and thus there is no need for VLBI observables. For typical radio tracking, the same Earth-based station transmits and receives the radio signals.

Recently, a cutting-edge radio tracking implementation, known as Planetary Radio Interferometry and Doppler Experiment (PRIDE), has been developed at the Joint Institute for VLBI ERIC (JIVE), combines extremely precise phased-referencing VLBI observations with radial Doppler measurements. The receiving and transmitting stations are distinct, which distinguishes this new technique from traditional radio tracking. This implies that the Doppler observables can thus be observed by a network of receive-only radio telescopes (Duev et al. 2012). PRIDE technique has been exploited successfully in a large number of interplanetary missions. The Mars Express, Venus Express, BepiColombo, and other missions have carried out PRIDE experiments that have supported a wide range of scientific applications (Bocanegra-Bahamon, Calves, Gurvits, Cimo, et al. (2019) and Pallichadath et al. (2020)). It is worth noting that the interest in the PRIDE technique increased substantially with the publication of Duev et al. 2012, which entailed the introduction of innovative pre- and post-processing algorithms.

A preliminary post-processing scheme of the Doppler observables that reduces the uncertainty in the determination using only simulated numerical simulations of the RISE radio science experiments was developed by Filice (2019). An overall improvement in the MOPs accuracy of about 18 % was reported in Filice (2019) using a network of receive-only stations. Recent investigations, the one presented in Peters et al. (2020), have shown that the combination of RISE and LaRa Doppler observations enhances the science return. Up to now, most of the studies have employed a one-lander configuration for the determination of the MOPs, the use of the PRIDE technique on a two-lander configuration has not been investigated yet. Hence, the objective of this work is to improve the processing scheme of the Doppler observables that reduces the uncertainty in the determination of the MOPs by using a two-lander configuration and the PRIDE technique. For this purpose, real Doppler observation data from NASA's InSight and numerically generated data from ESA's ExoMars missions have been used. The hypothesis is that by utilizing Doppler observations from two landers via a network of radio telescopes, the accuracy of the estimated MOPs can be improved.

In order to exploit the observation data efficiently, a covariance analysis is the most convenient statistical tool to tackle this precise orbit determination problem. Since the signal echoed back by the RISE and LaRa instruments can be received by several receive-only radio telescopes on Earth, the receiving ground stations share the uplink path and a portion of the downlink. This indicates that some random noises are shared by all ground stations, and the covariance analysis should include the cross-correlations of the Doppler observables between all pairs of ground stations. Here, a method to compute the correlation coefficients of the Doppler observables made at the Earth-based ground stations is developed and presented. More precisely, the observation data from five different passes of the InSight lander, which were recorded by several radio telescopes in 2020, are analyzed to estimate the full set of cross-correlation coefficients of Doppler observations from all stations. The open-source TU Delft Astrodynamics Toolbox (Tudat) has been extensively used to quantify the Doppler uncertainties. This toolkit is created by students, researchers, and professors at Delft University of Technology's Faculty of Aerospace Engineering, and publicly accessible on GitHub[1].

This paper is organized as follows. Section 2 introduces the rotational model of Mars and the calculation of the MOPs. The tracking strategy together with the differences between RISE and LaRa radio science experiments data is presented in Section 3. In Section 4, the different steps of the proposed methodology to reduce the uncertainties in the estimation of the MOPs are explained. The results of the numerical simulations are presented and discussed in Section 5. Last but not least, conclusions and recommendations for possible follow-ons are highlighted in Section 6.

2. Mars Rotation Model

This section describes the Mars rotation model, and more specifically the *Pathfinder model* (Konopliv, Yoder, et al. 2006), as well as the MOPs used to define the rotational state. The rotation of Mars has been studied and modeled more precisely than in any other planet in our solar system, with the exception of Earth. Compared to earlier Mars rotation models, such as *Mariner 9 model* and *Viking model*, the *Pathfinder model* has been the first to provide an estimate of the Martian precession

[1] https://github.com/tudat-team/tudat and https://github.com/tudat-team/tudatpy.

rate (Folkner et al. 2016). In order to model the Doppler shifts between the Earth-based ground stations and the Mars-based landers, the Doppler observables have been linearized in relation to the rotating parameters in the rotation matrix, such as polar motion, sidereal angle, and precession and nutation (Yseboodt, Barriot, and Dehant 2003).

2.1. Reference Frames

The variations in the rotation of Mars can be divided into three categories (Dehant et al. 2020): (1) rotational variations about the spin axis, (2) changes in the spin axis with respect to the inertial reference frame reference to inertial space, and (3) changes in spin axis with respect to the body-fixed axes. Each variation can be represented as a rotation matrix or a combination of them.

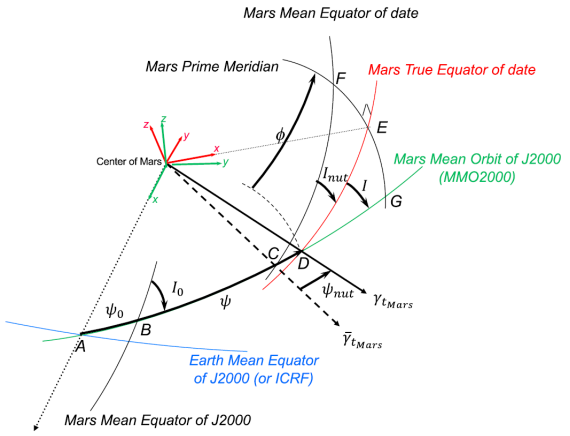

Figure 1. Mars orientation angles and reference frames for converting the coordinates between the inertial frame (Mars mean orbit in green) and Mars body-fixed rotating frame (in red). Taken from Le Maistre, Rosenblatt, Dehant, et al. (2018).

In order to find the parameters that orient Mars, it is essential to determine the rotation matrix between the body-fixed reference frame ($\vec{r}_{\text{fixed}}$) and the inertial reference frame ($\vec{r}_{\text{inertial}}$) (Le Maistre 2013). Figure 1 shows the different intermediate reference frames that are used in this transformation, which is defined as,

$$\vec{r}_{\text{fixed}} = \mathbf{\Pi}\,\mathbf{R}\,\mathbf{PN}\,\vec{r}_{\text{inertial}} \tag{1}$$

where $\mathbf{\Pi}$ is the polar motion matrix, $\mathbf{R}$ is the sidereal angle matrix, and $\mathbf{PN}$ is the precession-nutation matrix.

The polar motion matrix carries the rotation pole to the z-axis of the Mars body-fixed rotating frame (see Figure 1). Two rotating angles, also known as two pole coordinates X_p and Y_p, are required to switch from a frame tied to the rotation axis to a frame tied to the Mars (Le Maistre 2013). Since the amplitude of the polar motion is small when compared to the radius of Mars, the two rotation angles are small, and the transformation matrix can therefore be represented in terms of infinitesimal rotations around the x- and y-axes (see Appendix A.1 for the definition of the rotation matrices). The polar motion matrix $\mathbf{\Pi}$ is defined as,

$$\mathbf{\Pi} = \mathbf{R}_y\left(-X_p\right)\mathbf{R}_x\left(-Y_p\right). \tag{2}$$

The sidereal angle matrix $\mathbf{R}$ is the rotational matrix associated with the sidereal angle ϕ,

$$\mathbf{R} = \mathbf{R}_z\left(\phi\right). \tag{3}$$

This angle is measured from the Mars prime meridian to its vernal equinox along the celestial equator. It defines the rotation around the z-axis from the Mars body-fixed reference frame aligned with the figure axis of the planet (see Figure 1).

Finally, the precession-nutation matrix is built upon the longitude ψ of the node of the Mars body-fixed rotating frame and the axial tilt I between the Mars body-fixed rotating frame and the Mars mean orbital plane. In other words, the $\mathbf{PN}$ matrix rotates a vector from the MMO2000 xy-plane into the Mars true equator plane (see Figure 1). This last transformation is represented as the combination of the rotations defined by these two angles as,

$$\mathbf{PN} = \mathbf{R}_x\left(-I\right)\mathbf{R}_z\left(\psi\right). \tag{4}$$

2.2. Modeling the MOPs

The definition of the MOPs is the final step to determine the Mars rotational state. These are related to the rotation angles introduced above and are briefly discussed in this subsection.

2.2.1. Polar Motion

The polar motion is mainly caused by the seasonal mass exchanges between the polar caps and the atmosphere, as well as the Chandler wobble periodic component (Van Hoolst et al. 2000b). The two polar motion components, X_p and Y_p, can be expressed as a series of harmonic motions:

$$X_p = \sum {X_p}_m^c \cos\left(2\pi f_m t\right) + {X_p}_m^s \cos\left(2\pi f_m t\right), \tag{5}$$

$$Y_p = \sum {Y_p}_m^c \cos\left(2\pi f_m t\right) + {Y_p}_m^s \cos\left(2\pi f_m t\right) \tag{6}$$

where ${X_p}_m^c$, ${X_p}_m^s$, ${Y_p}_m^c$ and ${Y_p}_m^s$ amplitudes are denoted polar motion parameters. Each of them is associated with a harmonic frequency f_m. The polar motion parameters are part of the MOPs and provide information on the Martian mantle, atmosphere and ice caps (Yseboodt, Barriot, Dehant, and Rosenblatt 2004).

2.2.2. Sidereal Angle

The sidereal angle of a non-precession and non-nutation planet is defined as,

$$\phi\left(t\right) = \phi_0 + \dot{\phi}\left(t - t_0\right) + \Delta\phi \tag{7}$$

where ϕ_0 is the spin angle at the reference epoch t_0, $\dot{\phi}$ is the angular velocity related to the uniform rotation and $\Delta\phi$

is the periodic variation of ϕ. The main reason behind this periodic variation is the seasonal mass exchange of carbon dioxide between the atmosphere and the ice caps (Yseboodt, Barriot, Dehant, and Rosenblatt 2004). The periodic variation is expressed as follows,

$$\Delta\phi = \sum \phi_m^c \cos(2\pi f_m t) + \phi_m^s \sin(2\pi f_m t) \quad (8)$$

where ϕ_m^c and ϕ_m^s are referred to as spin variation parameters, and are associated with the respective harmonic frequency f_m. The spin variation parameters are included in the MOPs.

2.2.3. Precession and Nutation

The precession is a long-term motion of the rotation axis around an axis perpendicular to the ecliptic. The nutation is superimposed on this motion and consists of small variations in both the rate of precession and obliquity of the planet (Le Maistre, Rosenblatt, Rivoldini, et al. 2012). It is important to point out that nutations and precession are primarily driven by the attraction of the Sun on Mars. As **PN** matrix is a function of obliquity and longitude, the changes in obliquity and longitude are split into secular and periodic variations:

$$I(t) = I_0 + \dot{I}(t - t_0) + \Delta I, \quad (9)$$

$$\psi(t) = \psi_0 + \dot{\psi}(t - t_0) + \Delta\psi \quad (10)$$

where I_0 and ψ_0 are the obliquity and longitude at the reference epoch t_0, $\dot{I}$ and $\dot{\psi}$ are the secular changes of obliquity and longitude, ΔI and $\Delta\psi$ are the periodic variations in obliquity and longitude. Similarly to the sidereal angle and polar motion, the periodic variations can be expressed as,

$$\Delta I = \sum I_m^c(F, \sigma_{\mathrm{FCN}}) \cos(2\pi f_m t) + I_m^s(F, \sigma_{\mathrm{FCN}}) \sin(2\pi f_m t), \quad (11)$$

$$\Delta\psi = \sum \psi_m^c(F, \sigma_{\mathrm{FCN}}) \cos(2\pi f_m t) + \psi_m^s(F, \sigma_{\mathrm{FCN}}) \sin(2\pi f_m t) \quad (12)$$

where I_m^c,I_m^s,ψ_m^c,ψ_m^s amplitudes are indicated as nutation parameters and are associated with the harmonic frequencies f_m. Furthermore, the nutation terms can be divided into prograde and retrograde terms. These two motions can, at the same time, be written as a function of the core factor F and the free core nutation rate σ_{FCN} (see Appendix A.2 for its full derivation). Hence, the F and σ_{FCN} are transfer functions parameters for precession and nutation. Both two parameters are classified among the MOPs.

The latest and most accurate MOPs that have been published are from the Mars Reconnaissance Orbiter model; this is an update to the well-known *Pathfinder model* that takes into account all previous missions to Mars Reconnaissance Orbiter. Their values and errors can be found in Kuchynka et al. (2014), Konopliv, Park, and Folkner (2016), and Konopliv, Park, Rivoldini, et al. (2020). With InSight mission, it is anticipated that the actual rotational model will be improved as it will be possible to detect the nutations of Mars caused by non-rigid effects (Folkner et al. 2016).

3. PRIDE Technique

Deep-space radio tracking allows precise determination of the state vector of a spacecraft. PRIDE is a spacecraft tracking technique that employs transponders on spacecraft and a network of radio telescopes to provide VLBI and Doppler measurements. This is accomplished by precisely tracking the spacecraft carrier signal with radio telescopes on Earth. As a result, PRIDE is an additional function to the conventional radio tracking performed with DSN facilities used mainly for conducting scientific research (Bocanegra-Bahamon 2019). The traditional deep-space radio tracking also serves to send commands to the spacecraft and receive telemetry. It is important to note that the receive-only stations, also known as PRIDE stations, generate open-loop Doppler data, while the regular deep-space tracking stations generate closed-loop Doppler data.

In this section, a more in-depth description of the tracking strategies is given together with an introduction to the data and the noise sources that have been identified. Further, the main similarities and differences between the RISE and LaRa radio science experiments are discussed in general terms.

3.1. Tracking Strategies

Real time observations retransmitted by RISE and collected at different DSN ground stations can be retrieved from NASA's Planetary Data System repository[2]. Unfortunately, since the LaRa is not yet operational, no real data is available but only the times for the planned observation passes are known. Hence, two different tracking and setup strategies are applied in the simulations of the InSight and ExoMars missions. For InSight, a two-way configuration with the traditional radio tracking is employed, meaning that both uplink and downlink signals involve a single Earth-based antenna and the transponder on Mars. This implies that the addition five observation passes from 10 JIVE's radio telescopes are not taken into account in the simulations as they would not bring any major improvement. However, a more complex approach denoted PRIDE multi-station tracking strategy is used in the simulations of ExoMars mission. The use of several PRIDE stations can be advantageous, as there is a diversity of Doppler noise levels between receiving stations. With the addition of more receiving ground stations, a larger data set is analyzed thus potentially improving the accuracy of the estimated parameters. In this other strategy, the signal reflected by the transponder can be received by radio telescopes and the transmitter, as shown in Figure 2 (Dirkx 2015). The existence of multiple receiving stations rises the need of a noise level analysis between the Doppler observables, as these will be cross-correlated. By comparing the noise levels which are common to different ground stations, the full set of cross-correlation coefficients can be determined. More details about the noise levels are presented in Section 3.3.

For both missions, the only transmitters that generate the carrier are the antennas from the Deep Space Network (DSN). The three DSN ground facilities are located in Canberra (DSS-34,-

[2] https://pds-geosciences.wustl.edu/missions/insight/rise.htm

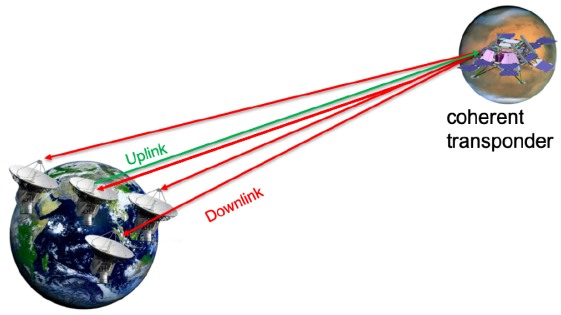

Figure 2. Sketch of a PRIDE multi-station tracking strategy. Taken from Filice (2019).

35,-36,-43), Madrid (DSS-54,-55,-56,-63,-65), and Goldstone (DSS-14,-24,-25,-26), which can transmit and receive signals at the same time. The carrier frequency for downlink and uplink are slightly distinctive to avoid interference between them. For instance, the uplink and downlink frequencies for LaRa are 7.162 GHz and 8.415 GHz (X-band), respectively (Peters et al. 2020). There was no reason to include simulated Doppler observations for RISE radio science experiments from receive-only stations if existing data from the InSight mission could be collected. Since ExoMars has not been launched, the PRIDE multi-station tracking strategy using the 10 radio telescopes administered by JIVE can be exploited. The five RISE observation passes from 10 JIVE's radio telescopes through the 2020 year are therefore useful for the computation of the correlation coefficient of the Doppler observations made at the Earth-based ground stations for the multi-station tracking strategy applied to LaRa radio science experiments.

The locations of the DSN ground facilities and the radio telescopes implemented in the simulations are displayed in Figure 3.

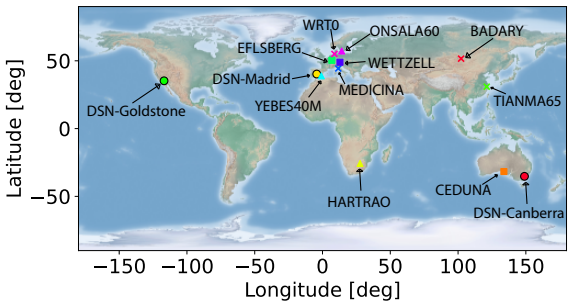

Figure 3. Locations of the ground stations illustrated in a world map. The transmitter ground stations are indicated with a circle marker together with a black outline.

3.2. Closed-Loop and Open-Loop Doppler Retrieval Schemes

The Doppler in the received signal originates from the relative motion between the lander and the Earth-based station. The Doppler can be estimated at the ground stations using either a closed-loop or an open-loop retrieval schemes at the receiver. A closed-loop retrieval scheme implements a real-time detection mechanism, including a phase-lock loop (PLL), that locks the phase of the received RF signal with a local oscillator at the ground station. Instead, an open-loop scheme implements the phase locking of the received RF signal at a later stage, making use of a digital PLL mimicking the real-time detection in the closed-loop scheme. For both receiver architectures, the Doppler observables are obtained by differentiating the phase output of the PLL (Bocanegra-Bahamon, Calves, Gurvits, Duev, et al. 2018).

In radio science experiments, the open-loop mechanism is preferred as the received signal exhibits abrupt changes in frequency and amplitude. This means that the PRIDE stations can precisely predict the carrier frequency without using a real-time detection mechanism (Bocanegra-Bahamon, Calves, Gurvits, Cimo, et al. 2019). On the contrary, regular deep-space tracking stations make use of the closed-loop Doppler retrieval scheme as they are used for navigation and telemetry applications.

3.3. Data Processing

All observations attain a certain level of uncertainty due to the inaccuracies associated to the instruments and propagation models as well as the presence of systematic noise. Moreover, software issues, human errors or hazardous weather conditions can also represent significant uncertainty sources and thus cannot be disregarded. The error distribution cannot be explained by a single statistical model (Filice 2019). As introduced in the tracking strategies, the full set of cross-correlations of the Doppler observables between ground stations is needed when PRIDE stations are used in the simulations. For a meaningful computation of the correlation coefficients, it is essential to identify the contribution of the main noises affected in an X-band radio signal. Therefore, a noise budget for the X-band and time integration τ at 60 s has been build and presented in Table 1 using Armstrong (2006) and Iess et al. (2012) from the last Cassini mission, as well as expectations for the missions under consideration. The contribution of the noise sources are expressed as modified Allan deviation at 60 s integration.

Since the DSN two-way Doppler data from InSight mission are sampled with a period of 1 min, the time integration τ for evaluating the noise is set to the same value. The noise sources that have been taken from Armstrong (2006) have a different time integration, τ is equal to 1000 s. Assuming that the noise sources are totally random, each noise source from Armstrong (2006) are converted from τ=1000 s to τ=60 s.

When the PRIDE multi-station tracking strategy is applied in the ExoMars mission, the signal transmitted from a DSN antenna can be received by several radio telescopes, including the

Table 1. Noise budget expressed as modified Allan deviation evaluated at τ=60 s.

Noise Source	Contribution [-]	Source
Frequency Standard	$3.27{\cdot}10^{-15}$	Armstrong (2006)
Antenna Mechanical	$1.6{\cdot}10^{-14}$	Iess et al. (2012)
Ground Electronics	$8.17{\cdot}10^{-16}$	Armstrong (2006)
Plasma Phase Scintillation	$[5.33{\cdot}10^{-11}, 1.27{\cdot}10^{-14}]$	Iess et al. (2012)
Stochastic Spacecraft Motion	$8.17{\cdot}10^{-16}$	Armstrong (2006)
Receiver Thermal Noise	$4.08{\cdot}10^{-16}$	Armstrong (2006)
Spacecraft Transponder Noise	$1.8{\cdot}10^{-14}$	Iess et al. (2012)
Tropospheric Scintillation	$6.5{\cdot}10^{-14}$	Iess et al. (2012)

transmitting antenna. Since the receiving ground stations share the uplink path and part of the downlink, the recorded signals at different ground stations are moderately correlated. The cross-correlations of the Doppler observables can be determined by analyzing the random noises that are common to all ground stations (see Section 4.5). The common noise for a two-way link is the combination of the frequency standard, plasma phase scintillation, stochastic spacecraft motion, spacecraft transponder noise, and half of the tropospheric scintillation. In Table 1, the solar plasma is the only noise represented by a range as it is modeled as a function of the Sun-Earth-Probe (SEP) angle. The solar plasma model has been derived by Iess et al. (2012), and the equations valid for X-band and evaluated at τ=60 s are the following:

$$\varsigma_{\text{sun}}\,(0^\circ \le \text{SEP} \le 90^\circ) = 1.76 \cdot 10^{-14} \sin(\text{SEP})^{-1.98} + 6.25 \cdot 10^{-14} \sin(\text{SEP})^{0.06}, \quad (13)$$

$$\varsigma_{\text{sun}}\,(90^\circ < \text{SEP} \le 170^\circ) = \left(1.76 \cdot 10^{-14} + 6.25 \cdot 10^{-14}\right) \sin(\text{SEP})^{1.05}, \quad (14)$$

$$\varsigma_{\text{sun}}\,(170^\circ < \text{SEP} \le 180^\circ) = 1.27 \cdot 10^{-14} \quad (15)$$

where ς_{sun} is the plasma phase scintillation expressed as modified Allan deviation.

3.4. LaRa and RISE Radio Science Experiments

The RISE and LaRa instruments are designed to investigate the internal structure of Mars through estimation of the precession and nutation of the spin axis or, more specifically, the determination of the set of MOPs detailed in Section 2.2. Therefore, the X-band radio link between the landers and the Earth-based ground stations is used in the two experiments to retrieve coherent two-way Doppler measurements (Dehant et al. 2020).

However, there are some key differences between both radio science experiments. The InSight landing site and the expected location of the ExoMars touchdown are located in completely opposite parts of the Red planet. These are *Elyseum Planitia* and *Oxia Planum*, respectively (Peters et al. 2020). The difference in the location of both transmitters is one of the key reasons why the combination of the data from both missions can be greatly beneficial. The locations of both landers are displayed in Figure 4.

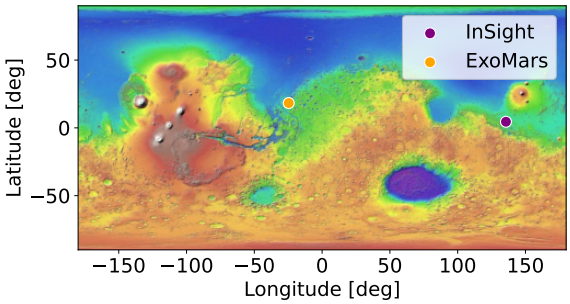

Figure 4. InSight and ExoMars landing zone targets.

The antenna configurations of the two experiments also present some differences worth highlighting. LaRa features one receiving and two transmitting monopole antennas that achieve the highest gain between 30° and 55° of line-of-sight elevation in all azimuth angles. In the RISE radio science experiment, two horn antennas that transmit and receive the signal continuously. One of these is pointing East, while the other one is heading West. The greatest gain of the RISE antennas occurs at 30° of line-of-sight elevation, with an aperture of roughly 25° off boresight (Peters et al. 2020). Since the antenna configurations and latitudes of the two landers are not the same, the observation pass durations are unequal. LaRa radio science experiment is planning to measure observations for 45 minutes twice a week, whereas RISE is typically reflecting the signal for an hour every day (Peters et al. 2020).

4. Orbit Determination Set-Up

This section describes the simulated estimation framework developed and addresses its limitations. Then, the parameters to be estimated are presented. A novel post-processing chain for the simulated PRIDE data and the scarce real radio tracking data is proposed. Figure 5 presents a global overview of the developed approach to reduce the uncertainty in the MOPs that will be discussed in this section.

4.1. Environment and Propagation Settings

Understanding which specific antennas are visible in each observation pass for the ExoMars mission requires propagating the orbit of Mars. This is due to the fact that the only data available is the planned observation windows for the LaRa radio science experiments. The Sun, Mercury, Venus, Earth, Moon, Mars, Jupiter, and Saturn are the primary celestial bodies that perturb the orbit of Mars, so these are created to represent the environment. Due to the great distance between the Earth and Mars, the global frame is chosen to be the mean ecliptic and equinox of J2000 (ECLIPJ2000) and the origin of such is placed at the solar system barycenter (SSB). The focus is set on the dynamics of Mars, being its orbit the only one propagated through the simulation using a central gravity model. The rotation ephemeris of Mars is modeled using the *Pathfinder model*

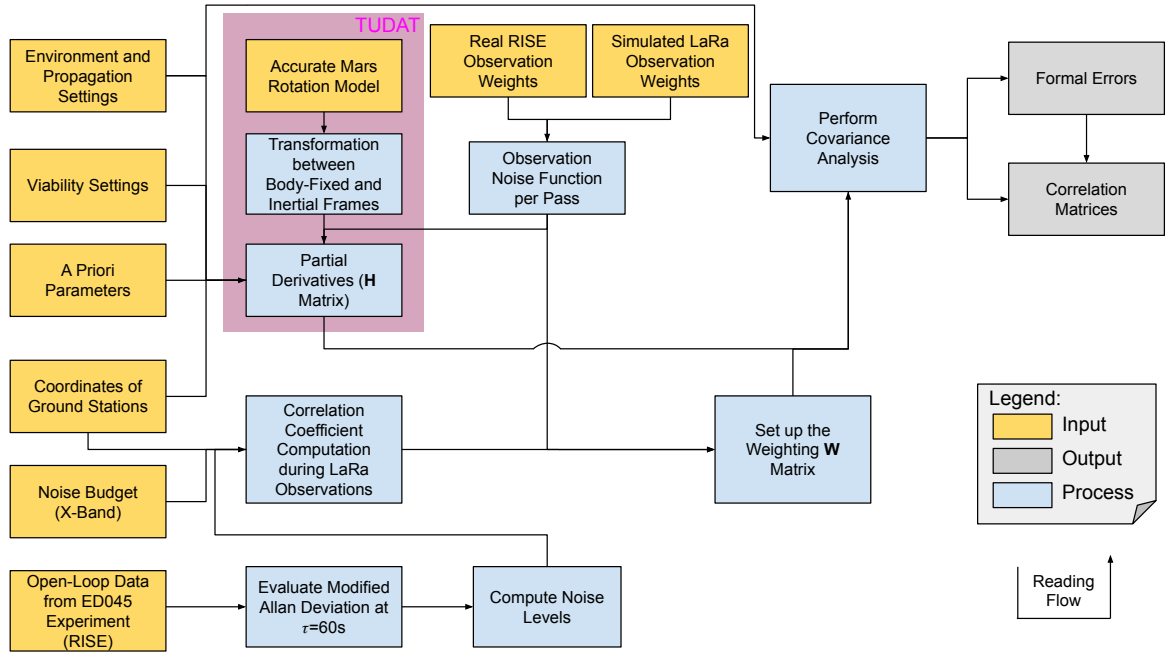

Figure 5. High-level flow diagram summarizing the methodology performed.

introduced in Section 2.2 and further described in-depth by Le Maistre (2013). The orbit and the rotation model of the other celestial models are instead modeled using the SPICE ephemeris[3].

For the propagation of the Mars orbit, its translational state as well as the integrator settings must be defined. The perturbations for the translational state from all the celestial bodies mentioned above were considered but for those from the Moon, which were considered negligible. Whereas the integrator type selected is a variable step-size Runge-Kutta integrator. A 7th order Runge-Kutta integrator with 8th order error is selected for the orbit propagation. The additional degree of freedom in the choice of the time step allows for a better control of the local error. The specific time step and tolerance settings of the integrator are shown in Table 2.

Table 2. Integrator set-up.

Initial Condition	Value
Initial Time Step	1 s
Min Step Size	1 s
Max Step Size	86400 s
Relative and Absolute Tolerance	$1{\cdot}10^{-12}$

Since the simulations results are to be compared with the data gathered by the real missions, data for at least 8 years must be thus generated to reproduce the missions time span. A trade-off between computational cost and accuracy must then be considered. For this reason, 1 Earth day is set as the maximum step size to keep a relatively high accuracy with the available computational resources. The final integration error is dominated by the maximum step size and the tolerance selected.

In addition to this, the propagation should take into account operational characteristics from each mission. As the antenna configurations are different (see Section 3.4), each instrument reaches its maximum gain at a different line-of-sight angle (Peters et al. 2020). Moreover, the signal is strongly perturbed by the solar conjunction for SEP angles lower than 10°. In order to improve the signal quality, only the Earth-based ground stations observations with an elevation angle larger than 10° were considered. All these observation limitations are denoted viability settings, and are listed in Table 3.

Table 3. Viability settings.

Requirement	Value
RISE Line-Of-Sight	[10°,30°]
LaRa Line-Of-Sight	[35°,45°]
Minimum Earth-based Station Elevation Angle	10°
Body Avoidance Angle for the Sun	10°

4.2. Estimated Parameters

The estimated parameters to be extracted from the observations can be divided into the initial state, two-lander positions and the MOPs. The initial state is the position and velocity of Mars

[3] https://naif.jpl.nasa.gov/naif/spiceconcept.html.

on its motion around the Sun, which are defined as x, y, z, $\dot{x}$, $\dot{y}$ and $\dot{z}$. Instead, the two-lander positions are characterized as $x_{\mathrm{RISE}}, y_{\mathrm{RISE}}, z_{\mathrm{RISE}}$ for InSight and $x_{\mathrm{LaRa}}, y_{\mathrm{LaRa}}, z_{\mathrm{LaRa}}$ for ExoMars. In this work, a total of 30 MOPs are considered. As introduced in Section 2.2, the MOPs can be split into three subgroups. The first subgroup contains the parameters that define the precession and nutation motion, which are the core factor F and the free core nutation rate σ_{FCN}. The spin variations, which represent the periodic variation of the sidereal angle, form the next subgroup, consisting of 4 cosine terms ϕ_m^c and sine terms ϕ_m^s until the 4th order. Lastly, the last 20 MOPs are included in the subgroup that defines the two polar motion components X_p and Y_p. Here, the polar motion amplitudes (cosine terms X_m^c, Y_m^c and sine terms X_m^s, Y_m^s) until the 4th order (including the ones associated with the Chandler frequency, m is about 3.34) are computed. In total, 42 parameters are estimated from the simulation data.

4.3. Covariance Analysis

A newly post-processing chain for combining observations from different missions and incorporating the PRIDE data has been developed. The proposed workflow is illustrated in Figure 5. The methodology followed to extract the uncertainties of the estimated parameters is based on a covariance analysis, which results in a significant reduction of formal errors. This approach is unique in that it does not assume that the observation weights and correlation coefficients of the Doppler observables between two Earth-based ground stations are constant. The determination of the observation weights and cross-correlations are described in Sections 4.4 and 4.5, respectively. Moreover, this innovative scheme is the first to be configured for a two-lander configuration.

The setup for the covariance analysis is documented below. As described in Schutz et al. (2004), the formal errors χ_i of the estimated parameters are defined as the square root of the diagonal elements of the covariance matrix $\mathbf{P}$:

$$\chi_i = \sqrt{\mathbf{P}_{ii}}, \tag{16}$$

$$\mathbf{P} = \left(\mathbf{H}^T\mathbf{W}\mathbf{H} + \mathbf{P}_0^{-1}\right)^{-1} \tag{17}$$

where $\mathbf{H}$ is the matrix of partial derivatives of the modeled observations, $\mathbf{W}$ is the weight matrix of the observations, and $\mathbf{P}_0$ is the a priori covariance matrix. The $\mathbf{H}$ matrix is obtained through a weighted least squares estimation performed with the astrodynamical toolkit Tudat (see Figure 5). It is important to mention that the covariance analysis is based on the weighted least squares with a priori knowledge, but the weight matrix that has been developed for the covariance matrix is not diagonal as it is commonly used in the least squares estimation. The Doppler observations, however, cannot be considered uncorrelated in the PRIDE multi-station tracking strategy. This is the reason why for the LaRa radio science experiment the traditional diagonal weight matrix $\mathbf{W}$ has been modified to introduce the existing cross-correlations (Filice 2019). The $\mathbf{W}$ matrix is a diagonal matrix, and its diagonal is made up of square matrices $\mathbf{\Sigma}$. The number of square matrices is determined by how the signal is discretized over time, where t is the observation time. Each square matrix is an inverse variance-covariance matrix that defines the degree of correlation between observations received by multiple Earth-based ground stations which share the same transmitter. The weight matrix $\mathbf{W}$ together with the diagonal element $\mathbf{\Sigma}$ are therefore expressed as,

$$\mathbf{W} = \begin{bmatrix} \mathbf{\Sigma}_{t_1}^{-1} & \cdots & 0 \\ \vdots & \ddots & \vdots \\ 0 & \cdots & \mathbf{\Sigma}_{t_k}^{-1} \end{bmatrix} \tag{18}$$

$$\mathbf{\Sigma}_{t_i} = \begin{bmatrix} \sigma_1^2 & \rho_{12}\sigma_1\sigma_2 & \cdots & \rho_{1n}\sigma_1\sigma_n \\ \rho_{12}\sigma_1\sigma_2 & \sigma_2^2 & \cdots & \rho_{2n}\sigma_2\sigma_n \\ \vdots & \vdots & \ddots & \vdots \\ \rho_{1n}\sigma_1\sigma_n & \rho_{2n}\sigma_2\sigma_n & \cdots & \sigma_n^2 \end{bmatrix} \tag{19}$$

where k is the maximum number of time observations, n is the number of ground stations visible at that specific time, the σ_i is the observation weight and $\rho_{i,j}$ represents the correlation coefficients of the noise levels between ground stations, for which more details are given in Section 4.5. The dimension of the square matrix $\mathbf{\Sigma}$ is given by the number of ground stations that have received the signal at that specific time of observation. During the RISE section of the simulation, as only DSN antennas are utilized, the square matrices $\mathbf{\Sigma}$ will be of 1x1 dimension and the regular diagonal structure is retrieved.

4.3.1. A Priori Parameters

In order to initialize the simulation, a priori values (represented as input in Figure 5) are given to the estimated parameters. The choice of these parameters allows for the reduction of the errors from the statistical method by providing the propagator with an informed guess of the a priori parameters. The a priori values are taken from literature, and other missions launched before the InSight. The list of the 42 a priori values associated with its source are found in Table 4.

Table 4. List of the a priori values.

Parameter	Uncertainty	Source
Position of Mars	1 km	Shan et al. (2018)
Velocity of Mars	0.2 mm/s	Shan et al. (2018)
F	0.07	Konopliv, Yoder, et al. (2006)
σ_{FCN}	1.5 deg/day	Konopliv, Yoder, et al. (2006)
Lander Coordinates	30 m	Kahn et al. (1992)
ϕ_1^c	23 mas	Le Maistre (2013)
ϕ_1^s	26 mas	Le Maistre (2013)
ϕ_2^c,ϕ_2^s	22 mas	Le Maistre (2013)
ϕ_3^c	18 mas	Le Maistre (2013)
ϕ_3^s	19 mas	Le Maistre (2013)
ϕ_4^c,ϕ_4^s	16 mas	Le Maistre (2013)
$X_{p_m}{}^c$,$X_{p_m}{}^s$,$Y_{p_m}{}^c$,$Y_{p_m}{}^s$	50 mas	Yseboodt, Barriot, Dehant, and Rosenblatt (2004)

The a priori covariance matrix $\mathbf{P}_0$ is built as a diagonal matrix, where the inverse of the a priori parameters mentioned in Table 4 are squared.

4.4. Observation Weights

Since a weighted covariance analysis is being used, the observation noise is applied to weight each Doppler observable. As illustrated in Figure 5, the observation weights from both missions are assumed to be different. The real observation noise per pass for RISE has been taken from Buccino et al. (2022) and the behavior varies significantly with the SEP angle due to the solar plasma shown in Table 1. As ExoMars has not been launched yet, the only noise source that is dependent on the SEP angle is the solar plasma. Hence, it has been assumed that the total observation noise per pass for the LaRa radio science experiment is the sum of the minimum observation noise of the RISE radio science experiment when the SEP angle is 180° plus the solar plasma increment, which can be determined by the fit model developed in Iess et al. (2012). For LaRa radio science experiment, only the largest noise source from Table 1 is considered, since the contribution of the other noise sources is much smaller when the SEP angle is smaller than 90°. The standard deviation of the observation noise per pass normalized with the downlink frequency is displayed in Figure 6 and these are the observation weights implemented in the weight matrix **W**. Since the observation noise per pass for RISE takes into consideration the entire ensemble of noise sources, the dip caused by the solar plasma model is not visible in the observation noise for RISE.

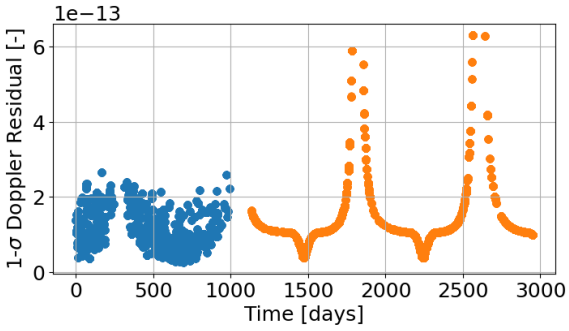

Figure 6. One standard deviation of Doppler noise as a function of time. The scatter points in blue are from RISE observations, whereas in orange are from LaRa observations.

Additionally, Figure 6 shows that RISE observations were recorded in the span of three years and started at the end of the year 2018. LaRa radio science experiments, on the other hand, are assumed to begin in 2022 and end in 2026. In fact, whether there is a larger gap between RISE and LaRa observations or observations are simultaneously, the covariance-based approach is still valid. This should not cause any significant effect on the improvement of the MOPs accuracy as all the variations in the rotation of Mars have a periodic behavior.

4.5. Cross-correlations of the Doppler Observables between Stations

A method to calculate the correlation coefficient $\rho_{i,j}$ of the Doppler observables between two ground stations has not yet been published. As introduced in Section 4.3, the cross-correlations are only required when the PRIDE multi-station tracking strategy is employed. In this configuration, the signal transmitted from a DSN antenna can be received by several Earth-based ground stations. Therefore, there are some shared noise sources in the data recorded at the different locations which can be identified after a proper analysis and comparison. The main differences in the received signal occur in the last part of the downlink, when the signal enters the atmosphere. Thus, the term common noise will be used to refer to the shared noise sources which perturb the received signals. These are: the frequency standard, plasma noise, stochastic spacecraft motion, spacecraft transponder noise and half of the tropospheric scintillation, as described in Section 3.3. This indicates that the cross-correlations can be determined at each specific observation time by comparing the noise levels of the Doppler observables for each pair of ground stations.

The data from the ED045 RISE radio experiment, which consists of five observation passes measured from 10 receive-only stations over the course of the 2020 year, could be used to compare Doppler noise levels. Due to scarce data, there may be instances where the noise levels of two stations located far apart from one another are strongly correlated. To avoid these situations, the correlation metric should account for the distance between the two stations, as tropospheric and ionospheric noises differ between the two locations. As a result, the distance between the stations has a significant impact on how similar the weather effects (tropospheric and ionospheric noise sources) are at different locations. Therefore, the cross-correlations depend on two indicators: (1) the comparison of the weather effects and (2) the comparison of the Doppler noise levels. Considering that Filice (2019) utilizes a model with a fixed constant cross-correlation between all the ground stations, this indicates that the metric of Filice (2019) does not reflect reality. In order to account for the two different contributions that have been mentioned as well as for the different levels of signal correlations, the following metric is proposed:

$$\rho_{i,j} = w_{\text{weather}_{i,j}} \cdot \rho_{\text{weather}_{i,j}} + w_{\text{Doppler}_{i,j}} \cdot \rho_{\text{Doppler}_{i,j}} \quad (20)$$

where $\rho_{\text{weather}_{i,j}}$ and $\rho_{\text{Doppler}_{i,j}}$ are correlation coefficients of weather effects and Doppler noise levels, respectively, and $w_{\text{weather}_{i,j}}$ and $w_{\text{Doppler}_{i,j}}$ are the weighting factors associated to them, $w_{\text{weather}_{i,j}} + w_{\text{Doppler}_{i,j}}$=1. The weighting factor of the weather effect is the percentage determined by dividing the tropospheric noise by the total noise using the noise budget shown in Table 1. This means that the weather indicator is only effective when the solar plasma noise is low. To obtain a cross-correlation of the Doppler observables between 0 and 1, both $\rho_{\text{weather}_{i,j}}$ and $\rho_{\text{Doppler}_{i,j}}$ must be as well between 0 and 1.

Local noise sources depend on system properties, local observation geometry and meteorological conditions. The noise sources that contribute to meteorological conditions are the

ionospheric and tropospheric effects, which are very different on the downlink when the distance between stations is large. Therefore, the correlation coefficient for the weather indicator $\rho_{\text{weather}_{i,j}}$ has been modeled using the coordinates of the two ground stations (see Figure 5). As a result, the $\rho_{\text{weather}_{i,j}}$ has been characterized to decrease with increasing distance between ground stations and can be expressed as,

$$\rho_{\text{weather}_{i,j}} = \exp\left(-\frac{d_{i,j}}{2 \cdot d_{\text{ion}}}\right) \tag{21}$$

where $d_{i,j}$ is the distance between the two ground stations, and d_{ion} defines the maximum radius around a ground station for which the weather noises are similar. The smaller the ratio $d_{i,j}$ to $2d_{\text{ion}}$, the higher the correlation coefficient associated to weather effects between signals from different stations. According to Zhao et al. (2021), the ionospheric noise source detected from two different stations separated by 413 km is still similar using GNSS signals. Thus, the d_{ion} chosen is 413 km.

As introduced in this subsection, the Doppler observables received by multiple stations share some noise sources. When the noise levels of the received signals are significantly higher than the common noise, it indicates that the noises associated with instrumentation and systematic errors, as well as the propagation noises of the final segment of the downlink, are undoubtedly contrasting. Therefore, the greater the difference between the received signal and the common noise, the more the observations are uncorrelated. For the Doppler indicator, the correlation coefficient between noise levels has been modeled using the logistic function (S-shaped curve) as follows,

$$\rho_{\text{Doppler}_{i,j}} = \frac{2}{1 + \exp\left(m \cdot x_{i,j}\right)} \tag{22}$$

where m is the steepness of the function. In this case, m is set to be the logarithmic slope of the white noise in the Allan deviation curve (Rudyk et al. 2020), $10^{-\frac{1}{2}}$ in linear scale. Equation (22) gives, in a simplified matter, the correlation between the noise levels at two ground stations. The $x_{i,j}$ variable determines the difference between the two Doppler noises and the common noise and is defined as,

$$x_{i,j} = \frac{\varsigma_i + \varsigma_j - 2 \cdot \varsigma_{\text{common}}}{2\varsigma_{\text{common}} + 2\left(\varsigma_{\text{sun}} - \varsigma_{\text{sun}=\pi}\right)} \tag{23}$$

where ς_i and ς_j denote the total minimum noise observed at each station, $\varsigma_{\text{common}}$ is the fixed common noise when the solar plasma noise is minimum, and $\varsigma_{\text{sun}} - \varsigma_{\text{sun}=\pi}$ is the increment of the solar plasma noise. Equation (23) quantifies the ratio of the uncommon noise to the common noise of the two stations (including the solar plasma), as can be illustrated in Figure 7. This specific ratio indicates which of the two noises, the common background noise or the uncommon noise, is predominant. Equation (22) outputs a value between 0 and 1 since the variable $x_{i,j}$ is always greater than 0. The variables that define $x_{i,j}$ in Equation (23) are expressed as Allan deviations.

Both ς_i and ς_j can be taken from the five observations of the ED045 experiment (see Figure 5). The $\varsigma_{\text{common}}$ is the fixed common noise when the solar plasma is minimum. The fixed common noise is obtained by multiplying the received noise at a DSN station by the percentage of fixed background noise, which is determined by dividing the minimum common noise by the total noise using the noise budget shown in Table 1. The increment of solar plasma noise, which depends on the SEP angle and is time-dependent, is part of the total common noise.

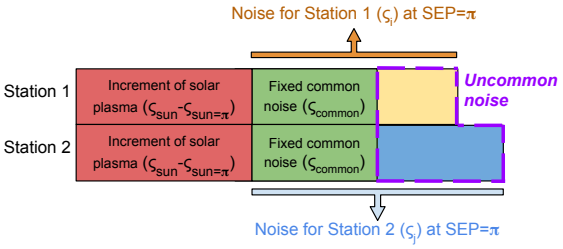

Figure 7. Classification of the parameters used in Equation (23).

5. Results and Discussion

Having described in depth the methodology and steps followed to perform the covariance analysis, this section contains a comprehensive discussion of the results obtained and a thorough comparison with previous data. First, a quality assessment of the real measurements from the five RISE radio science experiments is presented in Section 5.1. Part of these measurements are utilized for the composition of the lower-right quadrant of the weight matrix **W**, where the weights for LaRa observations are located. Furthermore, the outcome of the model developed to determine the correlation coefficients of the Doppler observables between the ground stations during the LaRa radio science experiments is analyzed in Section 5.2. As shown in Figure 5, the main two outputs of this analysis are the correlation matrices and the formal errors. Hence, the results of different correlation matrices and the interaction of the estimated parameters are discussed in Section 5.3. Lastly, Section 5.4 shows the achieved resolutions of the MOPs using the proposed model.

5.1. Fractional Frequency Deviation from InSight Measurements

The five observation passes from RISE radio science experiments, denoted ED045 experiment, are from a European VLBI Network project and were collected on the following dates: 22nd of February 2020, 29th and 30th of May 2020, and 21st and 22nd of October 2020. During these dates, the solar plasma noise should be close to its minimum. In the five experiments, eleven VLBI-equipped radio telescopes simultaneously tracked the signal from the RISE instrument. These are: Badary, Ceduna, Effelsberg, Hartrao, Irbene, Medicina, Onsala, Tian Ma, Dwingeloo, Wettzell, and Yebes. The data retrieved from the Irbene radio telescope are not included in the simulation since

only one observation pass was recorded where the signal post-processed was still very weak and noisy. It is important to remember that the received RF signal at the PRIDE stations passes through an open-loop architecture (see Section 3.2), and the output is the Doppler observables expressed in frequency domain. In order to determine the Doppler noise, the Doppler observables are post-processed by fitting a high order polynomial to the data using the SDtracker software (Calves et al. 2021). The fitting should remove the systematic noises. However, the presence of inherently time-correlated noises, such as propagation and instrumentation noises, implies that the Doppler noise may not be properly fit.

Since only PRIDE data of RISE observation passes along five days in 2020 are available, these Doppler observations are not included in the simulations for RISE radio science experiments. Hence, the RISE observations collected from radio telescopes are only analyzed with the aim of using part of them for the correlation metric when the PRIDE multi-station tracking strategy is employed, as mentioned in Figure 2. This implies that these PRIDE data from ED045 experiment are useful to determine the cross-correlations of the noise levels between ground stations for LaRa radio science experiments.

The modified Allan deviation of the noise is determined for each actual PRIDE observation and, in order to be in line with Table 1, the deviations are normalized with the carrier frequency. The well-known modified Allan deviation allows for the separation of white and flicker noise frequencies (Weiss et al. 1995). The modified version also provides information regarding the frequency stability, making the signal analysis more complete. For each receive-only station, the modified Allan deviation trend of the Doppler noise that has a slope closer to $-\frac{1}{2}$ is considered the most optimal, and these are shown in Figure 8. On the modified Allan deviation log-log plot, the white noise is recognized by a region of $-\frac{1}{2}$ slope.

Most of the observations present a negative slope of the modified Allan deviation. However, only the modified Allan deviation from the Medicina radio telescope has a precise slope of $-\frac{1}{2}$ in logarithmic scale (Weiss et al. 1995). This means that the observation measured by the Medicina radio telescope is only corrupted by white noise, and thus, the systematic noise sources are removed correctly. The rest of the measurements still contain systematic noise sources since they are random disturbances with a different power spectrum than white noise. The presence of residual noises of random nature will affect the subsequent covariance analysis leading to an underestimation of the formal errors. The presence of residual noise increases the uncommon noise for each station, which means that more cross-correlations tend to zero. Figure 8 shows that the Ceduna radio telescope contains the most residual noise.

The evaluation of the modified Allan deviation metric depends on the amount of data, and unfortunately, an entire observation pass commonly collects just hundreds of data points. Also, the modified Allan deviation is usually intended to estimate stability for larger time integrations, such as 1000 s in Armstrong (2006). The low whiteness of the data recorded in the radio telescopes is not surprising due to the scarce data,

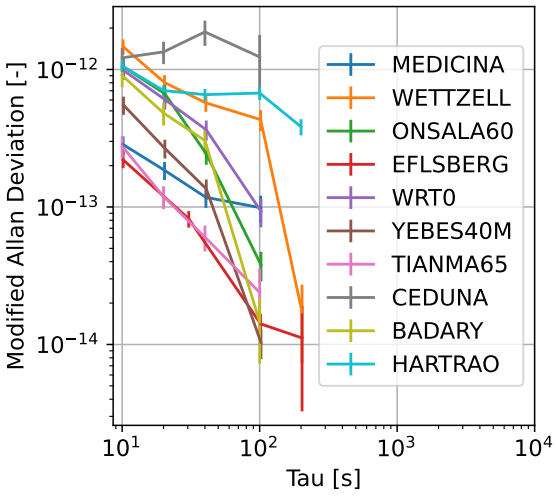

Figure 8. Modified Allan deviation of the Doppler noise with error bars as a function of the time integration τ for each radio telescope.

which can be seen from the maximum time integration τ and the error bars (see Figure 8). Besides this, there are propagation noise sources, such as tropospheric noise, which entail time dependencies. As a consequence of the presence of these noise sources, the post-processed data is not completely random. An improvement that would increase the whiteness of the data could be to model a couple of noise sources and remove them during the post-processing of the data. Implementing Notaro et al. (2020)'s time-delay mechanical noise cancellation technique into the post-processing of the Doppler noise could be a promising approach to reduce tropospheric and mechanical noises and improve PRIDE data quality.

For the determination of the correlation coefficients between the ground stations, an interpretation of the modified Allan deviation for each station is proposed. As the observations from RISE raw data[4] are sampled every 60 s, the time integration τ selected for inspecting the modified Allan deviation is 60 s. Hence, the modified Allan deviation of the Doppler noise evaluated at τ=60 s for each ground station is listed in Table 5. These variations will be the parameters used as fixed noise (ς_i or ς_j) in Equation (23) to evaluate the comparison of noise levels between ground stations.

The Doppler noise at τ=60 s for the DSN antennas (DSS-14, DSS-43, and DSS-63) is not collected during the ED045 experiment. Therefore, the Doppler noise has been taken from the standard deviation of the Doppler noise as a function of time presented in Buccino et al. (2022). The Doppler noise for the DSN is calculated for each day that the ED045 experiment is carried out. From the five days analyzed, the minimum noise for DSN stations was selected in order to have the least solar

[4] https://pds-geosciences.wustl.edu/missions/insight/rise.htm

Table 5. Doppler noise evaluated at τ=60 s for each station normalized with the carrier frequency.

Radio Telescope	Modified Allan Deviation [-]
MEDICINA	$1.19 \cdot 10^{-13}$
WETTZELL	$5.53 \cdot 10^{-13}$
ONSALA60	$1.46 \cdot 10^{-13}$
EFLSBERG	$6.60 \cdot 10^{-14}$
WRT0	$2.82 \cdot 10^{-13}$
YEBES40M	$1.03 \cdot 10^{-13}$
TIANMA65	$3.80 \cdot 10^{-14}$
CEDUNA	$2.45 \cdot 10^{-12}$
BADARY	$1.95 \cdot 10^{-13}$
HARTRAO	$7.12 \cdot 10^{-13}$
DSN	$2.56 \cdot 10^{-14}$

plasma noise. Among the radio telescopes, the lowest noise levels are found for the antennas that tend to have a higher SNR. The SNR is influenced by the diameter of the antenna dish and the power gain, which depends on the elevation angle of the receiver and the weather conditions. The Doppler noise levels of Effelsberg and Tian Ma radio telescopes are in the same order of magnitude as the one reported for the DSN antennas, since Effelsberg and Tian Ma antennas have 100 m and 65 m of antenna diameter, respectively.

5.2. Correlation Coefficients of the Doppler observables between Two Ground Stations

During LaRa radio science experiments, a total of 88 578 Doppler observables are simulated. Only 17 478 observations are planned to be collected from the DSN antennas. The vast majority of Doppler observables, precisely 71 100 observations, are expected to be received by radio telescopes around the world and transmitted by a DSN transmitter.

From the 88 578 LaRa observations, 213 956 combinations between ground stations can be retrieved. This indicates that the correlation metric is applied to all possible combinations between ground stations during LaRa radio science experiments. As shown in Figure 5, the correlation metric uses the coordinates of the ground stations, the noise budget, and the modified Allan deviation for each station given in Figure 8. The developed model depends on two indicators: (1) the comparison of the Doppler noise levels and (2) the comparison of the weather effects. In fact with this model, the more noise sources two ground stations have in common, the more the observations are correlated with each other. Also, the closer the ground stations are, the more the observations are correlated, as certain weather patterns are comparable.

The distribution of the 213 956 total correlation coefficients, Doppler noise and weather effects included, and the weighting factor associated with the weather effects used in the simulation can be seen in Figure 9. The behavior of each indicator is illustrated in Figure 10.

Figure 9 shows that the mean $\overline{\rho}_{i,j}$ and the median Med$(\rho_{i,j})$

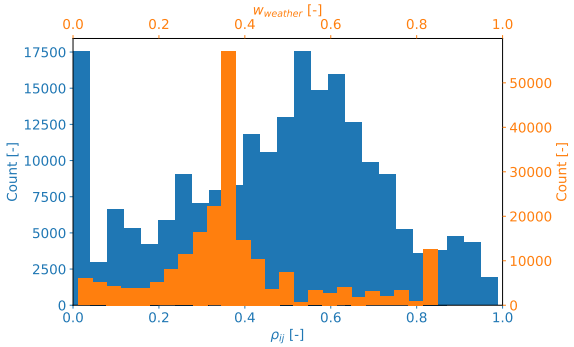

Figure 9. Histogram with the distribution of the correlation coefficient ρ_{ij} ( ) and the weighting factor $w_{weather}$ ( ).

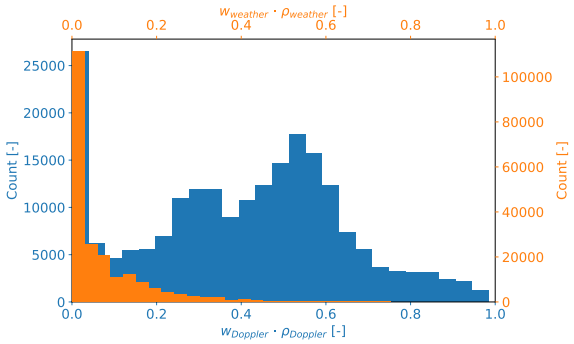

Figure 10. Histogram with the distribution of the two components of the final correlation coefficient, $w_{Doppler} \cdot \rho_{Doppler}$ ( ) and $w_{weather} \cdot \rho_{weather}$ ( ).

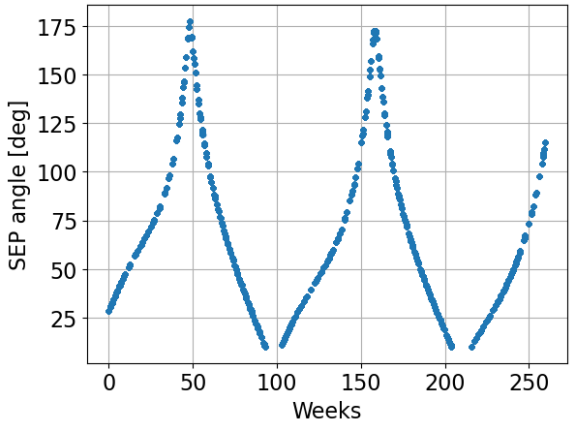

Figure 11. SEP angle as a function of time. The reference time is set on the day when ExoMars lander was expected to touch down on the Martian surface, 3rd of January 2022.

of all the correlation coefficients are 0.47 and 0.50, respectively. Both statistical values are close to the peak of the histogram. 17 500 of the cross-correlations are very close to 0, indicating that the Doppler observables are uncorrelated. This can be explained with the exponential function shown in Equation (21), where more than 100 000 combinations tend to 0 in the contribution of the weather indicator as seen in Figure 10. These values are consistent with the location of the radio telescopes depicted in Figure 3, in which it can be noticed that the radio telescopes are quite far apart. Another reason why the correlation coefficients lean to 0 for such a high number of combinations is that the uncommon noise is larger than the total common noise (see Equations (22) and (23)). This occurs when the received Doppler observables are collected while the solar plasma noise is at its lowest (SEP close to 180°).

On the contrary, Figure 9 illustrates that a large number of cross-correlations are close to the 0.6 value. This is due to the fact that when the SEP angle moves away from 180° and approaches the body avoidance angle, 10°, solar plasma noise becomes one of the dominating sources, as indicated in Table 1. Thus, the signals become noisier, and at the same time, the Doppler observations between ground stations become more correlated as the total common noise increases significantly (see Equations (22) and (23)).

Moreover, the behavior of the weighting factor shown in Figure 9 resembles a normal distribution with a peak around 0.35. The peak is observed once the SEP angle is close to 90°, which is one of the most often occurring as illustrated in Figure 11.

With the histograms, only an overall overview can be investigated. In order to provide further insights on the different ground stations correlations, a heat map with the mean correlation coefficients between ground stations as shown in Figure 12.

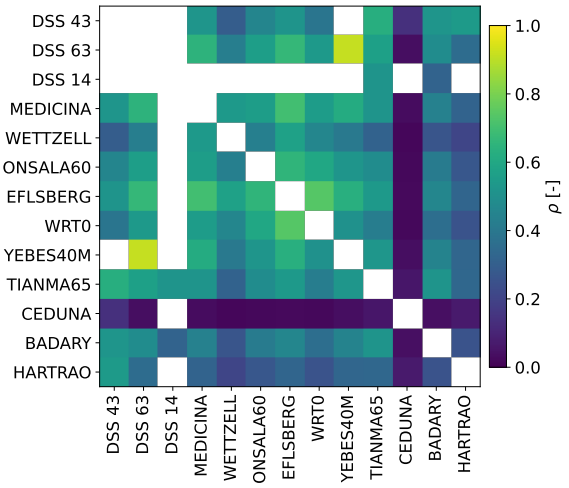

Figure 12. Mean of the correlation coefficients between ground stations shown as a correlation matrix.

Here, it can be seen that Yebes and DSS-63 (DSN ground facility in Madrid) antennas have a mean correlation coefficient of 0.91, which is very high. These two specific ground stations are less than 100 km distant from each other (see Figure 3), meaning that most of the downlink signal is perturbed by the same ionospheric noise sources. The Ceduna radio telescope shows the lowest correlation with most of the ground stations because the Doppler noise is the largest compared to the other antennas, see Table 5. Since Ceduna and DSS-43 antennas are located in Australia, this is the only combination in which the correlation coefficient is larger than 0.1. The mean correlation coefficient for the remaining combinations is close to the overall average correlation coefficient. The white squares in Figure 12 denote a lack of interaction for those specific combinations. This mostly happens to the DSS-14 antenna situated in Goldstone, since there are no additional stations located on the American continent. Most of the radio telescopes owned by JIVE are part of the European VLBI Network[5], and unfortunately, these stations are not spread all around the world, but are mainly located in Europe.

Surprisingly, observations that have been transmitted from Oceania can be received by most of the stations in Europe. This is due to the fact that the rotation of the Earth is prograde and the round-trip delay time is about 13 min. Between DSN antennas there cannot be a correlation, because only one signal can be transmitted at each time and the longitude between the stations is precisely 120° (Deutsch et al. 2016).

5.3. Correlation between Estimated Parameters

The correlation matrix between the 42 estimated parameters is computed using the covariance matrix **P** defined in Section 4.3 and the formal errors, which are discussed in further detail in Section 5.4. For the purpose of determining this correlation matrix, each term of the covariance matrix **P** is associated with two estimated parameters (or twice with a single estimated parameter) and normalized with the formal errors associated to them, $\frac{P_{i,j}}{\sigma_i \sigma_j}$. The correlation matrix can be used as a graphical representation of the interconnections between the estimated parameters. If the value of the correlation matrix associated with a given pair of estimated parameters is close to 1 or -1, it indicates that there is a substantial dependency between them.

Three different correlation matrices between the estimated parameters are plotted in Figures 13 to 15, where the indices of the estimated parameters are listed in Table 6. In case the initial state, i.e., the first six estimated parameters, are removed from the correlation matrix, the correlation between MOPs does not bring any outstanding changes.

Figures 13 and 14 show the correlation matrices in a single-lander configuration evaluated at the end of each mission. Figure 13 corresponds to the correlation matrix for RISE radio science experiments, which ends on the 21st of August 2021, whereas Figure 14 is the correlation matrix for LaRa radio science experiments which is expected to generate data from the 3rd of January 2022 until the end of the 2026 year. This

[5] http://old.evlbi.org/

Table 6. Indices of the estimated parameters.

0	1	2	3	4	5	6	7	8	9	10	11	12	13	14	15	16	17	18	19	20	21	22	23	24	25	26	27	28	29	30	31	32	33	34	25	26	27	28	29	40	41
x	y	z	$\dot{x}$	$\dot{y}$	$\dot{z}$	F	σ_{FCN}	x_{RISE}	y_{RISE}	z_{RISE}	x_{LaRa}	y_{LaRa}	z_{LaRa}	ϕ_1^c	ϕ_1^s	ϕ_2^c	ϕ_2^s	ϕ_3^c	ϕ_3^s	ϕ_4^c	ϕ_4^s	X_{p1}^c	X_{p1}^s	Y_{p1}^c	Y_{p1}^s	X_{p2}^c	X_{p2}^s	Y_{p2}^c	Y_{p2}^s	X_{p3}^c	X_{p3}^s	Y_{p3}^c	Y_{p3}^s	X_{pC}^c	X_{pC}^s	Y_{pC}^c	Y_{pC}^s	X_{p4}^c	X_{p4}^s	Y_{p4}^c	Y_{p4}^s

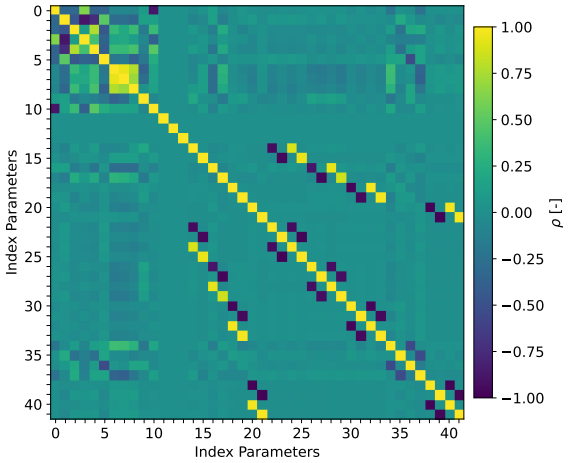

Figure 13. Correlation matrix in a one-lander configuration evaluated at end of the InSight mission. The labels of each index can be found in Table 6.

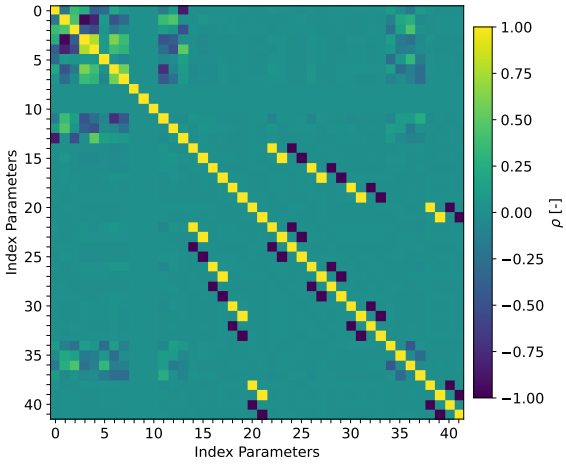

Figure 14. Correlation matrix in a one-lander configuration evaluated at the end of the ExoMars mission without taking into account RISE measurements. The labels of each index can be found in Table 6.

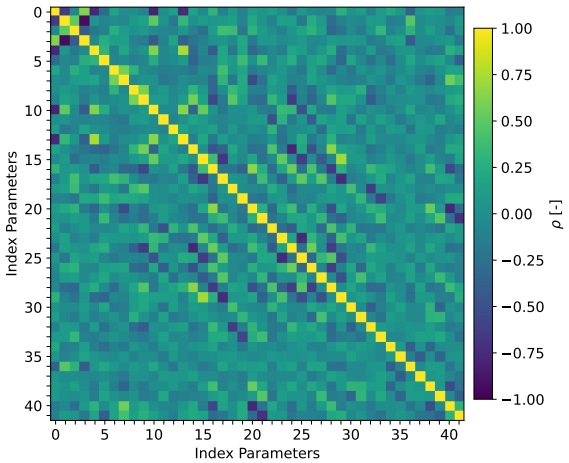

Figure 15. Correlation matrix in a two-lander configuration evaluated at the end of the ExoMars mission. The labels of each index can be found in Table 6.

implies that Figure 13 only utilizes RISE data, and Figure 14 14 exclusively uses LaRa data. Since both correlation matrices are evaluated in a one-lander configuration, it can be seen that the two correlation matrices are almost identical.

In both plots, there is a strong correlation between the core factor F and the free core nutation rate σ_{FCN}. This is due to the fact that these the rotational variations depend on F and σ_{FCN} on a similar manner. Theoretically, the pair can be expressed as a function of the moment of inertia of Mars as shown below (Sasao et al. 1980),

$$F = \frac{C_f}{C - C_f}\left(1 - \frac{\gamma}{e}\right), \tag{24}$$

$$\sigma_{\mathrm{FCN}} = -\Omega_0 \frac{C_f}{C - C_f}\left(e_f - \beta\right) \tag{25}$$

where C and C_f are the polar moments of inertia of Mars and fluid core, e and e_f are the dynamical flattenings of Mars and fluid core, γ is the compliance related to the deformation of Mars, Ω_0 is the constant diurnal angular velocity of Mars, and β is the compliance related to the contribution of the deformation at the core-mantle boundary (Yseboodt, Barriot, and Dehant 2003). F and σ_{FCN} is, as well, slightly correlated to the polar motion parameters at the Chandler frequency. This can is interpreted by the comparable periods, in which the theoretical amplitudes of the FCN period and the Chandler period are 247 and 207 days, respectively (Van Hoolst et al. 2000a).

Moreover, the sine and cosine terms of the X_p and Y_p component of the polar motion for the same frequency are anti-correlated with each other, and these correlations are parallel to the diagonal of the correlation matrix. Since the X_p and Y_p components are the projection of the same phenomenon, these estimated parameters are strongly correlated. The projection can be seen in Equations (5) and (6). Then, the X_p components of the polar motion are solidly correlated with the spin variation parameters relative to the same order and frequency. Whereas, the Y_p components of the polar motion are greatly anti-correlated with the spin variation parameters relative to the unchanging order and frequency. This can be explained with the following expressions (Mueller 1969),

$$\Delta\lambda = \big(Y_p \cos(\lambda) - X_p \sin(\lambda)\big) \tan(\theta), \tag{26}$$

$$\Delta\theta = X_p \cos(\lambda) + Y_p \sin(\lambda) \tag{27}$$

where λ and θ are the latitude and longitude of the lander, respectively. Due to polar motion, the position of the lander changes slightly and its variation can be calculated with the expressions above. As there is no spin variation parameter evaluated at the Chandler frequency, the X_p and Y_p components at this frequency are not correlated with any spin variation parameters.

In addition, it is important to note how the z-coordinate with respect to the lander position is correlated to the x-coordinate of the initial state for both correlation matrices. Nevertheless, the two matrices shown in Figures 13 and 14 have a few differences. In the InSight-lander configuration, the ExoMars lander coordinates are not correlated with the other parameters. On the contrary, InSight lander coordinates are not correlated with the rest of the parameters in the ExoMars-lander configuration. The reason is that these parameters do not vary with time but remain equal to the initial values during each simulation.

When the two missions are combined, the correlation matrix changes completely (see Figure 15). The correlation matrix takes into account RISE and LaRa radio science experiments and is evaluated at the end of ExoMars mission, precisely, the last day of the 2026 year. Figure 15 shows that there is a strong de-correlation of the values that were highly correlated in a one-lander configuration. On the other hand, many of the estimated parameters that were not correlated at all in the one-lander configuration appear to be slightly correlated in the two-lander configuration. This is due to the greater data set that is being used for the analysis. Including more data allows for the covariance analysis to detect more interdependencies among the estimated parameters. Another behind the de-correlation observed between certain parameters with respect to the one lander configuration is the landers relative location. Since the two landers are opposite of each other (InSight longitude = 135.62°E and ExoMars longitude = 335.37°E), this will probably reduce the correlation between parameters. This can be explained with the reduction of the variations of station latitude and longitude (see Equations (26) and (27)) are significantly reduced when the expressions become a linear combination of two landers.

An important remark is that the polar motion parameters should be de-correlated even more if the two landers (InSight latitude = 4.5°N and ExoMars latitude = 18.3°N) are opposite of each other as well in latitude. This is due to the fact that a moderate correlation can be seen on the annual, semiannual, terannual, and quaterannual polar motion parameters (see Figure 15). Hence, the advantages from combining data from several landers depends on the relative location between them, as the uncertainty in some parameters can decrease due to a low correlation between the observations.

Furthermore, the annual, semiannual, terannual, and quaterannual polar motion parameters in the one-lander configuration are correlated with two parameters, the opposite component and the spin variation parameters of the same order (see Figures 13 and 14). Since they are strongly correlated with two terms, the de-correlation observed in the two-lander configuration will lead to a fast decrease in the standard deviation of the MOPs associated with the polar motion. This will be more clear when discussing the behavior of the estimated parameters which will be presented in the next subsection.

5.4. MOPs Resolution

The standard deviations of the 30 MOPs uncertainties are computed using Equation (16) and plotted as a function of time in Figure 16. The black dashed line indicates the beginning of the LaRa experiment. All the MOPs accuracies are improved when a network of two landers is applied. All the parameters during the first weeks are very close to the a priori uncertainties (see Table 4). This can be explained with Equation (17), where $\mathbf{P}_0^{-1}$ matrix dominates over the $\mathbf{H}^T\mathbf{W}\mathbf{H}$ matrix. Most of the uncertainties start to decrease swiftly after a couple of months when the $\mathbf{H}^T\mathbf{W}\mathbf{H}$ matrix becomes predominant in the covariance analysis.

The results reported in Figure 16 show a faster reduction with time of the uncertainties in the core factor F, the free core nutation rate σ_{FCN}, the 4 polar motion parameters at the Chandler frequency, and the 8 spin variation parameters with respect the other 16 polar motion parameters. There is a high correlation between these 16 polar motion parameters in a lander configuration, and they are also correlated with the spin variation parameters (see Figures 13 and 14). This implies that these polar motion parameters, with the exception of those at the Chandler frequency, are more limited than the other MOPs, or that knowledge of these parameters is worse as a result of the aforementioned correlations. The lower dependency of the polar motion parameters at the Chandler frequency is the reason why a faster reduction of their uncertainties is observed.

Before the start of the LaRa radio science experiment, the accuracy of the free core nutation rate σ_{FCN} has improved by 98 % with respect to the a priori value (1.5 deg/day). The uncertainties of the core factor F, the 8 spin variation parameters, and the polar motion parameters at the Chandler frequency have decreased on average by 70 %, 80 %, and 86 % respectively with reference to the initial uncertainty. On the contrary, the uncertainty of the other 16 polar motion parameters has

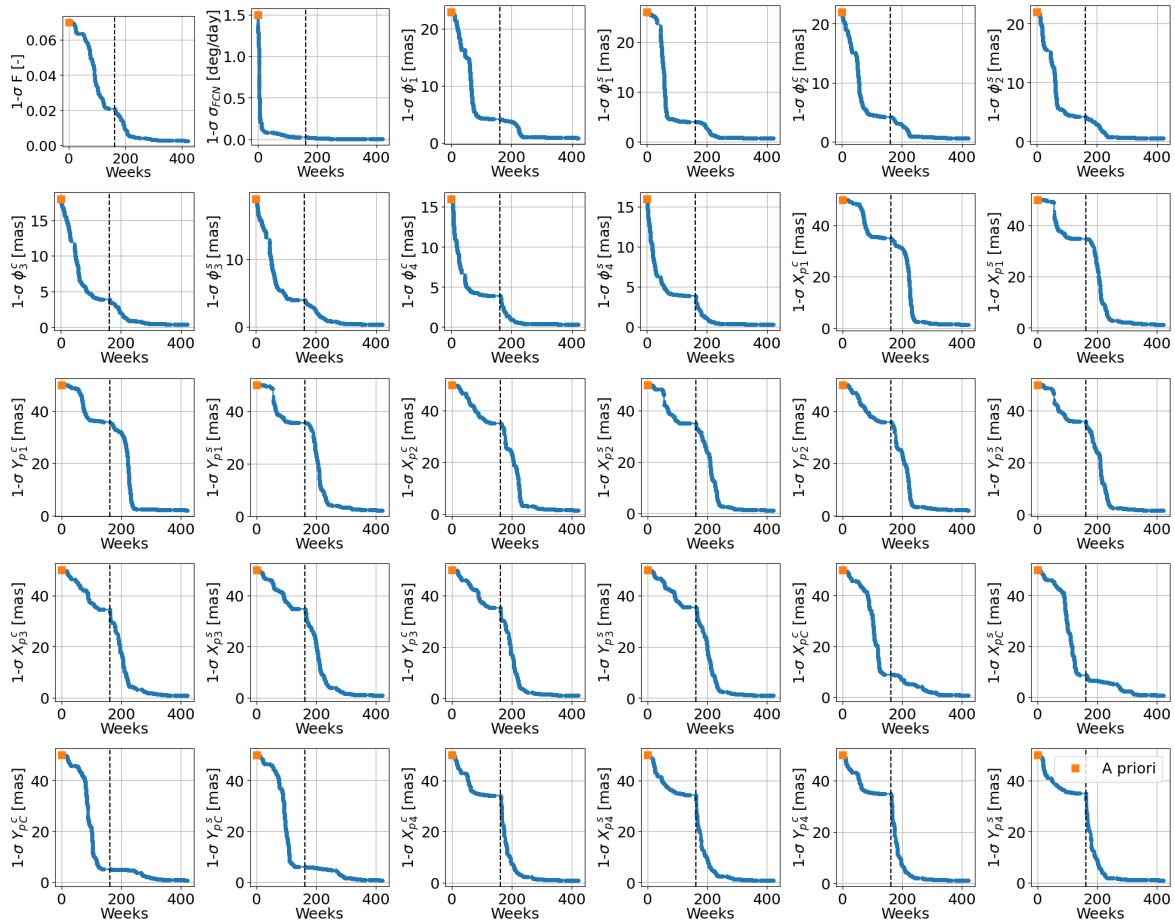

Figure 16. Evolution of the standard deviation of the MOPs uncertainties with respect to time. The reference time is set on the day when InSight lander arrived on the Martian surface. The black dashed line separates the RISE and LaRa radio science experiments. See Table 4 to identify the a priori values of the MOPs.

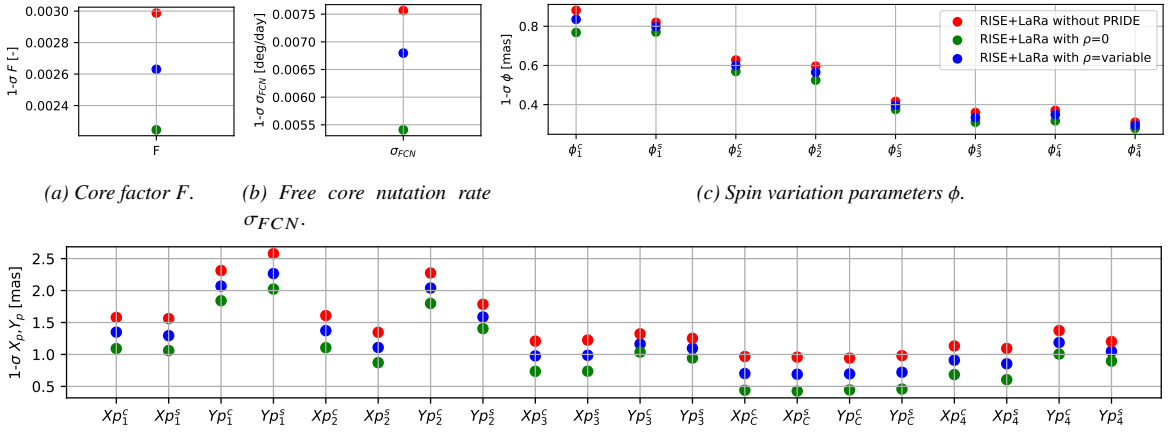

(a) Core factor F. *(b) Free core nutation rate σ_{FCN}.* *(c) Spin variation parameters ϕ.*

(d) Polar motion parameters X_p, Y_p.

Figure 17. Final formal errors of the MOPs obtained from different sets of configurations.

been reduced by around 30 % in relation to the a priori value (50 mas).

The LaRa experiment begins on week 160. From this moment on, the InSight and LaRa data are combined to retrieve more accurate MOPs estimations. Since receive-only stations are added in the LaRa radio science experiment, much more data points are gathered as described in Section 5.2. 23 728 observations are recorded during the RISE radio science experiment whereas 88 578 measurements are simulated during the LaRa radio science experiment. The accuracy of the polar motion parameters estimations is greatly improved when introducing the extensive data from the LaRa experiment. Figure 16 depicts that the MOPs uncertainties converge a few years after the beginning of this second mission. The time gap between the two experiments is about 16 weeks. The other small time gaps are caused by the solar conjuctions.

Combining the two experiments, Figure 16 shows that the uncertainty is lower for a two-lander configuration in comparison with a one-lander configuration (InSight-lander configuration). As it was discussed above, the accuracies for the 16 polar motion parameters are the most enhanced, about 96 % with respect to the one-lander configuration. This is caused by the de-correlation of these estimated parameters as illustrated in Figure 15. Interestingly, the de-correlation has slightly decreased the slope of the uncertainty reduction of the free core nutation rate σ_{FCN} (see Figure 16). However, a reduction of about 74 % in the uncertainty of this MOP was reached with respect to the one-lander configuration estimation. On the other hand, although the uncertainties in the core factor F, the 4 polar motion parameters at the Chandler frequency, and the 8 spin variation parameters decrease at a lower pace, they have been reduced on average by 87 %, 87 %, and 89 % respectively when compared to the one-lander configuration. During the last 100 weeks, MOPs slowly converge and their final formal errors are reported in Figure 17.

Moreover, the formal errors of two more tracking scenarios are shown in Figure 17. The correlation coefficients between ground stations during the LaRa radio science experiment are set to be fixed and constant in these added simulation configurations. One tracking scenario is simulated with correlation coefficients $\rho_{i,j}$ equal to 1, and the other one with correlation coefficients $\rho_{i,j}$ corresponding to 0. When all the observations between different ground stations are fixed to correlate with $\rho_{i,j}$=1, it means that adding the receive-only stations does not bring new data to the covariance analysis. Therefore, adding more observations from other ground stations when they are fully correlated should not influence the final formal errors. Nevertheless, the weighting matrix $\mathbf{W}$ becomes a diagonal matrix when all the observations are uncorrelated, determining that the uncertainties decrease even more, and this gives more effective information to the estimator.

Figure 17 shows that the formal errors achieved using the developed metric are just in between the two extreme scenarios. This observation is consistent with the average correlation coefficient $\overline{\rho}_{i,j}$ of 0.47 reported in Section 5.2. Furthermore, the plots indicate that the MOPs accuracies are enhanced when the 10 receive-only antennas during the LaRa radio science experiment are included in the simulation. The accuracy improvement of the core factor F, free core nutation rate σ_{FCN}, 4 polar motion parameters at the Chandler frequency, 8 spin variation parameters, and the other 16 polar motion parameters is 12 %, 10 %, 25 %, 5 %, and 15 %, compared to the simulation where only DSN antennas are used (labeled as "RISE + LaRa ρ=1"). More precisely, all the uncertainties have decreased by more than 10 times the a priori value with the covariance analysis. The uncertainties of the core factor F, the free core nutation rate σ_{FCN}, the 8 spin variation parameters, and the 20 polar motion parameters converge, respectively, to 0.0026, 0.0068 deg/day, 0.52 mas, and 1.2 mas.

Some of these results have been compared with previous works in the literature. In Yseboodt, Barriot, Dehant, and Rosenblatt (2004), the estimated final precision of the core factor F, the spin variation parameters, and the polar motion parameters are 0.006, 3 mas, and 2 mas, respectively. These uncertainties are relatively close to those presented. The differences observed may stem from the fact that these results were obtained using observation data prior to InSight mission, with four landers. Next, in Peters et al. (2020), the MOPs uncertainties are also estimated using InSight and ExoMars with a two-lander configuration. Unfortunately, the set of MOPs used are slightly different and the only uncertainties that can be compared are the spin variation parameters. For the annual and semi-annual spin angles, the final uncertainties are both 8 mas, which are slightly above those reported here. These results are based on simulations using Doppler observations from a period of time of 4 years, which is a half of that used in this work, and without any receive-only stations. This makes a straight comparison difficult and may explain the slight differences observed.

It is worth noting that the covariance analysis depends significantly on the number of estimated parameters. If the initial state, defined by the first six estimated parameters, had been removed from the covariance analysis, the uncertainty of the MOPs would have been even smaller. In this case, the polar motion parameters, the core factor F and the free core nutation rate σ_{FCN} uncertainties would have decreased by 9 % and 11 % with respect to the uncertainties of the covariance analysis when the initial state is estimated. On the other hand, the accuracy of the 8 spin variation parameters improves overall by 16 % in comparison when 42 estimated parameters are utilized in the covariance analysis. When the initial state is omitted, the covariance analysis becomes slightly optimistic since the Mars ephemeris error is ignored.

Lastly, the evolution of the standard deviation of the initial state and lander positions have similar behavior to the spin variation parameters, where in both experiments separately the uncertainty is decreased significantly. As the Doppler observations are not sensitive to the z-axis, only the z-coordinates and $\dot{z}$-velocity behave differently from the others. This indicates that the accuracies along the spin axis are enhanced than the accuracies along the equatorial plane. In order to improve the accuracy of the z-components, Le Maistre (2016) proposed a

method that entails inferring the z-coordinates using precise estimations of the in-equatorial plane coordinates from radio tracking and a high-resolution topography model of Mars.

6. Conclusion

This paper proposes a novel covariance-based method that improves the MOPs accuracy by combining Doppler observations in a two-lander configuration and including a network of receive-only stations. This investigation brings valuable insights into the origin and internal structure of Mars. In particular, the advantages of using the PRIDE technique for signal post-processing were investigated. This method is one of the most promising approaches to extend the current, and limited, knowledge about the Red planet.

The proposed combination of two landers has shown to improve the accuracy of the Mars rotational state estimation, in line with what was observed in Peters et al. (2020). The results reported in this paper have been obtained assuming a touchdown date of the ExoMars lander in January 2022. Unfortunately, this mission has been put on hold due to the ongoing conflict in Ukraine, with no foreseen launch date in the near-future. Nevertheless, the integration of the Doppler observations of a delayed ExoMars mission is possible, and therefore, the developed PRIDE-based method remains valid. However, if the integration of the ExoMars observation data is made later, most probably several years, the proposed method would have to be applied using a precise propagator of the rotational state and orbital position. This is to avoid that the obtained uncertainties of the MOPs get affected by the errors introduced by the propagator.

With a total of 23 728 real InSight-RISE observations and 88 578 simulated ExoMars-LaRa observations generated using TUDAT, this study has shown that the interplay between the MOPs observed separately for these two missions is very similar. The strong correlations between X_p and Y_p components of the polar motion parameters, and those between the polar motion parameters and the spin variation parameters relative to the same order and frequency seen in the one-lander configuration, are significantly relaxed when these two radio science experiments are combined. One of the main reasons behind these lower correlations is the optimal placement of both landers on the Red Planet's surface. The longitude plays a strong role and they are located at completely opposite longitudes, thus providing fully complementary Doppler observations to analyze optimally the rotational state of Mars. The advantage of the two-lander configuration can be clearly seen in the reduction of the polar motion parameters uncertainty, which is reduced by 96 % with respect to the one-lander configuration. This considerable reduction is observed for all polar motion parameters except for those evaluated at the Chandler frequency. Overall, the uncertainties of the MOPs in a two-lander configuration are reduced by around 92 % when compared to the one-lander configuration on average. These results have been compared quantitatively with previous work, and the uncertainties reported in Yseboodt, Barriot, Dehant, and Rosenblatt (2004) are relatively close to those presented.

Regarding the added value of integrating PRIDE data collected with a network of receive-only stations, which are combined with the observations from the DSN ground stations, this work has proven that it can reduce significantly the uncertainties of the MOPs. In this scenario, the greatest improvement in accuracy is reported for the polar motion parameters at the Chandler frequency, which is around 25 % with respect to the tracking scenario when only DSN ground stations are used. On the contrary, the uncertainties of the core factor F, free core nutation rate σ_{FCN}, 4 polar motion parameters at the Chandler frequency, 8 spin variation parameters, and the other 16 polar motion parameters are reduced by 12 %, 10 %, 25 %, 5 %, and 15 % in comparison when two-way Doppler links with DSN antennas are employed. The addition of the PRIDE data from receive-only stations allowed a much faster convergence of the formal errors. The enlarged data set thus led to a more robust covariance analysis. Unfortunately, the JIVE's radio telescopes are mainly located over Europe. Therefore, this study should be extended to include radio telescopes spread all over the world to see how this larger network could enhance the science return.

Furthermore, a metric for determining the cross-correlations of the Doppler observables between Earth-based ground stations is developed and discussed in Section 4.5. Since the signal transmitted from a DSN antenna can be received by several radio telescopes, the signals collected at different radio telescopes cannot be assumed to be uncorrelated and a representative correlation metric was missing in the literature. Two indicators are considered in the proposed metric, (1) the comparison of noise levels, and (2) the comparison of the ionospheric and tropospheric effects. For the first indicator, real Doppler observations of RISE radio science experiments collected during five dates of the 2020 year at ten receive-only stations have been analyzed. The time-dependent developed model gives, in a simplified matter, the correlation between noise levels at two ground stations. In this metric, the modified Allan deviations evaluated at integration time equal to 60 s for each receive-only antenna are retrieved. By increasing the integration time, the model would become more robust as the Allan deviations become more accurate. Further improvements on the collected measurements are required, being one of them fitting the Doppler residual using a higher order polynomial in order to reduce the systematic noises seen in the real measurements.

Last but not least, the findings from the comprehensive and extensive analysis performed have confirmed that combining data from different Mars-based landers and adding more Earth-based receive-only stations reduces the uncertainty of the MOPs. However, this analysis has been made without having had access to real observation data from the ExoMars lander. The proposed method to retrieve the uncertainties of the MOPs can be refined and further improved to be able to integrate ExoMars observations when they are made available.

References

Armstrong, JW (2006). "Low-frequency gravitational wave searches using spacecraft Doppler tracking". In: *Living Reviews in Relativity* 9.1, pp. 1–59.

Bocanegra-Bahamon, T (Mar. 2019). "Planetary Radio Interferometry and Doppler Experiment (PRIDE) for radio occultation studies: A Venus Express test case". PhD thesis. Faculty of Aerospace Engineering: Delft University of Technology.

Bocanegra-Bahamon, T, GM Calves, LI Gurvits, G Cimo, et al. (2019). "Venus Express radio occultation observed by PRIDE". In: *Astronomy & Astrophysics* 624, A59.

Bocanegra-Bahamon, T, GM Calves, LI Gurvits, DA Duev, et al. (2018). "Planetary radio interferometry and Doppler experiment (PRIDE) technique: a test case of the mars express phobos flyby-II. Doppler tracking: formulation of observed and computed values, and noise budget". In: *Astronomy & Astrophysics* 609, A59.

Buccino, D et al. (2022). "Low-SNR Doppler Data Processing for the InSight Radio Science Experiment". In: *Remote Sensing* 14.8, p. 1924.

Calves, GM et al. (2021). "High spectral resolution multi-tone Spacecraft Doppler tracking software: Algorithms and implementations". In: *Publications of the Astronomical Society of Australia* 38.

Cottaar, S and P Koelemeijer (2021). "The interior of Mars revealed". In: *Science* 373.6553, pp. 388–389.

Dehant, V et al. (2020). "The radioscience LaRa instrument onboard ExoMars 2020 to investigate the rotation and interior of mars". In: *Planetary and Space Science* 180, p. 104776.

Deutsch, LJ et al. (2016). "Deep space network: The next 50 years". In: *14th International Conference on Space Operations*, p. 2373.

Dirkx, D (2015). "Interplanetary Laser Ranging. Analysis for Implementation in Planetary Science Missions". In: *Ph. D. Thesis*.

Duev, DA et al. (2012). "Spacecraft VLBI and Doppler tracking: algorithms and implementation". In: *Astronomy & Astrophysics* 541, A43.

Filice, V (2019). "Analysis of PRIDE contribution to ExoMars-LaRa experiment". MA thesis. Rome, Italy: University of Rome "La Sapienza".

Folkner, W et al. (2016). "Models and Measurements of the Rotation of Mars". In: *AGU Fall Meeting Abstracts*. Vol. 2016, G51C–05.

Iess, L et al. (2012). "Improved Doppler tracking systems for deep space navigation". In: *International Symposium on Space Flight Dynamics (ISSFD)*.

Kahan, D et al. (2021). "Mars precession rate determined from radiometric tracking of the InSight Lander". In: *Planetary and Space Science* 199, p. 105208.

Kahn, RD et al. (1992). "Position determination of a lander and rover at Mars with Earth-based differential tracking". In: *The Telecommunications and Data Acquisition Report*.

Konopliv, AS, RS Park, and W Folkner (2016). "An improved JPL Mars gravity field and orientation from Mars orbiter and lander tracking data". In: *Icarus* 274, pp. 253–260.

Konopliv, AS, RS Park, A Rivoldini, et al. (2020). "Detection of the Chandler wobble of Mars from orbiting spacecraft". In: *Geophysical Research Letters* 47.21, e2020GL090568.

Konopliv, AS, CF Yoder, et al. (2006). "A global solution for the Mars static and seasonal gravity, Mars orientation, Phobos and Deimos masses, and Mars ephemeris". In: *Icarus* 182.1, pp. 23–50.

Kuchynka, P et al. (2014). "New constraints on Mars rotation determined from radiometric tracking of the Opportunity Mars Exploration Rover". In: *Icarus* 229, pp. 340–347.

Le Maistre, S (2013). "The rotation of Mars and Phobos from Earth-based radio-tracking observations of a lander". PhD thesis. UCL-Université Catholique de Louvain.

– (2016). "InSight coordinates determination from direct-to-Earth radio-tracking and Mars topography model". In: *Planetary and Space Science* 121, pp. 1–9.

Le Maistre, S, A Rivoldini, et al. (2021). "Preliminary results of one Martian year of observations from the radio-science experiment of InSight, RISE". In: *52nd Lunar and Planetary Science Conference*. 2548, p. 2011.

Le Maistre, S, P Rosenblatt, V Dehant, et al. (2018). "Mars rotation determination from a moving rover using Doppler tracking data: What could be done?" In: *Planetary and Space Science* 159, pp. 17–27.

Le Maistre, S, P Rosenblatt, A Rivoldini, et al. (2012). "Lander radio science experiment with a direct link between Mars and the Earth". In: *Planetary and Space Science* 68.1, pp. 105–122.

Mueller, II (1969). "Spherical and practical astronomy, as applied to geodesy". In: *New York*.

Notaro, V et al. (2020). "Reducing Doppler noise with multi-station tracking: The Cassini test case". In: *Acta Astronautica* 173, pp. 45–52.

Pallichadath, V et al. (2020). "PRIDE: Ground-based VLBI observations for Spaceborne Probes". In: *European Planetary Science Congress*, EPSC2020–647.

Peters, MJ et al. (2020). "LaRa after RISE: Expected improvement in the Mars rotation and interior models". In: *Planetary and Space Science* 180, p. 104745.

Rudyk, AV et al. (2020). "Strapdown inertial navigation systems for positioning mobile robots-mems gyroscopes random errors analysis using allan variance method". In: *Sensors* 20.17, p. 4841.

Sasao, T, S Okubo, and M Saito (1980). "A simple theory on the dynamical effects of a stratified fluid core upon nutational motion of the Earth". In: *Symposium-International Astronomical Union*. Vol. 78. Cambridge University Press, pp. 165–183.

Schutz, B, B Tapley, and GH Born (2004). *Statistical orbit determination*. Elsevier.

Shan, Q et al. (2018). "Improving the Accuracy of the Martian Ephemeris Short-Term Prediction". In: *Advances in Astronomy* 2018.

Van Hoolst, T, V Dehant, and P Defraigne (2000a). "Chandler wobble and free core nutation for Mars". In: *Planetary and Space Science* 48.12-14, pp. 1145–1151.

Van Hoolst, T, V Dehant, and P Defraigne (2000b). “Sensitivity of the Free Core Nutation and the Chandler Wobble to changes in the interior structure of Mars”. In: *Physics of the Earth and Planetary Interiors* 117.1-4, pp. 397–405.

Weiss, MA et al. (1995). “Confidence on the modified Allan variance and the time variance”. In: *Proceedings of the 9th European Frequency and Time Forum (EFTF)*, pp. 8–10.

Yseboodt, M, JP Barriot, and V Dehant (2003). “Analytical modeling of the Doppler tracking between a lander and a Mars orbiter in terms of rotational dynamics”. In: *Journal of Geophysical Research: Planets* 108.E7.

Yseboodt, M, JP Barriot, V Dehant, and P Rosenblatt (2004). “Uncertainties on Mars Interior Parameters Deduced from Orientation Parameters Using Different Radio-Links: Analytical Simulations”. In: *Lunar and Planetary Science Conference*, p. 1643.

Zhao, L, J Dousa, and P Vaclavovic (2021). “Accuracy evaluation of ionospheric delay from multi-scale reference networks and its augmentation to PPP during low solar activity”. In: *ISPRS International Journal of Geo-Information* 10.8, p. 516.

A. Derivations

A.1. Rotation Conventions

R_x, R_y and R_z are elemental rotation matrices which each one is a rotation about one of the axes. The rotation angle is defined as α and is rotated clockwise about $x-$, $y-$ or $z-$axis. The three basic rotation matrices are expressed as follows,

$$\mathbf{R}_x(\alpha) = \begin{bmatrix} 1 & 0 & 0 \\ 0 & \cos(\alpha) & -\sin(\alpha) \\ 0 & \sin(\alpha) & \cos(\alpha) \end{bmatrix}, \quad (28) \qquad \mathbf{R}_y(\alpha) = \begin{bmatrix} \cos(\alpha) & 0 & \sin(\alpha) \\ 0 & 1 & 0 \\ -\sin(\alpha) & 0 & \cos(\alpha) \end{bmatrix}, \quad (29) \qquad \mathbf{R}_z(\alpha) = \begin{bmatrix} \cos(\alpha) & -\sin(\alpha) & 0 \\ \sin(\alpha) & \cos(\alpha) & 0 \\ 0 & 0 & 1 \end{bmatrix}. \quad (30)$$

A.2. Prograde and Retrograde Terms

The periodic motion of the spin axis can be expressed in prograde p_m and retrograde r_m terms, which at the same are dependent to the nutation parameters described in Section 2 (Le Maistre 2013). This expression can be expressed as follows,

$$p_m e^{2i\pi f_m t} + r_m e^{-2i\pi f_m t} = \delta I_m + i \sin(I_0)\delta\psi_m. \quad (31)$$

The prograde and retrograde terms contain the real and imaginary parts. As a result, substituting these terms for $p_m = p_m^{\Re} + ip_m^{\Im}$ and $r_m = r_m^{\Re} + ir_m^{\Im}$ in Equation (31) (Le Maistre 2013). One can achieve each term which can be expressed as,

$$p_m^{\Re} = \frac{I_m^c + \sin(I_0)\psi_m^s}{2}, \quad (32) \qquad r_m^{\Re} = \frac{I_m^c - \sin(I_0)\psi_m^s}{2}, \quad (33) \qquad p_m^{\Im} = \frac{-I_m^s + \sin(I_0)\psi_m^c}{2}, \quad (34) \qquad r_m^{\Im} = \frac{I_m^s + \sin(I_0)\psi_m^c}{2}. \quad (35)$$

Since Mars is assumed to be a non-rigid planet, a fluid core changes the prograde and retrograde terms as follows (Le Maistre 2013),

$$p'_m = p_m\left(1 + F\frac{\sigma_m}{\sigma_m - \sigma_{\mathrm{FCN}}}\right), \quad (36) \qquad r'_m = r_m\left(1 + F\frac{\sigma_m}{\sigma_m + \sigma_{\mathrm{FCN}}}\right) \quad (37)$$

where the primed parameters are the nutation amplitudes for a non-rigid planet, σ_m are the orbital rates coming from the theory of nutation, σ_{FCN} is free core nutation rate and F is the core factor. By substituting again the Equations (36) and (37) into complex terms, and replacing the real and imaginary parts using the Equations (32) to (35), the amplitudes of nutation in longitude and obliquity for a non-rigid body ($I_m^{c'}$, $I_m^{s'}$, $\psi_m^{c'}$ and $\psi_m^{s'}$) become the following (Le Maistre 2013):

$$I_m^{c'} = I_m^c\left(1 + F\frac{\sigma_m^2}{\sigma_m^2 - \sigma_{\mathrm{FCN}}^2}\right) + \sin(I_0)\psi_m^s F\frac{\sigma_m\sigma_{\mathrm{FCN}}}{\sigma_m^2 - \sigma_{\mathrm{FCN}}^2}, \quad (38) \qquad I_m^{s'} = I_m^s\left(1 + F\frac{\sigma_m^2}{\sigma_m^2 - \sigma_{\mathrm{FCN}}^2}\right) - \sin(I_0)\psi_m^c F\frac{\sigma_m\sigma_{\mathrm{FCN}}}{\sigma_m^2 - \sigma_{\mathrm{FCN}}^2}, \quad (39)$$

$$\psi_m^{c'} = \psi_m^c\left(1 + F\frac{\sigma_m^2}{\sigma_m^2 - \sigma_{\mathrm{FCN}}^2}\right) - \frac{I_m^s}{\sin(I_0)} F\frac{\sigma_m\sigma_{\mathrm{FCN}}}{\sigma_m^2 - \sigma_{\mathrm{FCN}}^2}, \quad (40) \qquad \psi_m^{s'} = \psi_m^s\left(1 + F\frac{\sigma_m^2}{\sigma_m^2 - \sigma_{\mathrm{FCN}}^2}\right) + \frac{I_m^c}{\sin(I_0)} F\frac{\sigma_m\sigma_{\mathrm{FCN}}}{\sigma_m^2 - \sigma_{\mathrm{FCN}}^2}. \quad (41)$$

With this full derivation, the connection of the core factor F and the free core nutation rate σ_{FCN} with the longitude and obliquity can be recognized.

3

Conclusion and Future Work

This chapter provides extensive conclusions based on the data presented in the Journal Article (see Chapter 2), together with possible improvements to be done in order to continue this line of research.

3.1. Conclusions

The answers to the research questions posed in Section 1.2 are provided in this section. In order to present an in-depth conclusion to the main research topic that inspired the thesis, all sub-questions are answered individually. The answer of each sub-question is found below:

1. **How much can the uncertainty of the estimated parameters from RISE and LaRa observables be reduced by using the PRIDE technique?**

   (a) *How is the correlation coefficient of the Doppler observables made at the Earth-based ground stations calculated?*

   As explained before, the observations received from radio telescopes and DSN antennas cannot be assumed to be independent. However, the constant correlation approach proposed by Filice (2019) is not yet an accurate representation of the existing correlation between the signals received at different ground stations. Time varying correlation metric between ground stations has been developed. This metric uses the distance between stations as well as the real Doppler measurements obtained by post-processing the RISE radio science experiment data. Two indicators are evaluated: (1) the comparison of noise levels and (2) the comparison of Doppler noise effects. The distance between ground stations is used as the main indicator of the weather noise correlation between signals. Ionospheric and tropospheric noises are very similar for ground stations located close to each other. Thus, the lower the distance between receiving stations, the greater the correlation associated to weather effects. On the contrary, the Doppler noise indicator is evaluated using the real Doppler measurements as well as the noise budget indicated in Chapter 2. The real Doppler measurements consist of five observations passes measured from 10 receive-only radio telescopes over the course of 2020 year. Moreover, the Doppler noise indicator takes into account that the solar plasma noise varies over time. Using the values of the modified Allan deviation at τ=60 s for each station, the correlation of this indicator is determined by analyzing the differences between the noise levels at the two stations. The greater the common noise between the two signals, the higher the correlation coefficient. These two indicators are weighted using the ratio of the tropospheric noise to the total noise as a noise budget estimation. It is important to note that this metric was developed for the purpose of the research presented in this thesis. Being such a complex problem, the published correlation models for signal post-processing are very scarce and did not provide the degree of accuracy that was required for this research. Henceforth, having a preliminary metric that varies with time and for each combination of

stations entails a significant improvement to the available signal correlation models. The proposed model has imperfections in that it uses fixed Doppler noise for each ground station before incorporating the change of solar plasma noise. Thus, using real Doppler noise data sets that vary over time for each station would improve the model, and at the same time, help to validate the metric.

(b) *How is the interplay between MOPs on the observables changed from a single-lander configuration to two-lander configuration?*

The interplay between the MOPs varies when a one-lander or a two-lander configuration is utilized. In a one-lander configuration, no differences were reported in the accuracy of the MOPs when the InSight or ExoMars observations are gathered independently. In this tracking scenario, three strong correlations are observed. First, the correlation between the core factor F and the free core nutation rate σ_{FCN} occurs as the rotational variations depend on F and σ_{FCN} a similar manner. Secondly, for the same frequency, the sine and cosine terms of the polar motion parameters are correlated with each other. Thirdly, the polar motion parameters are correlated with the spin variations relative to the same order and frequency. These strong correlations and anti-correlations are reduced significantly when combining data from two landers. The main explanation why the strong correlations are halved can be found in the optimum location of the two landers, which are opposite longitudinally to each other. Due to this, the uncertainties of the polar motion parameters are the most affected when the two missions are combined as the signatures are decreased significantly. In this specific two-lander configuration, the interplay between MOPs is completely different. In addition to the relaxation of the strong correlations observed in a one-lander configuration, the rest of the MOPs present a moderate correlation between them, which was much lower in the one-lander case.

(c) *What is the improvement of the accuracy of the MOPs by combining RISE and LaRa instrument measurements?*

The proposed covariance analysis method has the advantage of allowing simultaneous analysis of observations received from different stations (including PRIDE stations). When only DSN stations are used, the weight matrix **W** becomes a diagonal matrix containing only the observation weights. It should be noted, however, that when several receive-only stations are considered, a creative approach to the weight matrix **W** is required. Combining the two radio science experiments, a large decrease appears in the MOPs uncertainty in comparison with a single-lander configuration. The parameters that are the most affected due to the variation of network geometry are those related to polar motion. As it was stated for the previous question, the polar motion parameters are the MOPs that depend most on the longitude of the lander. Thus, there is a fast decrease in the uncertainties of these parameters. More precisely, the polar motion uncertainty is reduced on average by 96 % with respect to the one-lander configuration. The other parameters are also influenced by the de-correlation, but they have a slower decrease. The core factor F, the 4 polar motion parameters at the Chandler frequency, and the 8 spin variation parameters have been reduced on average by 87 %, 87 %, and 89 % with respect to the one-lander configuration. On the contrary, the spin nutation rate σ_{FCN} is the parameter that has the lowest decrease, it reduced only by 74 % with reference to the one-lander configuration.

The results achieved are compared quantitatively with existing literature. In the proposed model using a two-lander configuration, the uncertainties of the core factor F, the 8 spin variation parameters and the 20 polar motion parameters at the end of ExoMars mission converge towards 0.0026, 0.52 mas and 1.2 mas, respectively. In Yseboodt et al. (2004), the estimated final precision of the core factor F, the spin variation parameters, and the polar motion parameters are 0.006, 3 mas, and 2 mas, respectively. These uncertainties are relatively close to those presented. Additionally, in Peters et al. (2020), the MOPs uncertainties are also estimated using InSight and ExoMars with a two-lander configuration. Unfortunately, the set of MOPs used are slightly different and the only uncertainties that can be compared are the spin variation parameters. For the annual and semi-annual spin angles, the final uncertainties are both 8 mas, which are slightly above those reported here. These results

are based on simulations using Doppler observations from a period of time of 4 years, which is a half of that used in this work. This makes a straight comparison difficult and may explain the slight differences observed.

(d) *What is the improvement of the accuracy of the MOPs by implementing additional receive-only antennas?*

The addition of the 10 receive-only stations can bring more data and information to the covariance analysis. In particular, 71 100 observations have been simulated for these 10 antennas to investigate the future LaRa radio science experiment. This is more than 4 times the number of two-way link observations between the transponder and the DSN antennas were expected to be collected during the LaRa radio science experiment. Using the correlation coefficient metric developed in this thesis, the uncertainty of the 4 polar motion parameters at the Chandler frequency and the other 16 polar motion parameters is reduced on average by 25 % and 15 %, respectively, when compared to the simulation where only DSN antennas are used. The least affected parameters are those related to the spin variations and core properties. The accuracy improvement of the core factor F, free core nutation rate σ_{FCN}, and 8 spin variation parameters is 12 %, 10 % and 5 % with respect to the configuration composed of only two-way links.

3.2. Recommendations for Future Work

In this section, recommendations to continue and improve the work reported in this thesis are given. Several intriguing aspects that require further research have been identified and are listed below:

1. The final formal errors achieved through the covariance analysis are slightly optimistic. True errors, which are the differences between estimated and actual values, can be several times larger than formal uncertainties. Marty et al. (2009) uses a similar covariance analysis and recommend adopting a factor of 5 to scale all formal errors obtained. The following source can be use as a benchmark for orbiters (e.g. Mars Global Surveyor), and with landers, the factor adopted should be slightly smaller. However, it is important to note that the model developed contains low whiteness of the recorded data of the five observation passes from the 10 radio telescopes. This has some effects to the formal errors. Modeling a couple of noise sources and removing them during data post-processing could improve the whiteness of the data by reflecting a more realistic scenario. Also, it can be improved by fitting the Doppler residuals using a higher-order polynomial. Moreover, each observation pass contained only a few hundred of data points and this reduces the effectiveness of the modified Allan deviation metric which is highly dependent on the size of the data set. Hence, it is recommended to analyze a large data-set to evaluate the modified Allan deviations and retrieve a more accurate Doppler noise for each station.
2. The observations are weighted using the 1-σ of the Doppler noise as a function of time. The observation weights utilized for the RISE radio science experiment are real and are taken from Buccino et al. (2022). Since the ExoMars mission has not been launched yet, the total observations noise per pass for the LaRa radio science experiments has been assumed as the sum of the minimum observation noise of the RISE experiment (when the SEP is equal to 180°) plus the increment of solar plasma model with respect to the minimum solar plasma value (using the model developed by less et al. (2012)). Other noise sources are not considered in this report and thus, should be added in future works. Depending only on the solar plasma noise source, the total noise becomes exponentially large when the SEP angle is low. By summing up a large number of noise sources, the total observation noise could be reduced when the SEP angle is low. By performing these changes, the observation noise will more accurately represent the real situation. In addition to this, the observation weights used are made as a function of time but are not dependent on each Earth-based station. Due to this, the observation weights are assumed to be the same when multiple receiving stations are visible. Thus, making the weights of the observations dependent on the receiving station would improve the model developed.
3. The correlations of noise levels between ground stations are no longer assumed to be constant. The new preliminary metric developed is dependent on the SEP angle and the station pairs. However, some improvements in how the correlation coefficient is calculated are still required.

Only the distance is considered for the weather indicator, but temperature has a significant impact as well. For the noise levels indicator, the developed metric is based solely on a single value extracted from the ED045 experiment data for each station and on the change of solar plasma over the SEP angle. The model could be improved by extracting multiple Doppler noise values for each station. Other indicators, such as signal-to-noise ratio, could also be included. The signal-to-noise ratio may aid in determining how much correlation the two stations have in local noise sources, which are affected by local observation geometry as well as system properties (e.g. mechanical noise).

4. Most of the additional radio telescopes utilized in the simulation are located all over Europe. This selection of the radio telescopes has been constrained by the real Doppler data recorded during five observation passes of the RISE radio science experiment. Only four of these 10 stations are located in the other continents, except the American continent. This is a limitation of the EVN network. Further studies should be performed to understand how much the MOPs signature varies when having a radio telescope network spread all over the world.
5. The observation time passes chosen for RISE are real and the ones from LaRa were given by the Royal Observatory of Belgium. Since the ExoMars mission was initially planned to be launched in 2021, the observations were expected to start in early 2022. However, this timeline has not been accomplished. Therefore, it should be analyzed how the results change when the time gap between the two missions is larger. From the published research, the uncertainties of the MOPs should not be significantly affected, as the variations of the Mars rotational state are periodical. A delayed launch could be attributed to larger propagation errors, since the Mars orbit should be propagated for a longer period of time. Further research is required to confirm whether the conclusions are still valid.

Bibliography

Bocanegra-Bahamon, T et al. (2019). “Venus Express radio occultation observed by PRIDE”. In: Astronomy & Astrophysics 624, A59.

Buccino, D et al. (2022). “Low-SNR Doppler Data Processing for the InSight Radio Science Experiment”. In: Remote Sensing 14.8, p. 1924.

Calves, GM et al. (2021). “High spectral resolution multi-tone Spacecraft Doppler tracking software: Algorithms and implementations”. In: Publications of the Astronomical Society of Australia 38.

Dehant, V et al. (2020). “The radioscience LaRa instrument onboard ExoMars 2020 to investigate the rotation and interior of mars”. In: Planetary and Space Science 180, p. 104776.

Duev, DA et al. (2012). “Spacecraft VLBI and Doppler tracking: algorithms and implementation”. In: Astronomy & Astrophysics 541, A43.

Filice, V (2019). “Analysis of PRIDE contribution to ExoMars-LaRa experiment”. MA thesis. Rome, Italy: University of Rome ”La Sapienza”.

Folkner, WM et al. (2018). “The rotation and interior structure experiment on the InSight mission to Mars”. In: Space Science Reviews 214.5, pp. 1–16.

Iess, L et al. (2012). “Improved Doppler tracking systems for deep space navigation”. In: ISSFD.

Marty, JC et al. (2009). “Martian gravity field model and its time variations from MGS and Odyssey data”. In: Planetary and Space Science 57.3, pp. 350–363.

Pallichadath, V et al. (2020). “PRIDE: Ground-based VLBI observations for Spaceborne Probes”. In: European Planetary Science Congress, EPSC2020–647.

Peters, MJ et al. (2020). “LaRa after RISE: Expected improvement in the Mars rotation and interior models”. In: Planetary and Space Science 180, p. 104745.

Rivoldini, A et al. (2011). “Geodesy constraints on the interior structure and composition of Mars”. In: Icarus 213.2, pp. 451–472.

Yseboodt, M et al. (2004). “Uncertainties on Mars Interior Parameters Deduced from Orientation Parameters Using Different Radio-Links: Analytical Simulations”. In: Lunar and Planetary Science Conference, p. 1643.

A

Verification and Validation

This appendix chapter will focus on the verification and validation tests that have been performed in order to check the correctness and credibility of the results given. As InSight is still a fully operational mission, Appendix A.1 presents a unit test that confirms the setup of the observation times for the RISE radio science experiment and the orbit propagation is executed correctly by comparing outcomes from the Royal Observatory of Belgium. Subsequently, the creative approach utilized, the covariance analysis method, needs to be verified. The formal errors vary depending the number of ground stations and the correlation coefficient, and thus, this is examined during the LaRa radio science experiment in Appendix A.2. The signals simulated are not noise-free and the implementation of the Gaussian noise is inspected in Appendix A.3. Appendix A.4 shows two limiting cases where the final formal errors should be almost identical to each other. Lastly, an extensive application of the TUDAT toolkit has reduced the amount of verification and validation, since already includes a significant number of unit and system tests.

A.1. Preliminary Analysis

On November 2018, the NASA's InSight lander landed successfully on Mars. After the landing, a significant amount of raw data measured has been archived on the NASA's Planetary Data System[1]. Inside *RISE Tracking Data Message (TDM) Data Collection*, a text file containing the time when RISE instrument is having communication with a specific DSN antenna (Goldstone, Canberra, and Madrid ground facilities) between 2018 and 2021 years. The preciseness of the observation times helps to determine whether the environment and propagation settings and the location of the InSight lander are implemented correctly. Also, it demonstrates that the high-accuracy Mars rotation model developed in Filice (2019) is executed properly.

However, there are some parameters that are not available in NASA's Planetary Data System. Since this work is in collaboration with the Royal Observatory of Belgium, they have provided four graphs about the RISE measurements to verify the setup does not contain any software bugs. The reason why the Royal Observatory of Belgium has access to data about RISE is that they cooperate substantially with the InSight team at NASA's Jet Propulsion Laboratory. The comparison of the graphs between the ones executed with TUDAT and those provided by a member of the Royal Observatory of Belgium (Dr. Le Maistre) is presented in Figures A.1 to A.4.

[1] https://pds-geosciences.wustl.edu/missions/insight/rise.htm

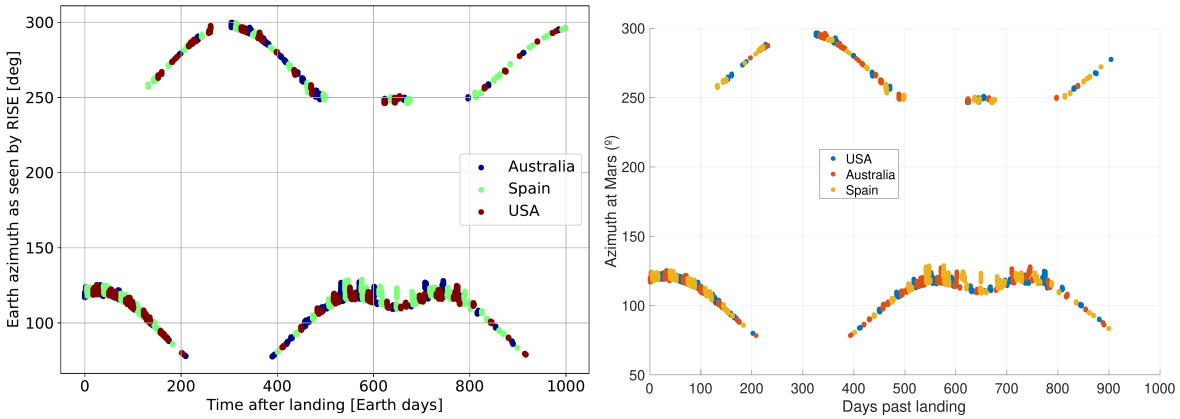

(a) Executed with TUDAT. **(b)** Extracted from Dr. Le Maistre.

Figure A.1: Earth azimuth as seen by RISE as a function of Earth days after InSight landing (27th of November 2018).

Figure A.1 testifies that the observation times selected correspond to the ones provided by the Royal Observatory of Belgium. This can be seen from the gap that occurs after 300 days approximately where the signal power is remarkably weak. This is due to the solar plasma. Additionally, the trend of the Earth azimuth as seen by RISE seems that fits the plot given by Dr. Le Maistre, and this suggests that the location and configuration of InSight lander is properly defined.

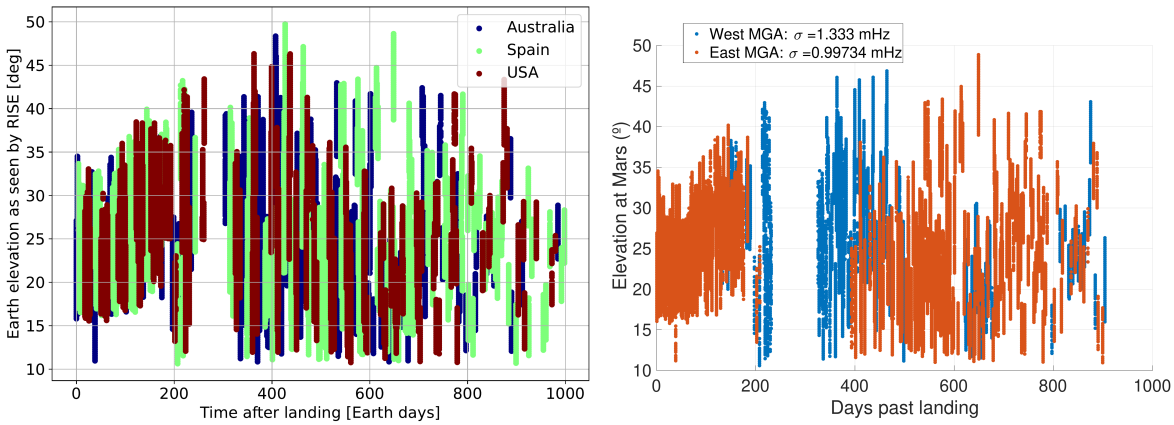

(a) Executed with TUDAT. **(b)** Extracted from Dr. Le Maistre.

Figure A.2: Earth elevation as seen by RISE as a function of Earth days after InSight landing (27th of November 2018).

Figure A.2 shows the Earth elevation angle as seen by RISE along with the mission duration. Unfortunately, the graph from the Royal Observatory of Belgium does not separate the observations by ground facilities. Nevertheless, the behavior of the plot is almost identical. The only slight difference is the observation gap shown at 300 days can be seen as somewhat smaller in the one executed with TUDAT. The reason is due to the body avoidance angle between Mars and Sun is not published and the value that has been chosen is 10°. Furthermore, it can be seen that most of the signal is between the 10° and 30°, which is the line-of-sight requirement that has been published on Peters et al. (2020).

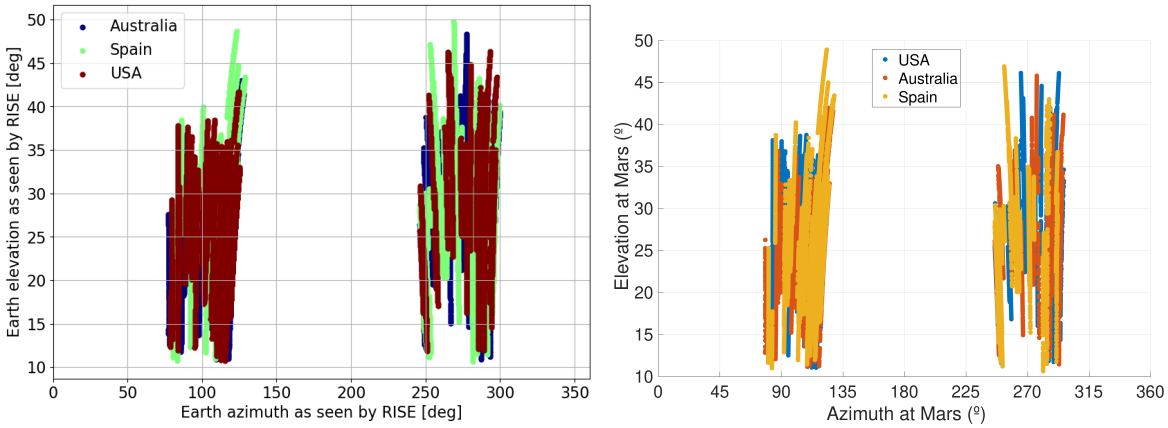

(a) Executed with TUDAT. **(b)** Extracted from Dr. Le Maistre.

Figure A.3: Earth elevation as seen by RISE as a function of Earth azimuth as seen by RISE.

Figure A.3 is the combination of the Figures A.1 and A.2, and clearly shows that the two graphs match.

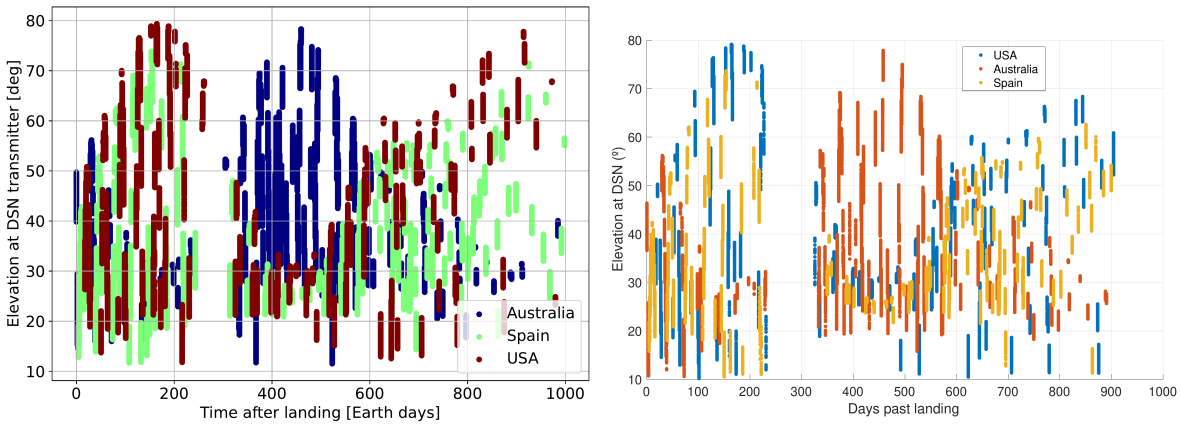

(a) Executed with TUDAT. **(b)** Extracted from Dr. Le Maistre.

Figure A.4: Elevation angle at DSN transmitter as a function of Earth days after InSight landing (27th of November 2018).

Ultimately, Figure A.4 illustrates the elevation angle when the signal is transmitted at the DSN ground stations as a function of time. Again, this plot demonstrates that the RISE observation times fit the ones extracted from the Royal Observatory of Belgium. The observation gap that occurs at 300 days match, and this certifies that the viability settings selected for the body avoidance angle are suitable. Another viability setting that here can be observed is that the DSN antenna transmits signals only when the elevation is larger than 10°. These graphs are helpful to testify the viability settings defined in Chapter 2.

A.2. Estimated Parameters as a Function of the Correlation and the Number of Stations

The simulations executed and shown in this section are utilizing only ground stations close to the European continent during the LaRa radio science experiment. When only one transmitter and the viability settings are removed, every final uncertainty of the estimated parameters should have a common trend. The behavior that should be seen is that the formal errors decrease when the correlation coefficient decreases. Similar to this, the accuracy of the estimated parameters should improve when more observations are analyzed because more information is offered to the estimator. In fact, when the observations are uncorrelated from each other, the formal errors have to decrease by a factor of $1/\sqrt{n^\circ}$ of observations. In case the observations are correlated with each other, adding more observations from other ground stations should not influence the final formal errors.

In order to testify this, the viability settings of the line-of-sight, the minimum elevation at transmitters, and the body avoidance angle are removed. Subsequently, the Gaussian noise implemented which was related to the Doppler residuals is dismissed as well. For this, only the LaRa radio science experiment is taken into consideration where a single transmitter antenna is utilized. The transmitter antenna chosen is the DSS-63 due to the vast radio telescopes around Europe that can receive the signal reflected. The nine radio telescopes utilized that can receive the signal reflected are YEBES40M, MEDICINA, EFLSBERG, WRT0, WETTZELL, ONSALA60, HARTRAO, and BADARY. The DSS-63 antenna also can receive the signal that it has transmitted. The final formal errors against the number of ground stations that receive the signal and the fixed correlation coefficient selected in the weighting matrix of the covariance analysis are shown in Figures A.5 to A.10. The range of the correlation coefficient selected is from 0 until 0.9 with a step of 0.1. The correlation coefficient of value 1 is not evaluated because the covariance matrix becomes singular and cannot be inverted due to a large condition number.

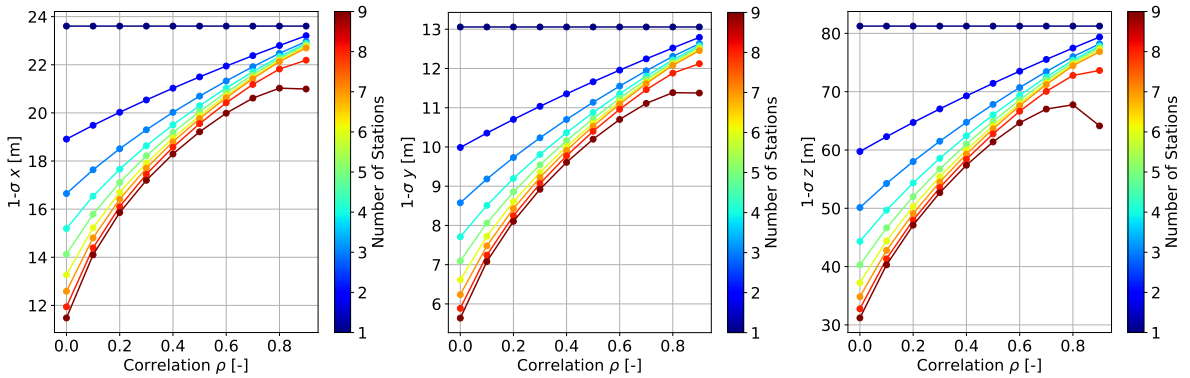

(a) $x-$coordinate. **(b)** $y-$coordinate. **(c)** $z-$coordinate.

Figure A.5: Formal errors of the initial position state evaluated at the end of the ExoMars mission as a function of the covariance coefficent and number of ground stations.

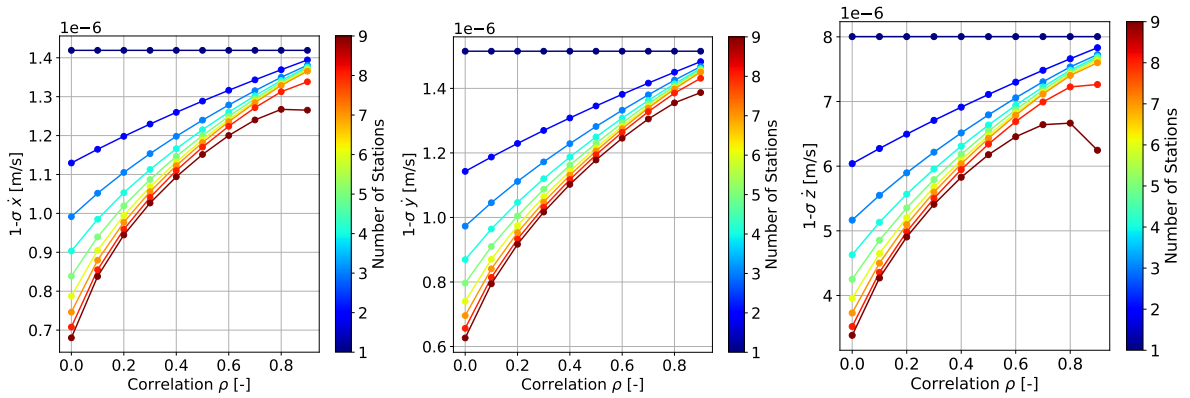

(a) Velocity along $x-$axis. **(b)** Velocity along $y-$axis. **(c)** Velocity along $z-$axis.

Figure A.6: Formal errors of the initial velocity state evaluated at the end of the ExoMars mission as a function of the covariance coefficient and number of ground stations.

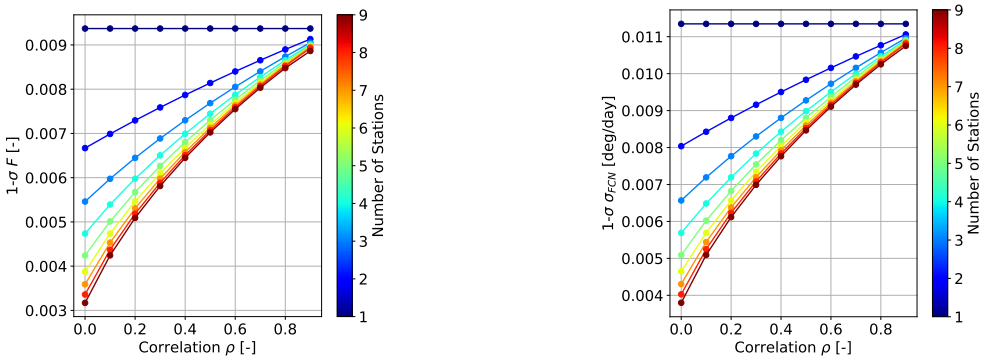

(a) Core factor F.

(b) Free core nutation rate σ_{FCN}.

Figure A.7: Formal errors of the core factor and free core nutation rate evaluated at the end of the ExoMars mission as a function of the covariance coefficient and number of ground stations.

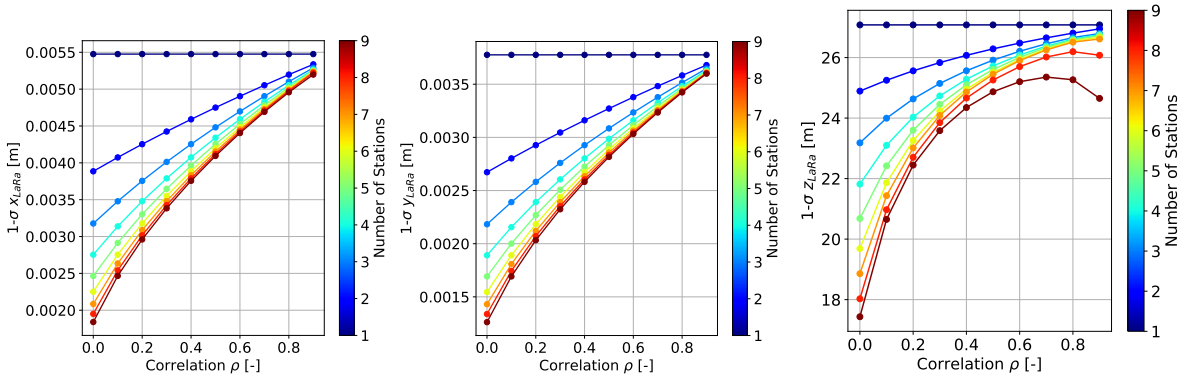

(a) $x_{\text{LaRa}}-$coordinate.

(b) $y_{\text{LaRa}}-$coordinate.

(c) $z_{\text{LaRa}}-$coordinate.

Figure A.8: Formal errors of the lander position evaluated at the end of the ExoMars mission as a function of the covariance coefficient and number of ground stations.

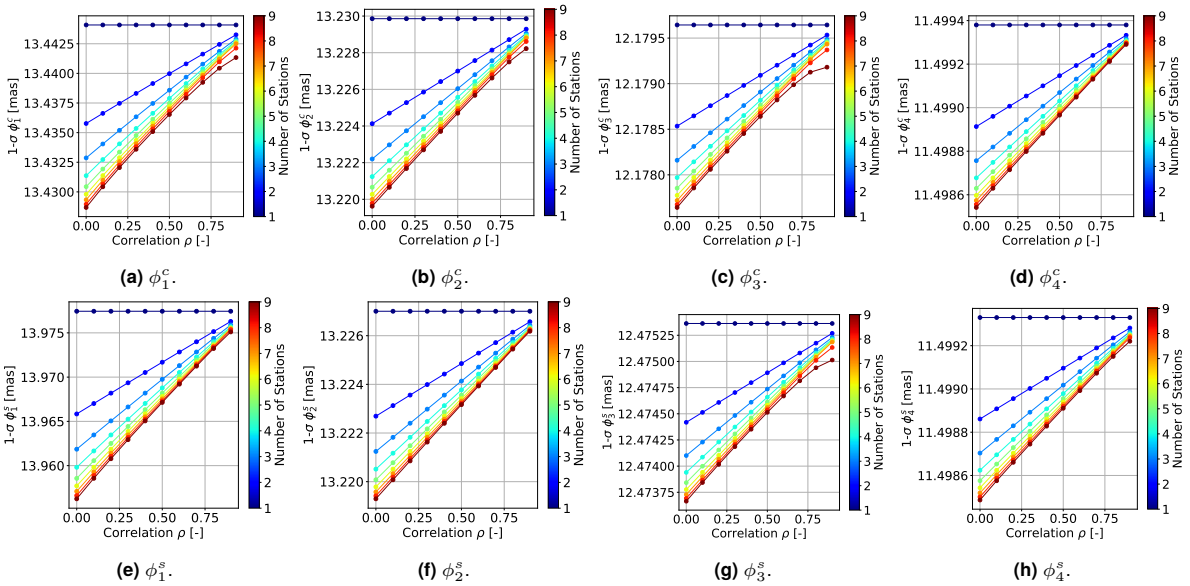

(a) ϕ_1^c.

(b) ϕ_2^c.

(c) ϕ_3^c.

(d) ϕ_4^c.

(e) ϕ_1^s.

(f) ϕ_2^s.

(g) ϕ_3^s.

(h) ϕ_4^s.

Figure A.9: Formal errors of the spin variation parameters evaluated at the end of the ExoMars mission as a function of the covariance coefficient and number of ground stations.

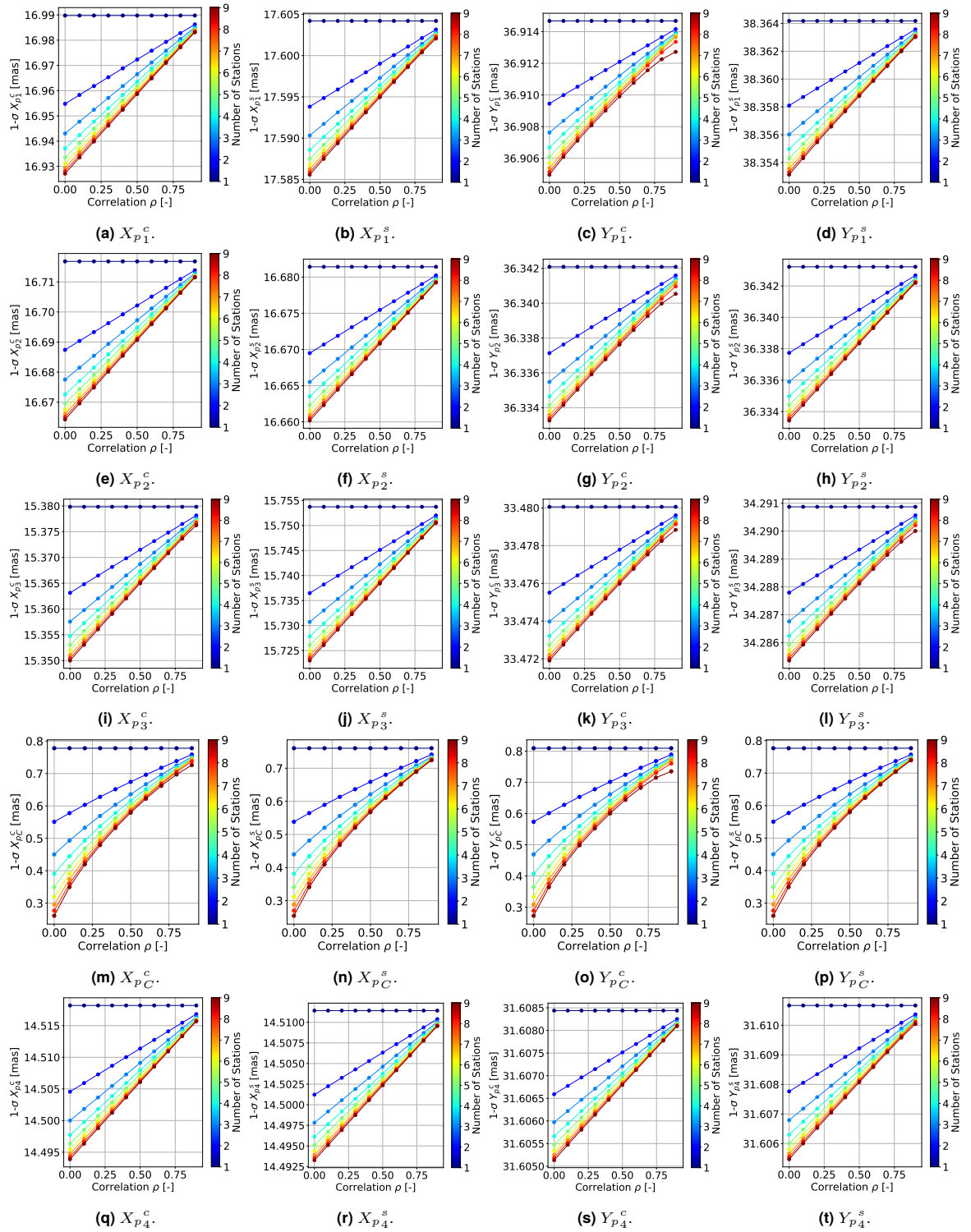

(a) $X_{p_1}^c$. **(b)** $X_{p_1}^s$. **(c)** $Y_{p_1}^c$. **(d)** $Y_{p_1}^s$.

(e) $X_{p_2}^c$. **(f)** $X_{p_2}^s$. **(g)** $Y_{p_2}^c$. **(h)** $Y_{p_2}^s$.

(i) $X_{p_3}^c$. **(j)** $X_{p_3}^s$. **(k)** $Y_{p_3}^c$. **(l)** $Y_{p_3}^s$.

(m) $X_{p_C}^c$. **(n)** $X_{p_C}^s$. **(o)** $Y_{p_C}^c$. **(p)** $Y_{p_C}^s$.

(q) $X_{p_4}^c$. **(r)** $X_{p_4}^s$. **(s)** $Y_{p_4}^c$. **(t)** $Y_{p_4}^s$.

Figure A.10: Formal errors of the polar motion parameters evaluated at the end of the ExoMars mission as a function of the covariance coefficient and number of ground stations.

These plots confirm that the behavior of the graph tends to be second-degree polynomial when the number of stations is larger than 1. This is since the formal errors decrease by a factor of $1/\sqrt{\text{n}^\circ \text{ of observations}}$ when the observations are uncorrelated with each other. Hence, if one assumes that the number of observations received by each station is the same one, the formal error when 9 stations are used should be a factor of $1/\sqrt{9}$ smaller than the one with 1 station. For instance, the

uncertainty of the core factor F at ρ=0 for 1 ground station is about 0.0094 (see Figure A.7a), and for 9 ground stations the uncertainty should tend to $0.0094/\sqrt{9} \approx 0.0031$. For the polar motion parameters, the second-degree curve is more light compared to the rest of the parameters. The reason is that the polar motions are strongly correlated with each other and with the spin variation parameters relative to the same order. On the other hand, the formal errors have to be identical when they are correlated with each other (close to ρ equal to 1) and this means that the number of ground stations is not dependent. All of this clearly shows that the setup of the covariance analysis, specifically the one of the weighting matrix, is performed correctly.

In addition to this, it is difficult to find ground stations where the number of observations that each one receive is the same for all of them. In any case, the normalized partials of the design matrix with respect to the ExoMars lander position should behave in the same way for each station as expressed in Equation (A.1) and illustrated in Figure A.11.

$$\frac{\partial H_i}{\partial \mathbf{p}} \approx \frac{\partial H_j}{\partial \mathbf{p}} \tag{A.1}$$

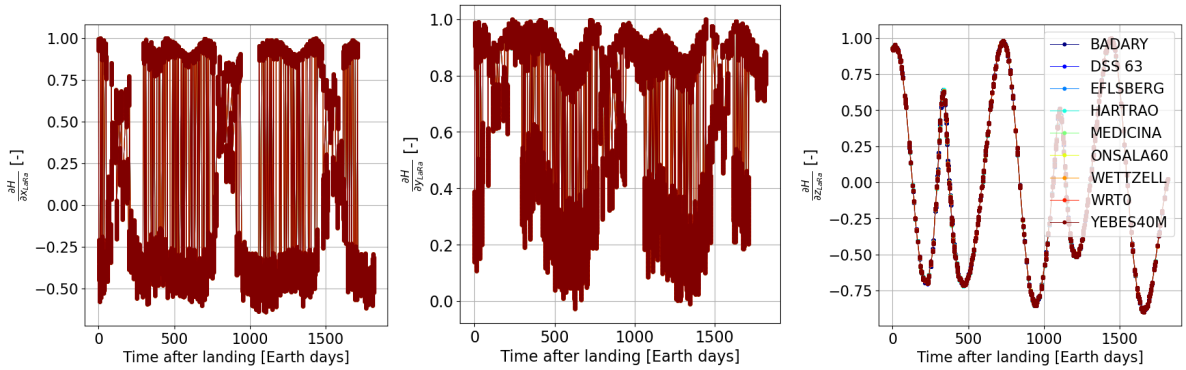

(a) $\frac{\partial H}{\partial x_{\text{LaRa}}}$ (b) $\frac{\partial H}{\partial y_{\text{LaRa}}}$ (c) $\frac{\partial H}{\partial z_{\text{LaRa}}}$

Figure A.11: Normalized partial derivatives of the design matrix with respect to the ExoMars lander position as a function of Earth days after ExoMars landing (assumed to be 3rd of January 2022).

A.3. Implementation of the Gaussian Noise

The Doppler residual generated in TUDAT is based on the observation noise. The Doppler residuals have been generated using the observation noise per pass. In this section, a verification of the RISE observations during the third day (30-11-2018) where the one standard deviation of the Doppler residual is set at 1.036633640854711E-13. With this, one verifies whether the observation noises are implemented correctly in the simulation.

For each observation, Gaussian noise is added using the variance of the observation noise per pass. This specific pass has 49 data points, and the root-mean-square error (RMSE) of all the Doppler residuals converges to the one standard deviation $(1 - \sigma)$ when the number of observations increases. This can be seen in Figure A.12 and it should work for all the rest of the passes.

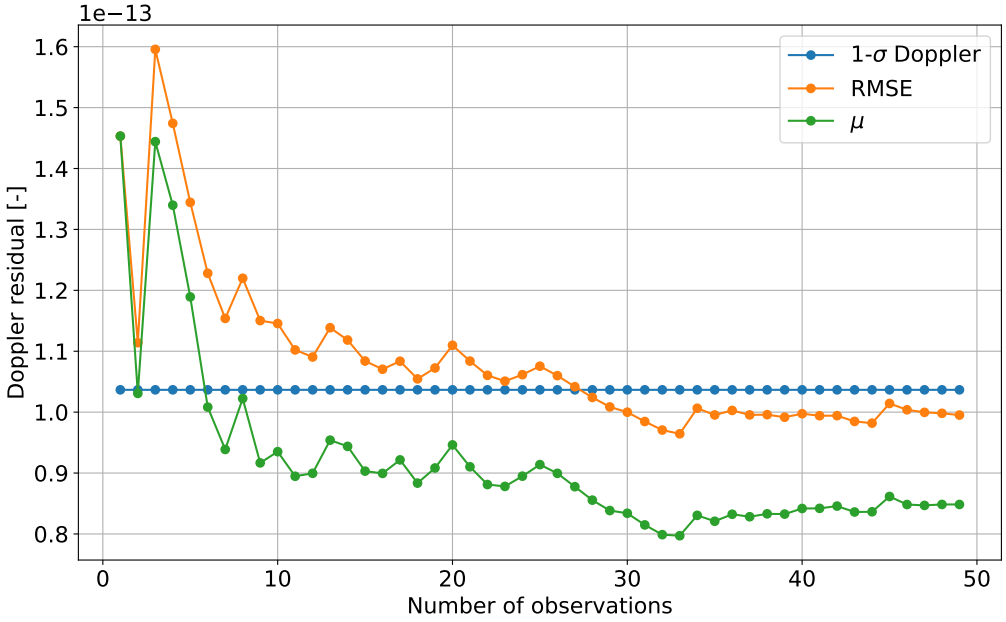

Figure A.12: $1-\sigma$, RMSE and μ of the Doppler residual.

If the pass would be larger, the RMSE should be closer to the $1-\sigma$ Doppler residual. It is important to note that as the number of observations increases, the offset between the mean and the RMSE is about $\sqrt{N}$. This is can be explained with the following equations:

$$\text{RMSE} = \sqrt{\frac{\sum_{i=1}^{N} \epsilon^2}{N}} \tag{A.2}$$

$$\mu = \frac{\sum_{i=1}^{N} \epsilon_i}{N} = \frac{\epsilon_1 + ... + \epsilon_N}{N} \cong \sqrt{\frac{(\epsilon_1 + ... + \epsilon_N)^2}{N^2}} \cong \sqrt{\frac{\epsilon_1^2 + ... + \epsilon_N^2}{N^2}} = \sqrt{\frac{\sum_{i=1}^{N} \epsilon_i^2}{N^2}} = \frac{\text{RMSE}}{\sqrt{N}} \tag{A.3}$$

A.4. Correlation Coefficient

There are two limiting cases in which the formal errors can be verified. First, as presented in Appendix A.4.1, the metric developed for computing the correlation coefficient between ground stations needs to be checked. There is not a straightforward way to inspect this, and thus, the mean correlation coefficient mentioned in Chapter 2 ($\overline{\rho}_{i,j}$=0.47) is set as a fixed correlation coefficient for all the combinations. As reported in the scientific article, when the observations are highly correlated with each other, the addition of the receive-only stations is negligible. Therefore, the final formal errors should be as well similar and the difference is investigated in Appendix A.4.2. The comparison of the results achieved is performed using the covariance analysis without estimating the initial state.

A.4.1. Cross-correlation Fixed at 0.47 *versus* Variable Cross-correlation

The formal errors of the two different simulation configurations and their dissimilarities are listed in Table A.1.

Table A.1: Comparison of formal errors.

	F [-]	σ_{FCN} [deg/day]	x_{RISE} [m]	y_{RISE} [m]	z_{RISE} [m]	x_{LaRa} [m]
ρ fixed at 0.47	2.5E-3	6.4E-3	4.4E-3	4.4E-3	9.3	3.8E-3
ρ variable	2.3E-3	6.1E-3	4.3E-3	4.4E-3	9.3	3.6E-3
Difference	5.68 %	4.38 %	0.83 %	0.43 %	0.20 %	5.35 %
	y_{LaRa} [m]	z_{LaRa} [m]	ϕ_1^c [mas]	ϕ_1^s [mas]	ϕ_2^c [mas]	ϕ_2^s [mas]
ρ fixed at 0.47	3.3E-3	5.3	0.59	0.64	0.52	0.45
ρ variable	3.1E-3	4.6	0.58	0.63	0.51	0.45
Difference	8.14 %	15.08 %	0.35 %	0.48 %	0.87 %	0.80 %
	ϕ_3^c [mas]	ϕ_3^s [mas]	ϕ_4^c [mas]	ϕ_4^s [mas]	$X_{p_1}^c$ [mas]	$X_{p_1}^s$ [mas]
ρ fixed at 0.47	0.35	0.31	0.32	0.26	1.3	1.2
ρ variable	0.35	0.3	0.31	0.26	1.3	1.1
Difference	0.66 %	1.18 %	1.85 %	1.07 %	3.82 %	3.05 %
	$Y_{p_1}^c$ [mas]	$Y_{p_1}^s$ [mas]	$X_{p_2}^c$ [mas]	$X_{p_2}^s$ [mas]	$Y_{p_2}^c$ [mas]	$Y_{p_2}^s$ [mas]
ρ fixed at 0.47	1.8	1.9	1.2	1.1	1.6	1.4
ρ variable	1.8	1.9	1.1	1.1	1.6	1.4
Difference	2.44 %	1.77 %	3.91 %	5.13 %	2.59 %	2.74 %
	$X_{p_3}^c$ [mas]	$X_{p_3}^s$ [mas]	$Y_{p_3}^c$ [mas]	$Y_{p_3}^s$ [mas]	$X_{p_C}^c$ [mas]	$X_{p_C}^s$ [mas]
ρ fixed at 0.47	1.0	1.0	1.1	1.0	0.73	0.73
ρ variable	0.95	0.96	1.1	1.0	0.66	0.66
Difference	5.48 %	5.71 %	2.89 %	3.18 %	11.14 %	10.20 %
	$Y_{p_C}^c$ [mas]	$Y_{p_C}^s$ [mas]	$X_{p_4}^c$ [mas]	$X_{p_4}^s$ [mas]	$Y_{p_4}^c$ [mas]	$Y_{p_4}^s$ [mas]
ρ fixed at 0.47	0.65	0.74	0.92	0.88	1.12	0.95
ρ variable	0.56	0.68	0.86	0.82	1.1	0.91
Difference	14.97 %	8.77 %	7.11 %	7.12 %	4.25 %	4.45 %

Table A.1 shows that the final formal errors have a small margin of error, and the average error is about 4.39 %. The two simulation scenarios cannot be considered that are the same. As explained above, the developed metric changes the correlation coefficient between ground stations constantly and it is difficult to verify whether the results simulated are correct. In any case, Table A.1 shows that the differences are smaller than the improvement that the receive-only antennas make when are implemented.

A.4.2. Cross-correlation Fixed at 0.99 *versus* not adding PRIDE Stations

The formal errors of the two different simulation configurations and their differences are listed in Table A.2.

Table A.2: Comparison of formal errors.

	F [-]	σ_{FCN} [deg/day]	x_{RISE} [m]	y_{RISE} [m]	z_{RISE} [m]	x_{LaRa} [m]
ρ fixed at 0.99	2.7E-3	7.0E-3	4.5E-3	4.5E-3	9.4	4.6E-3
Removing PRIDE stations	2.8E-3	7.0E-3	4.5E-3	4.5E-3	9.4	4.6E-3
Difference	0.86 %	0.41 %	0.10 %	0.02 %	0.02 %	0.31 %
	y_{LaRa} [m]	z_{LaRa} [m]	ϕ_1^c [mas]	ϕ_1^s [mas]	ϕ_2^c [mas]	ϕ_2^s [mas]
ρ fixed at 0.99	4.1E-3	6.3	0.59	0.64	0.53	0.46
Removing PRIDE stations	4.1E-3	6.6	0.59	0.64	0.53	0.46
Difference	0.44 %	5.09 %	0.03 %	0.08 %	0.18 %	0.13 %
	ϕ_3^c [mas]	ϕ_3^s [mas]	ϕ_4^c [mas]	ϕ_4^s [mas]	$X_{p_1}^c$ [mas]	$X_{p_1}^s$ [mas]
ρ fixed at 0.99	0.36	0.31	0.33	0.27	1.5	1.3
Removing PRIDE stations	0.36	0.32	0.33	0.27	1.5	1.3
Difference	0.07 %	0.14 %	0.25 %	0.06 %	0.16 %	0.27 %
	$Y_{p_1}^c$ [mas]	$Y_{p_1}^s$ [mas]	$X_{p_2}^c$ [mas]	$X_{p_2}^s$ [mas]	$Y_{p_2}^c$ [mas]	$Y_{p_2}^s$ [mas]
ρ fixed at 0.99	2.0	2.0	1.3	1.3	1.7	1.5
Removing PRIDE stations	2.0	2.0	1.4	1.3	1.7	1.5
Difference	0.22 %	0.22 %	0.57 %	0.46 %	0.55 %	0.62 %
	$X_{p_3}^c$ [mas]	$X_{p_3}^s$ [mas]	$Y_{p_3}^c$ [mas]	$Y_{p_3}^s$ [mas]	$X_{p_C}^c$ [mas]	$X_{p_C}^s$ [mas]
ρ fixed at 0.99	1.2	1.2	1.2	1.2	0.92	0.92
Removing PRIDE stations	1.2	1.2	1.2	1.2	0.92	0.92
Difference	0.25 %	0.26 %	0.16 %	0.27 %	0.44 %	0.71 %
	$Y_{p_C}^c$ [mas]	$Y_{p_C}^s$ [mas]	$X_{p_4}^c$ [mas]	$X_{p_4}^s$ [mas]	$Y_{p_4}^c$ [mas]	$Y_{p_4}^s$ [mas]
ρ fixed at 0.99	0.81	0.88	1.1	1.1	1.2	1.1
Removing PRIDE stations	0.82	0.91	1.1	1.1	1.2	1.1
Difference	1.17 %	2.64 %	0.30 %	0.33 %	0.18 %	0.61 %

Table A.2 confirms that having fully correlated observations or not adding receive-only stations is relatively the same. The average error between the two simulation scenarios is only about 0.51 %. The ρ value cannot be fixed at 1, because the covariance matrix becomes singular and not invertible. This affirms that the weighting matrix **W** is built properly.

B

Additional Results

In this appendix chapter, additional results that have not been presented in the journal paper (Chapter 2) are provided here. First, the graphs generated for the RISE radio science experiment shown in Appendix A.1 can be applied to LaRa radio science experiment, and this is can be seen in Appendix B.1. In addition, the resolution of the remaining estimated parameters are presented in Appendix B.2. Besides this, Appendix B.3 presents all the Doppler noise, the signal-to-noise ratio and the modified Allan deviation for the five observation passes of year 2020 from several radio telescopes.

B.1. Preliminary Analysis of LaRa Measurements

Having possible observation passes for the LaRa radio science experiment between the years 2022 and 2026, similar plots shown in Appendix A.1 can be achieved for LaRa. It is important to point out that the ExoMars mission has been delayed, and thus, the possible observation passes given by the Royal Observatory of Belgium do not correspond to the actual observation passes. By changing the observation time passes and the lander location, the Earth azimuth as seen by LaRa as a function of time can be determined as shown in Figure B.2.

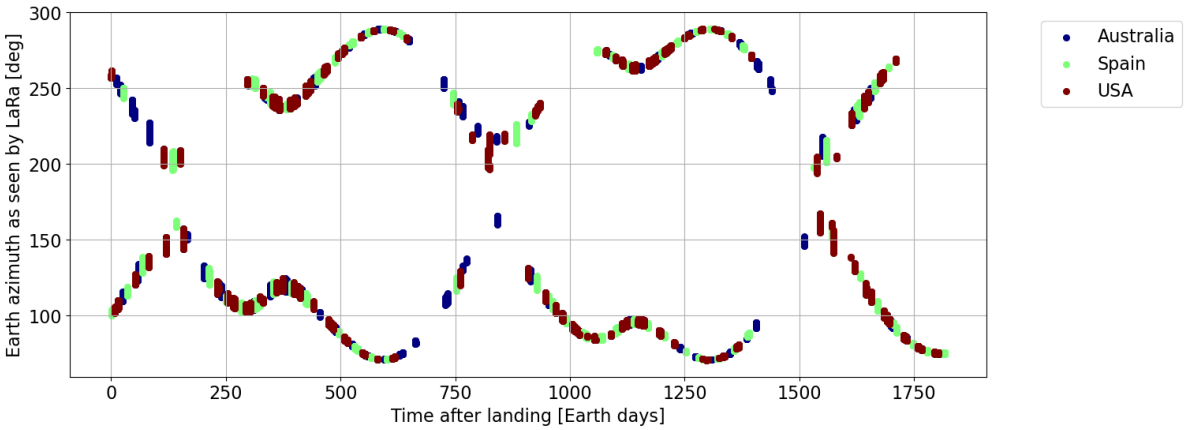

Figure B.1: Earth azimuth as seen by LaRa as a function of Earth days after ExoMars landing (assumed to be 3rd of January 2022).

Here, it can be seen that the radio science experiment lasts slightly more than the one of RISE. Nevertheless, it is important to note that LaRa instrument is planned to measure observations for 45 minutes twice a week, instead, the RISE instrument takes each day 1 hour of measurement. From this figure, the solar plasma occurs in two-time instances, around 700 and 1500 Earth days after the ExoMars landing. In the same manner, the Earth elevation as seen by LaRa can be accomplished as shown in Figure B.2.

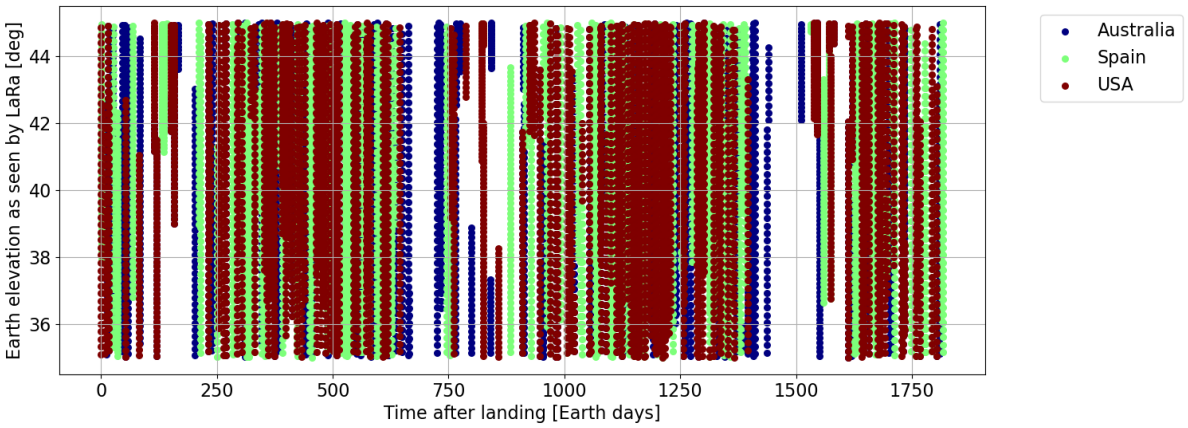

Figure B.2: Earth elevation as seen by LaRa as a function of Earth days after ExoMars landing (assumed to be 3rd of January 2022).

Figure B.2 demonstrates that the line-of-sight of the LaRa instrument is between 35° and 45°. This is one of the viability settings defined in the journal paper (see Chapter 2) and taken from Peters et al. (2020). This certifies that the setup of the environment and propagation settings have been implemented correctly. Figure B.3 is a combination of Figures B.1 and B.2.

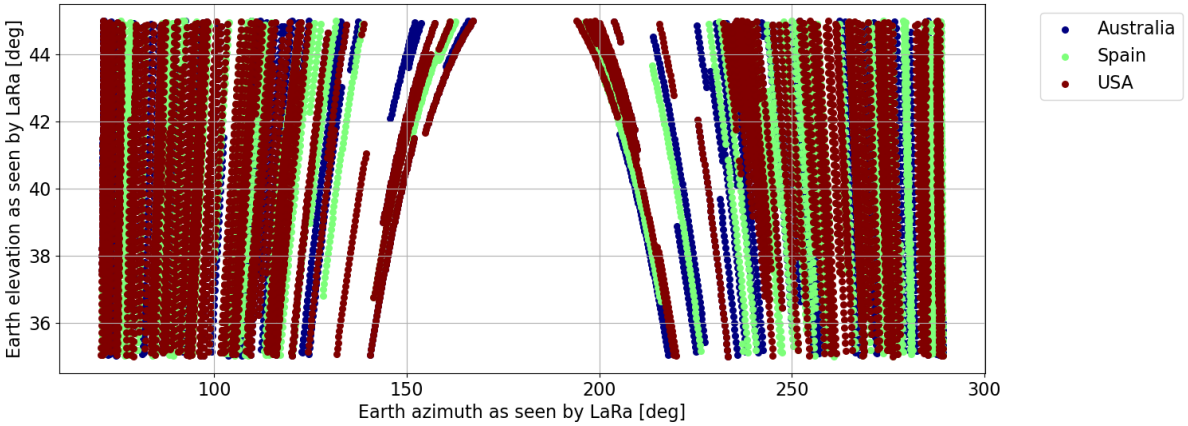

Figure B.3: Earth elevation as seen by LaRa as a function of Earth azimuth as seen by LaRa.

Compared to Figure A.3, the range of azimuth angle is larger for the LaRa instrument. Moreover, plots related to Earth-based ground stations can also be accomplished. The elevation angles at which the DSN antennas transmit the signal are presented in Figure B.4.

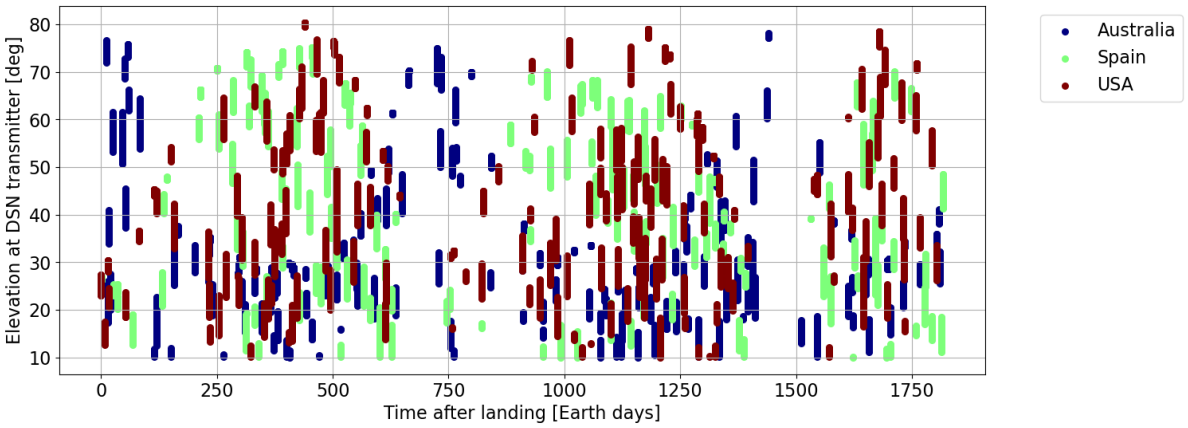

Figure B.4: Elevation angle at DSN transmitter as a function of Earth days after ExoMars landing (assumed to be 3rd of January 2022).

The elevation angles are mostly between 10° and 80°, and here, it can be seen that the minimum elevation angle at which the DSN antenna can transmit is 10°. Subsequently, the same plot can be performed when the signal is received by the Earth-based ground stations. Since the simulations utilize radio telescopes for the LaRa radio science experiments, the DSN antennas are not the only ground stations that receive the signal reflected by LaRa. The elevation angle at which the signal is received by the ground stations is shown in Figure B.5.

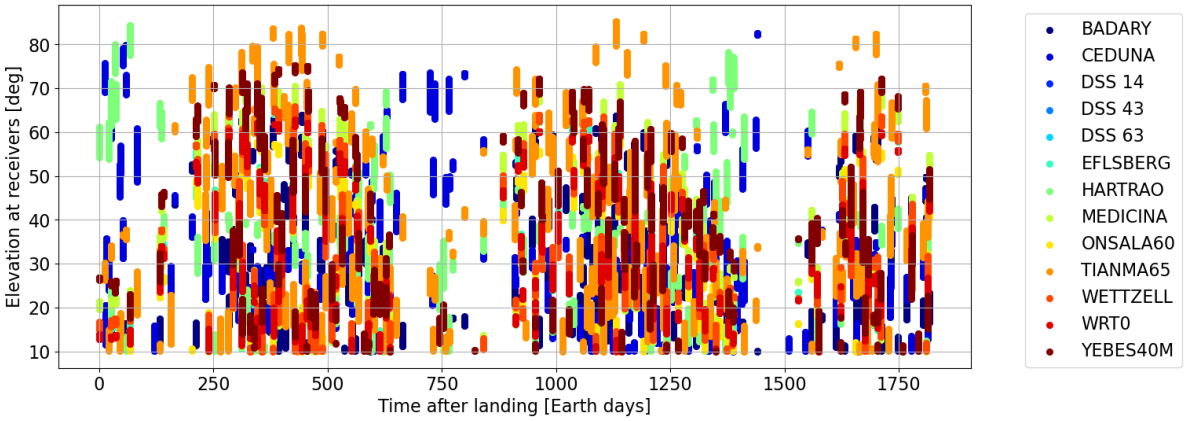

Figure B.5: Elevation angle at the receiving antennas as a function of Earth days after ExoMars landing (assumed to be 3rd of January 2022).

From Figure B.5 is difficult to interpret when each radio telescopes can receive the signal reflected by LaRa. Hence, a scatter plot to distinguish the observation occurrences from all the Earth-based ground stations. This is presented in Figure B.6.

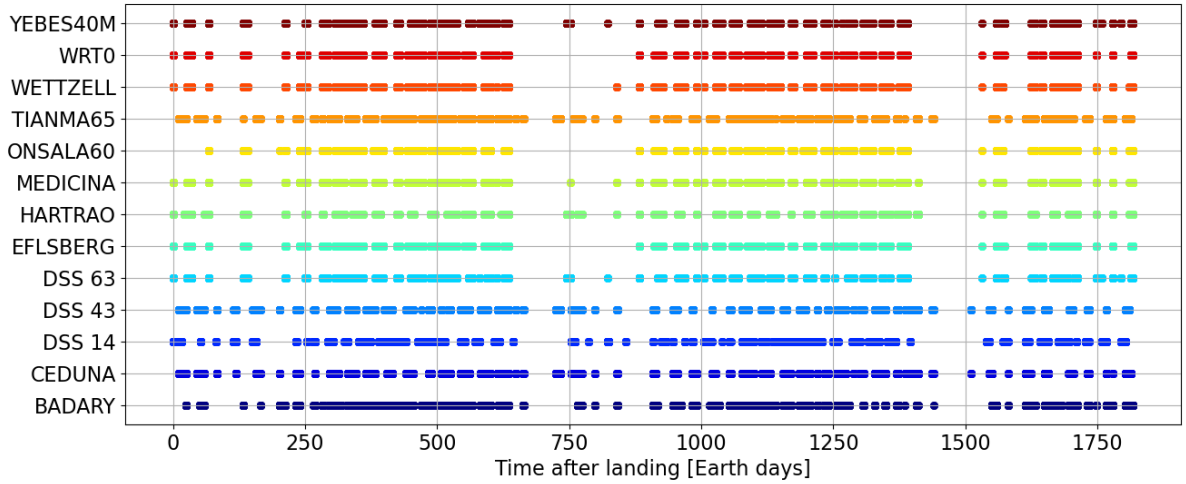

Figure B.6: Time instances when the radio signal reflected is received by the receivers (assumed to be 3rd of January 2022).

Furthermore, the number of observations measured by each Earth-based ground station is presented in a horizontal histogram as seen in Figure B.7.

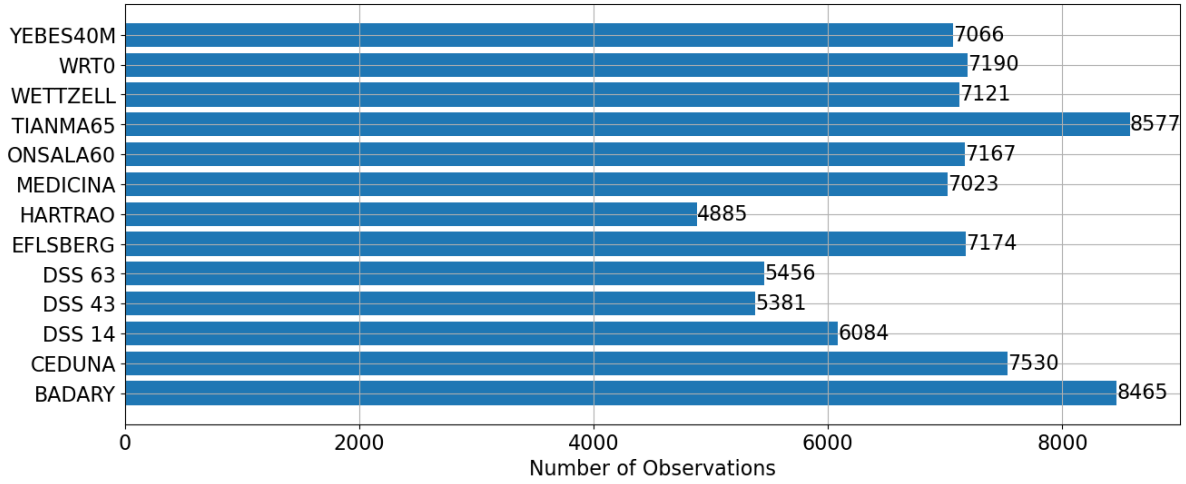

Figure B.7: Total number of observations per receiving antenna.

Most radio telescopes detect more observations than the DSN stations. This is because the radio telescopes can receive signals that are transmitted by multiple DSN antennas. Most of the radio telescopes are around Europe and they receive the signal transmitted by the DSN facilities of Madrid and Canberra. The signal from Canberra is detected from radio telescopes from Europe due to the rotation of Earth. Then, the DSN antennas are designated to receive the signal that the same stations have transmitted, and thus, the number of observations is lower compared to the radio telescopes.

B.2. Resolution of the Estimated Parameters

The resolution of the MOPs has been presented in Chapter 2. The evolution of the standard deviation of the remaining uncertainties as a function of time is shown in Figure B.8.

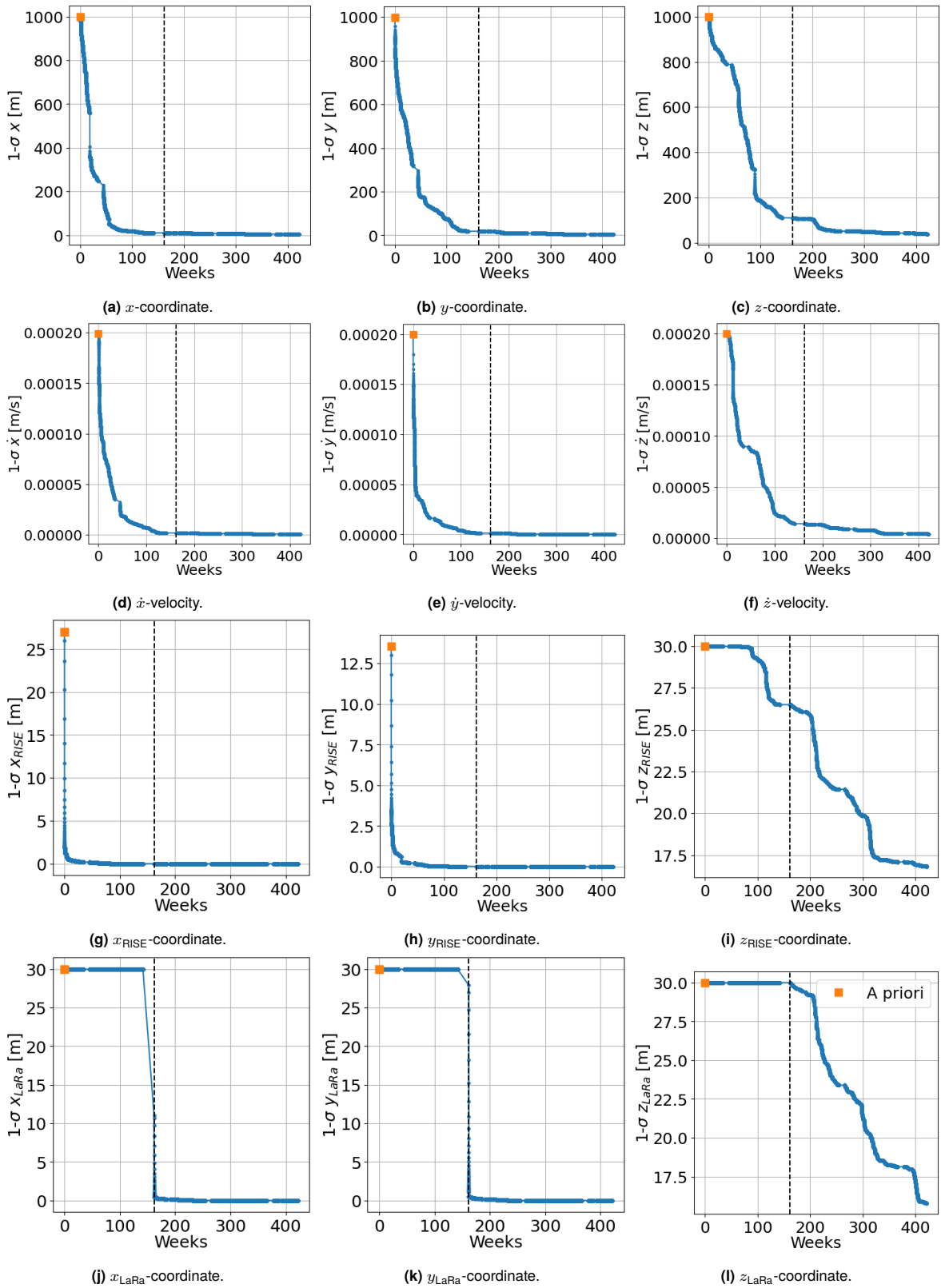

(a) x-coordinate. **(b)** y-coordinate. **(c)** z-coordinate.

(d) $\dot{x}$-velocity. **(e)** $\dot{y}$-velocity. **(f)** $\dot{z}$-velocity.

(g) x_{RISE}-coordinate. **(h)** y_{RISE}-coordinate. **(i)** z_{RISE}-coordinate.

(j) x_{LaRa}-coordinate. **(k)** y_{LaRa}-coordinate. **(l)** z_{LaRa}-coordinate.

Figure B.8: Evolution of the standard deviation of the uncertainties with respect to time. The reference time is set on the day when InSight lander arrived on the Martian surface. The black dashed line separates the RISE and LaRa radio science experiments.

The initial state behaves very similarly to the MOPs, but the uncertainties of the lander positions vary differently from the rest. During the RISE radio science experiment, it can be seen that the uncertainty

of the LaRa lander position is equal to the a priori value as the LaRa observations are not gathered until week 160.

The formal errors at the end of RISE and LaRa missions are listed for all estimated parameters, including for the MOPs, in Table B.1.

Table B.1: The standard deviation of the uncertainties of the estimated parameters.

	x [m]	y [m]	z [m]	$\dot{x}$ [m/s]	$\dot{y}$ [m/s]	$\dot{z}$ [m/s]
End of RISE	10.55	18.74	109.88	1.76E-6	1.43E-6	1.41E-5
End of LaRa	5.10	4.87	37.75	6.83E-7	3.68E-7	3.96E-6
	F [-]	σ_{FCN} [deg/day]	x_{RISE} [m]	y_{RISE} [m]	z_{RISE} [m]	x_{LaRa} [m]
End of RISE	2.09E-2	2.62E-2	1.11E-2	1.12E-2	26.5	30
End of LaRa	2.63E-3	6.8E-3	4.41E-3	4.47E-3	16.81	3.73E-3
	y_{LaRa} [m]	z_{LaRa} [m]	ϕ_1^c [mas]	ϕ_1^s [mas]	ϕ_2^c [mas]	ϕ_2^s [mas]
End of RISE	30	30	4.162	4.065	4.193	4.174
End of LaRa	3.40E-3	15.79	0.835	0.798	0.6	0.565
	ϕ_3^c [mas]	ϕ_3^s [mas]	ϕ_4^c [mas]	ϕ_4^s [mas]	${X_{p_1}}^c$ [mas]	${X_{p_1}}^s$ [mas]
End of RISE	3.915	3.944	3.895	3.865	35.069	34.758
End of LaRa	0.397	0.334	0.349	0.295	1.349	1.295
	${Y_{p_1}}^c$ [mas]	${Y_{p_1}}^s$ [mas]	${X_{p_2}}^c$ [mas]	${X_{p_2}}^s$ [mas]	${Y_{p_2}}^c$ [mas]	${Y_{p_2}}^s$ [mas]
End of RISE	35.84	35.521	35.118	35.014	35.766	35.862
End of LaRa	2.07	2.266	1.373	1.109	2.04	1.587
	${X_{p_3}}^c$ [mas]	${X_{p_3}}^s$ [mas]	${Y_{p_3}}^c$ [mas]	${Y_{p_3}}^s$ [mas]	${X_{p_C}}^c$ [mas]	${X_{p_C}}^s$ [mas]
End of RISE	34.484	34.72	35.199	35.413	8.87	8.612
End of LaRa	0.978	0.987	1.164	1.096	0.701	0.69
	${Y_{p_C}}^c$ [mas]	${Y_{p_C}}^s$ [mas]	${X_{p_4}}^c$ [mas]	${X_{p_4}}^s$ [mas]	${Y_{p_4}}^c$ [mas]	${Y_{p_4}}^s$ [mas]
End of RISE	5.063	6.039	34.106	34.224	34.867	34.937
End of LaRa	0.696	0.722	0.91	0.854	1.186	1.048

Lastly, the final formal errors of the 12 remaining estimated parameters with the two other limiting cases are illustrated in Figure B.9.

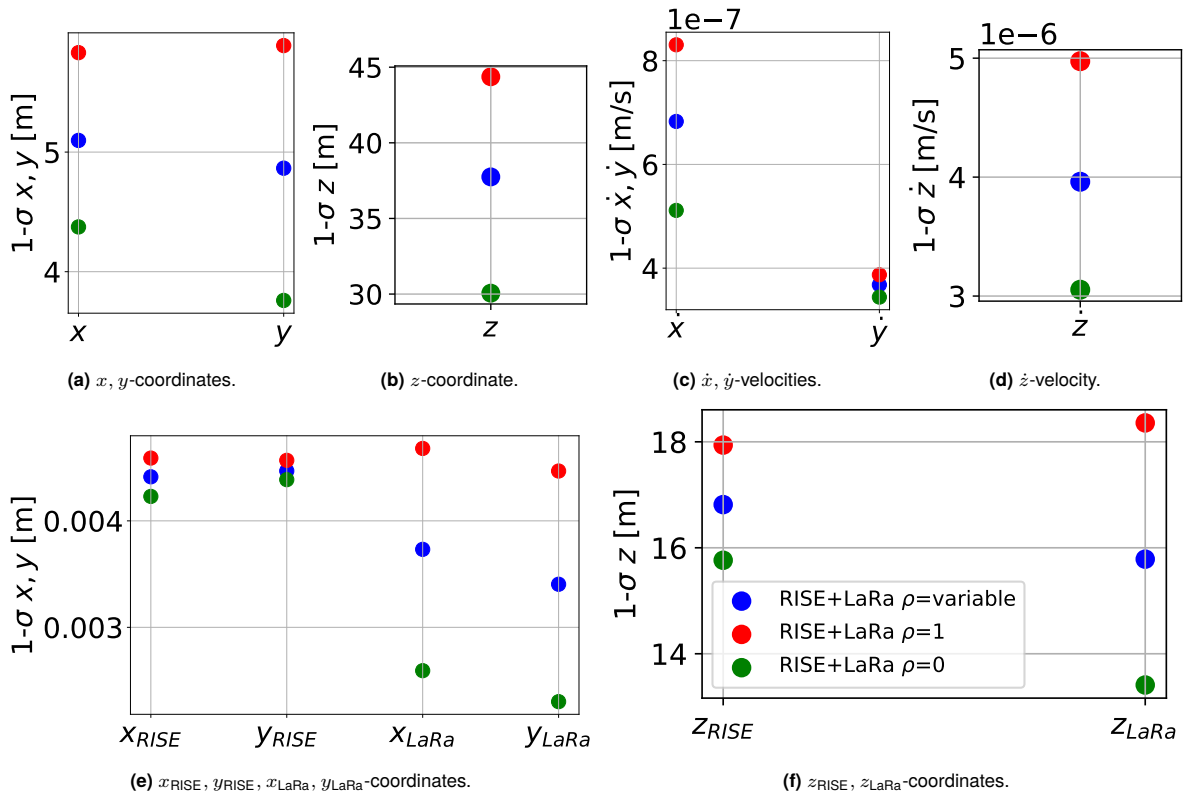

(a) x, y-coordinates. **(b)** z-coordinate. **(c)** $\dot{x}, \dot{y}$-velocities. **(d)** $\dot{z}$-velocity.

(e) $x_{\text{RISE}}, y_{\text{RISE}}, x_{\text{LaRa}}, y_{\text{LaRa}}$-coordinates. **(f)** $z_{\text{RISE}}, z_{\text{LaRa}}$-coordinates.

Figure B.9: Final formal errors of the estimated parameters obtained from different sets of configurations.

B.3. ED045 Experiment

The Joint Institute of VLBI ERIC has shared with TU Delft five observation passes of RISE radio science experiment during 2020 year. This specific radio science experiment is denoted ED045 experiment. These observation passes have been observed by radio telescopes owned by JIVE. The measurements took place on the following dates:

- 22nd of February 2020
- 29th of May 2020
- 30th of May 2020
- 21st of October 2020
- 22nd of October 2020

These measurements have been utilized for the determination of the correlation coefficient between the ground stations during the LaRa radio science experiment. Since the simulation includes radio telescopes only for the LaRa radio science experiment, actual and real measurements have been carried out in preparation for the LaRa operations. In fact, the minimum Allan deviation at τ=60 s of each station normalized with respect to the topocentric frequency is the value utilized for the computation of the correlation coefficient. The observations have been post-processed and the algorithms used are explained on Calves et al. (2021). The algorithms utilized by JIVE are meant to reduce and remove systematic noises. This is done by fitting the Doppler residuals.

However, the signal still contains a few outliers in some data products, such as the signal-to-noise ratio and Doppler noise. Hence, additional filtering has been processed to remove the irregularities. Also, some observations had a drop in the signal-to-noise ratio and these measurements have been cropped. The drops are caused when the lander can be seen by the receiver when the elevation angle is lower than 10° or when there is an interference. Here, the signal power is reduced significantly, and thus, the noise dominates.

The JIVE's receive-only antennas are located in Badary, Ceduna, Effelsberg, Hartrao, Irbene, Medicina, Onsala, Tian Ma, Dwingeloo, Wettzell, and Yebes. Three plots are presented for each observation pass that is received by radio telescopes. The plots are: (1) the Doppler noise as a function of time, (2) the signal-to-noise ratio as a function of time, and (3) the modified Allan deviation as a function of time integration τ. The modified Allan deviation graph shows whether the post-fitting algorithms have removed the noises from the measurements. If the observation contains only propagation and instrumental noises, which are random noises, the modified Allan deviation should have a slope of -0.5. Since most of the observations still contain systematic noises, the slope is not -0.5. This means that a higher order polynomial is needed for fitting the Doppler residuals more precisely. Some of the Doppler noises have a periodic behavior, and therefore, the minimum Allan deviation has a high value and the trend is quite off from the one of white noise. This is one of the reasons why Irbene station has been removed from the simulations. Then, the number of data points of each observation pass are relatively low for computing a suitable modified Allan deviation. This is indicated as well with the large error bars of the modified Allan deviation.

In addition to this, it is important to note that the signal-to-noise ratio is dependent of the diameter antenna, weather as well as the elevation angle at which the signal is received. These three factors make variations on the signal-to-noise ratio.

The three graphs for each observation pass are illustrated below:

B.3.1. BADARY

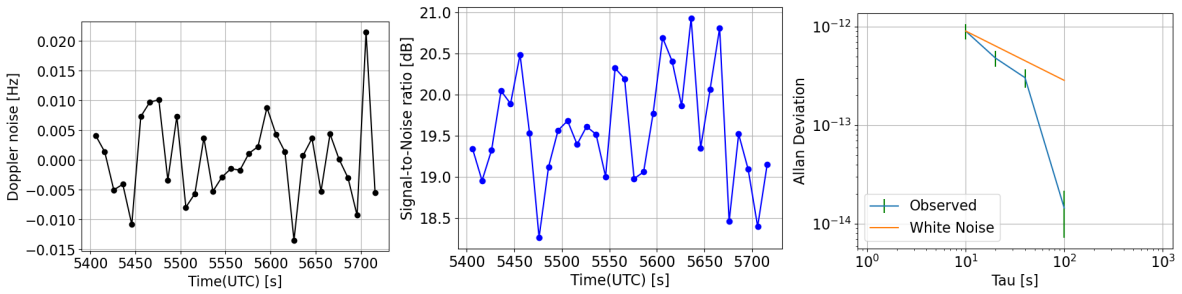

(a) Doppler noise as function of time. **(b)** Signal-to-noise ratio as function of time. **(c)** Modified Allan deviation.

Figure B.10: Real measurements observed from Badary station at 01:30:06 UTC on the 22nd of February 2020.

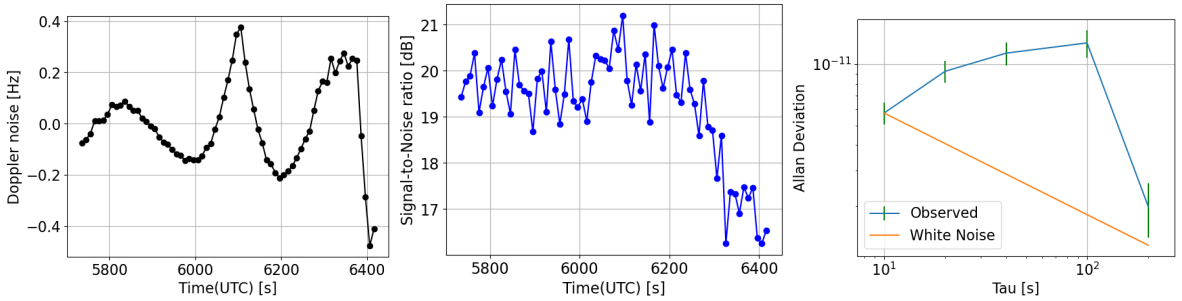

(a) Doppler noise as function of time. **(b)** Signal-to-noise ratio as function of time. **(c)** Modified Allan deviation.

Figure B.11: Real measurements observed from Badary station at 01:35:36 UTC on the 22nd of February 2020.

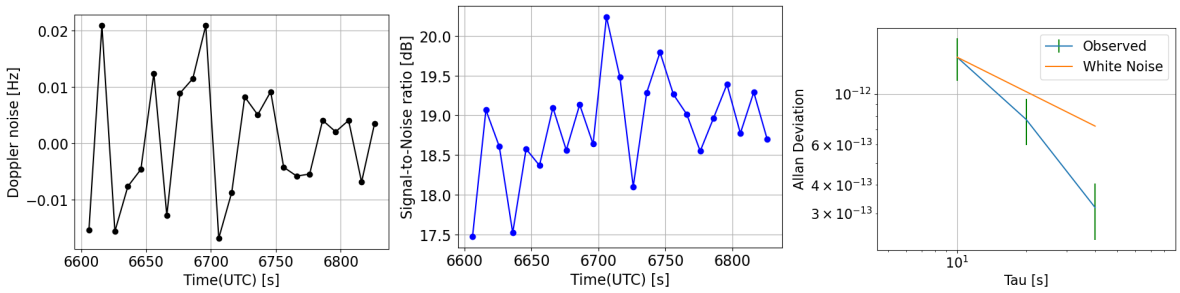

(a) Doppler noise as function of time. **(b)** Signal-to-noise ratio as function of time. **(c)** Modified Allan deviation.

Figure B.12: Real measurements observed from Badary station at 01:50:06 UTC on the 22nd of February 2020.

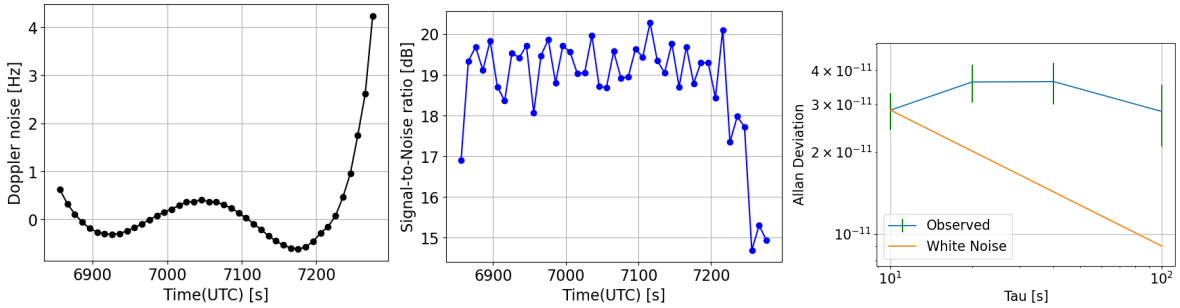

(a) Doppler noise as function of time. **(b)** Signal-to-noise ratio as function of time. **(c)** Modified Allan deviation.

Figure B.13: Real measurements observed from Badary station at 01:54:16 UTC on the 22nd of February 2020.

B.3.2. CEDUNA

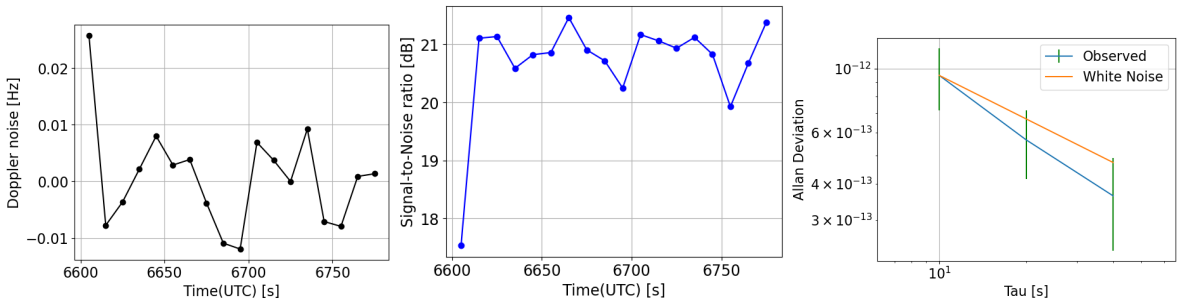

(a) Doppler noise as function of time. **(b)** Signal-to-noise ratio as function of time. **(c)** Modified Allan deviation.

Figure B.14: Real measurements observed from Ceduna station at 01:50:05 UTC on the 22nd of February 2020.

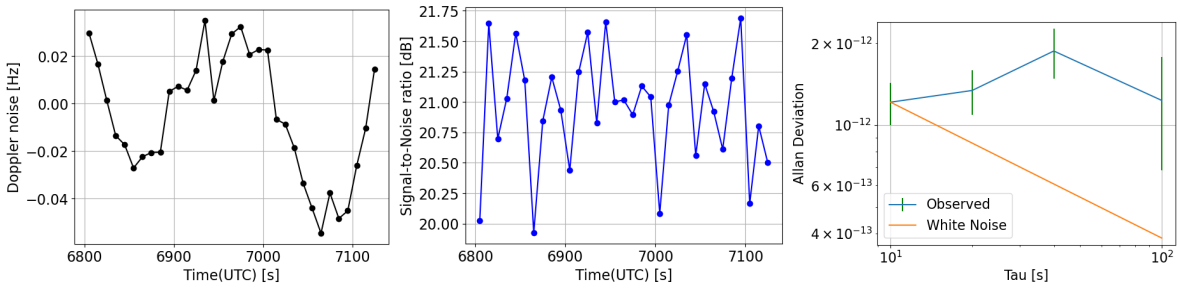

(a) Doppler noise as function of time. **(b)** Signal-to-noise ratio as function of time. **(c)** Modified Allan deviation.

Figure B.15: Real measurements observed from Ceduna station at 01:53:25 UTC on the 22nd of February 2020.

B.3.3. EFLSBERG

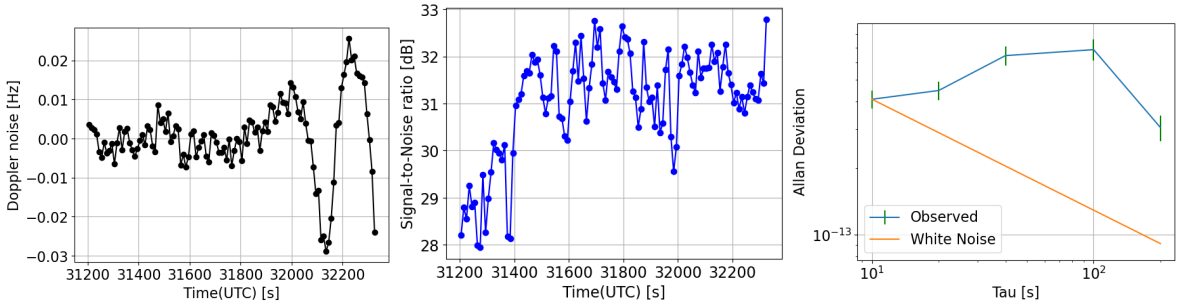

(a) Doppler noise as function of time. **(b)** Signal-to-noise ratio as function of time. **(c)** Modified Allan deviation.

Figure B.16: Real measurements observed from Effelsberg station at 08:40:05 UTC on the 29th of May 2020.

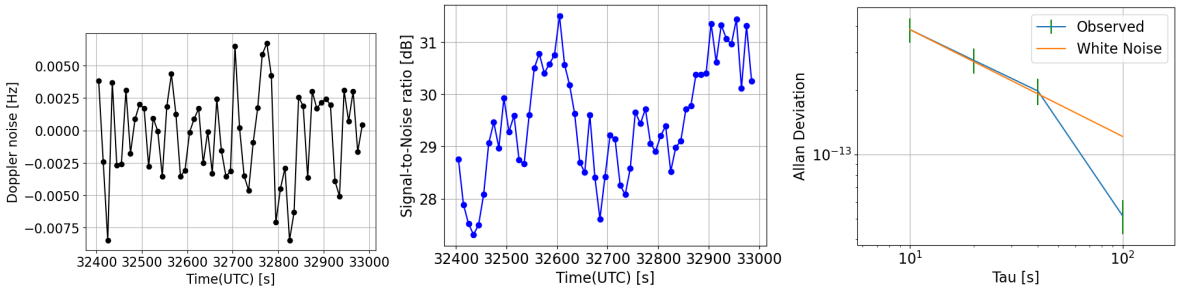

(a) Doppler noise as function of time. **(b)** Signal-to-noise ratio as function of time. **(c)** Modified Allan deviation.

Figure B.17: Real measurements observed from Effelsberg station at 09:00:05 UTC on the 29th of May 2020.

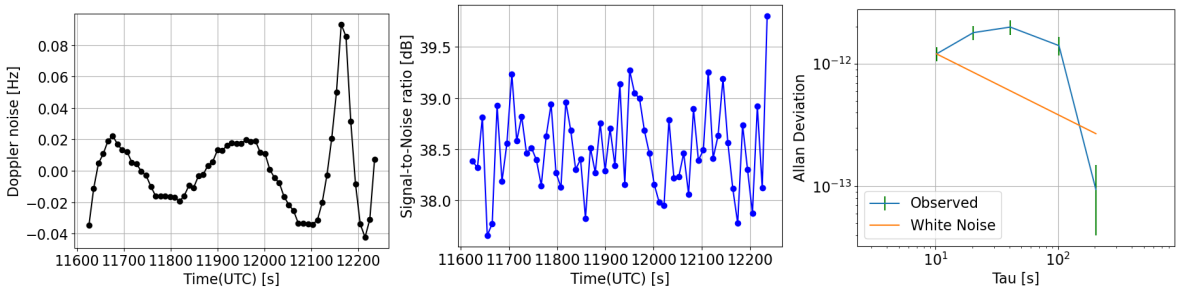

(a) Doppler noise as function of time. **(b)** Signal-to-noise ratio as function of time. **(c)** Modified Allan deviation.

Figure B.18: Real measurements observed from Effelsberg station at 03:13:45 UTC on the 21st of October 2020.

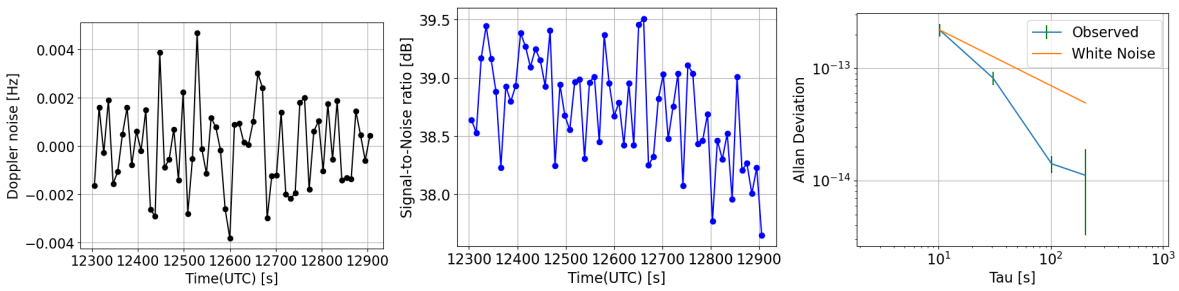

(a) Doppler noise as function of time. **(b)** Signal-to-noise ratio as function of time. **(c)** Modified Allan deviation.

Figure B.19: Real measurements observed from Effelsberg station at 03:25:05 UTC on the 21st of October 2020.

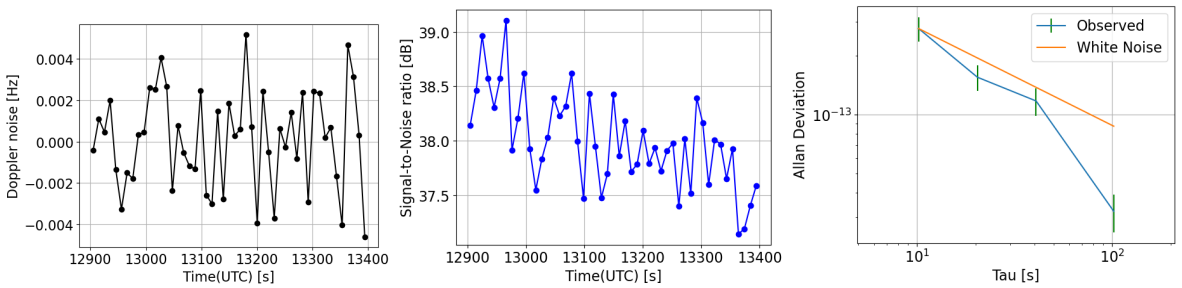

(a) Doppler noise as function of time. **(b)** Signal-to-noise ratio as function of time. **(c)** Modified Allan deviation.

Figure B.20: Real measurements observed from Effelsberg station at 03:35:05 UTC on the 21st of October 2020.

B.3.4. HARTRAO

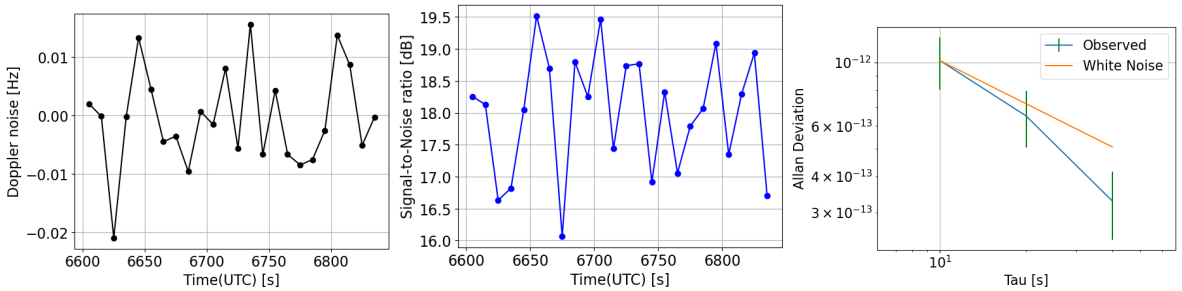

(a) Doppler noise as function of time. **(b)** Signal-to-noise ratio as function of time. **(c)** Modified Allan deviation.

Figure B.21: Real measurements observed from Hartrao station at 01:50:05 UTC on the 22nd of February 2020.

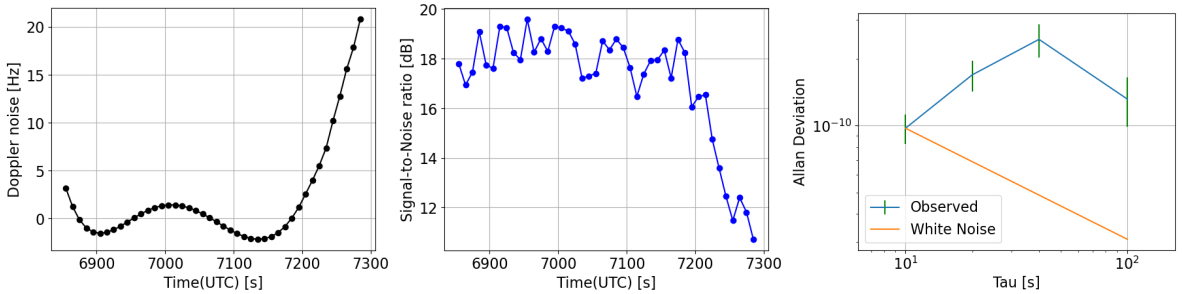

(a) Doppler noise as function of time. **(b)** Signal-to-noise ratio as function of time. **(c)** Modified Allan deviation.

Figure B.22: Real measurements observed from Hartrao station at 01:54:15 UTC on the 22nd of February 2020.

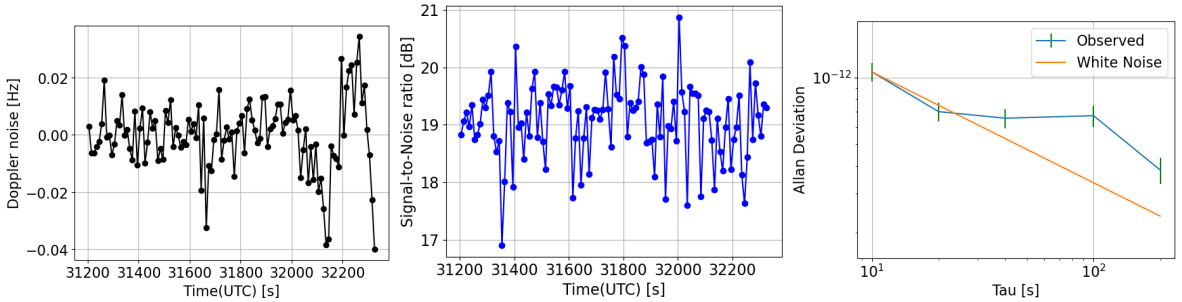

(a) Doppler noise as function of time. **(b)** Signal-to-noise ratio as function of time. **(c)** Modified Allan deviation.

Figure B.23: Real measurements observed from Hartrao station at 08:40:05 UTC on the 29th of May 2020.

B.3.5. IRBENE

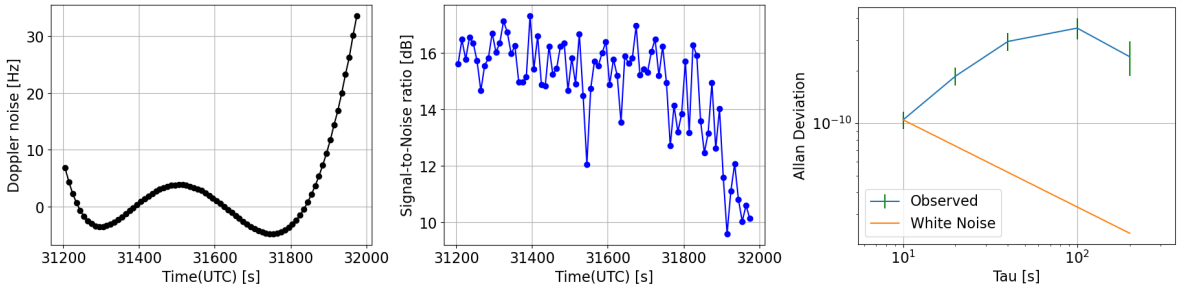

(a) Doppler noise as function of time. **(b)** Signal-to-noise ratio as function of time. **(c)** Modified Allan deviation.

Figure B.24: Real measurements observed from Irbene station at 08:40:05 UTC on the 29th of May 2020.

B.3.6. MEDICINA

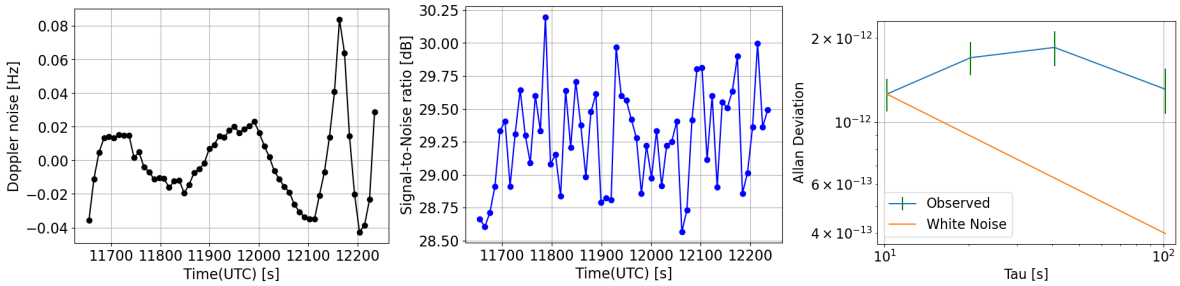

(a) Doppler noise as function of time. **(b)** Signal-to-noise ratio as function of time. **(c)** Modified Allan deviation.

Figure B.25: Real measurements observed from Medicina station at 03:14:15 UTC on the 30th of May 2020.

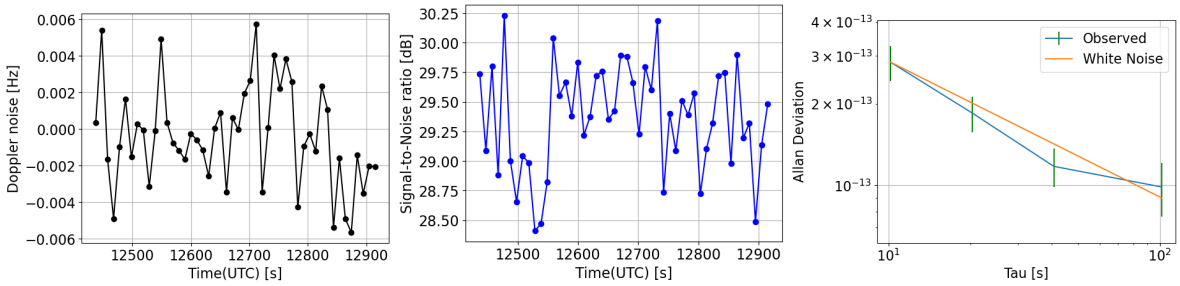

(a) Doppler noise as function of time. **(b)** Signal-to-noise ratio as function of time. **(c)** Modified Allan deviation.

Figure B.26: Real measurements observed from Medicina station at 03:25:05 UTC on the 30th of May 2020.

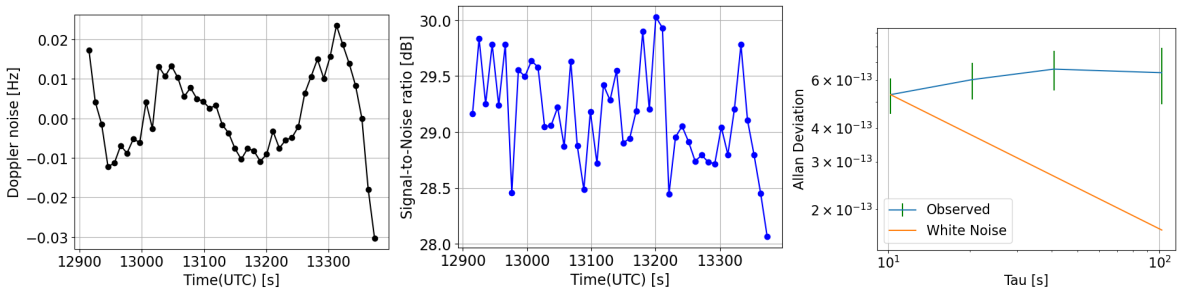

(a) Doppler noise as function of time. **(b)** Signal-to-noise ratio as function of time. **(c)** Modified Allan deviation.

Figure B.27: Real measurements observed from Medicina station at 03:35:15 UTC on the 30th of May 2020.

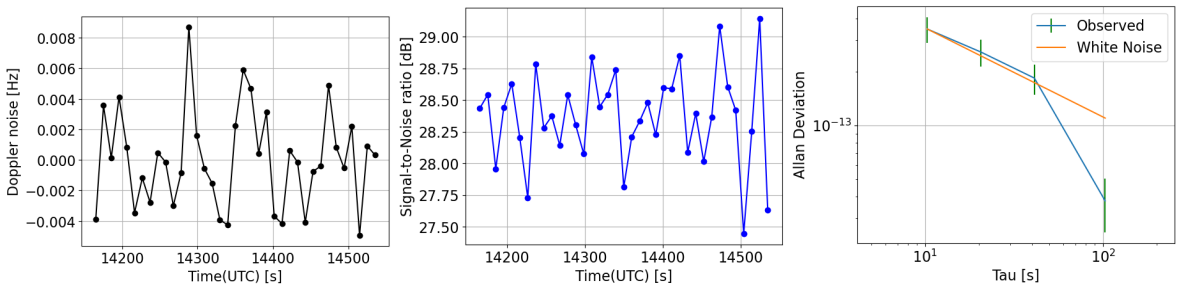

(a) Doppler noise as function of time. **(b)** Signal-to-noise ratio as function of time. **(c)** Modified Allan deviation.

Figure B.28: Real measurements observed from Medicina station at 03:56:05 UTC on the 22nd of October 2020.

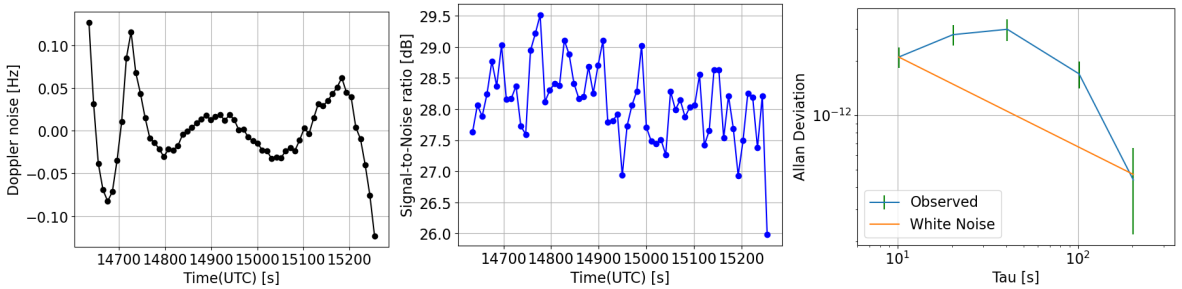

(a) Doppler noise as function of time. **(b)** Signal-to-noise ratio as function of time. **(c)** Modified Allan deviation.

Figure B.29: Real measurements observed from Medicina station at 04:03:55 UTC on the 22nd of October 2020.

B.3.7. ONSALA60

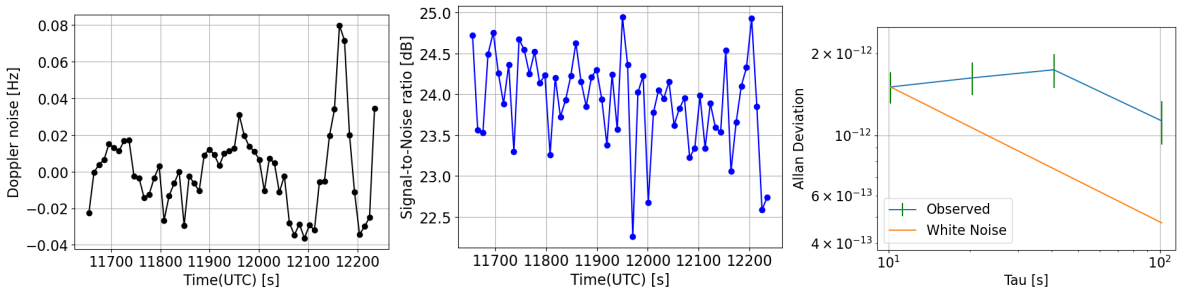

(a) Doppler noise as function of time. **(b)** Signal-to-noise ratio as function of time. **(c)** Modified Allan deviation.

Figure B.30: Real measurements observed from Onsala station at 03:14:15 UTC on the 21st of October 2020.

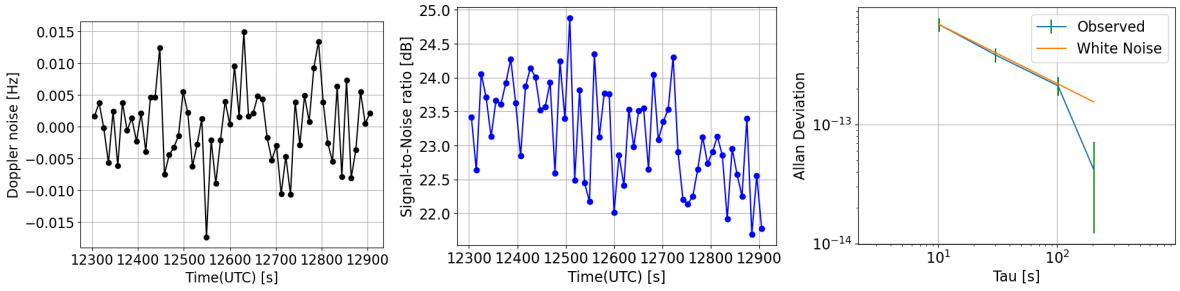

(a) Doppler noise as function of time. **(b)** Signal-to-noise ratio as function of time. **(c)** Modified Allan deviation.

Figure B.31: Real measurements observed from Onsala station at 03:25:05 UTC on the 21st of October 2020.

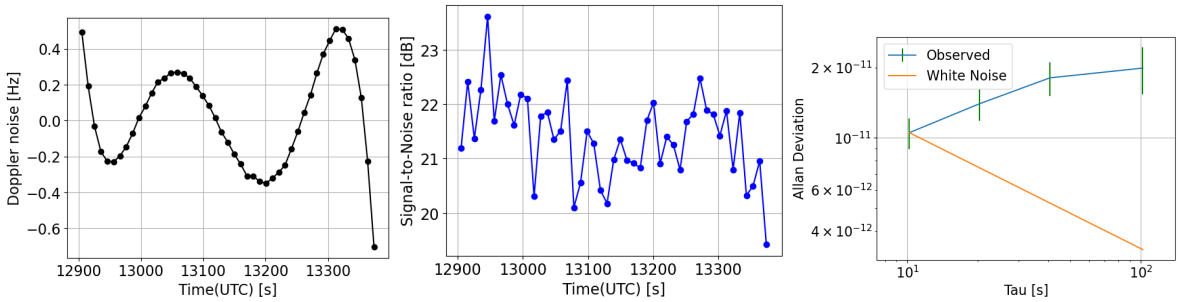

(a) Doppler noise as function of time. **(b)** Signal-to-noise ratio as function of time. **(c)** Modified Allan deviation.

Figure B.32: Real measurements observed from Onsala station at 03:35:05 UTC on the 21st of October 2020.

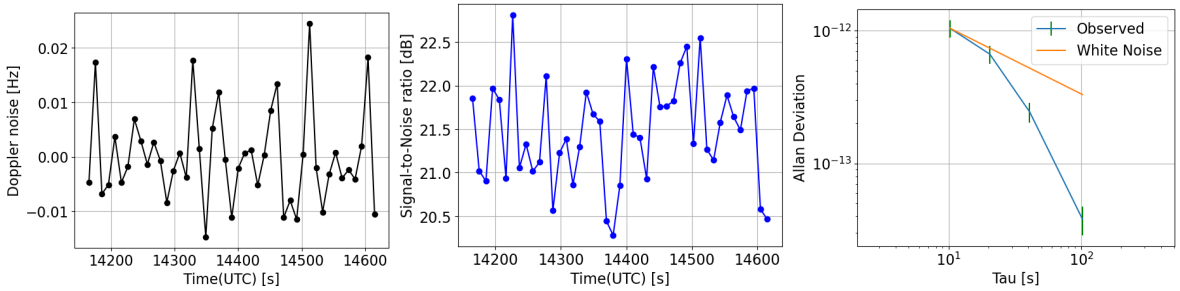

(a) Doppler noise as function of time. **(b)** Signal-to-noise ratio as function of time. **(c)** Modified Allan deviation.

Figure B.33: Real measurements observed from Onsala station at 03:56:05 UTC on the 22nd of October 2020.

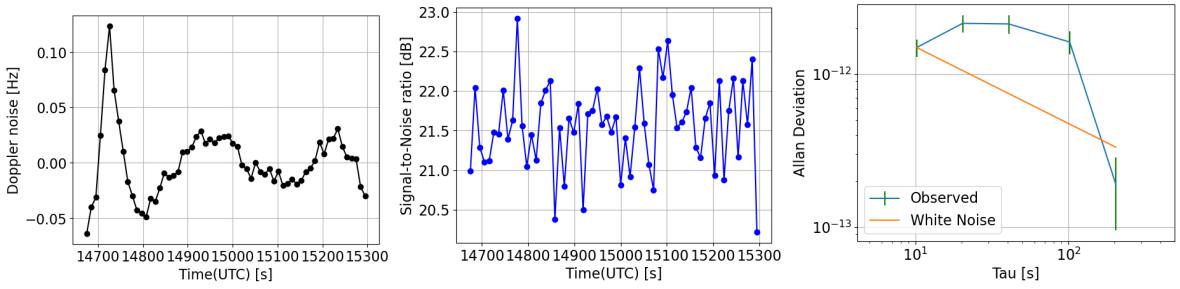

(a) Doppler noise as function of time. **(b)** Signal-to-noise ratio as function of time. **(c)** Modified Allan deviation.

Figure B.34: Real measurements observed from Onsala station at 04:04:35 UTC on the 22nd of October 2020.

B.3.8. TIANMA65

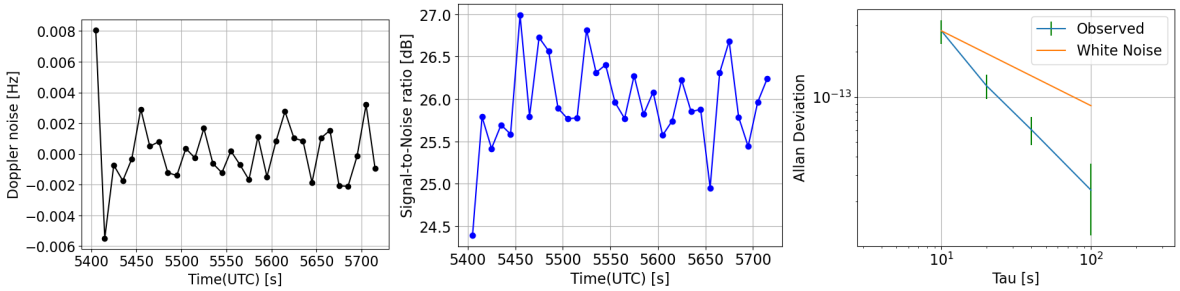

(a) Doppler noise as function of time. **(b)** Signal-to-noise ratio as function of time. **(c)** Modified Allan deviation.

Figure B.35: Real measurements observed from Tian Ma station at 01:30:05 UTC on the 22nd of October 2020.

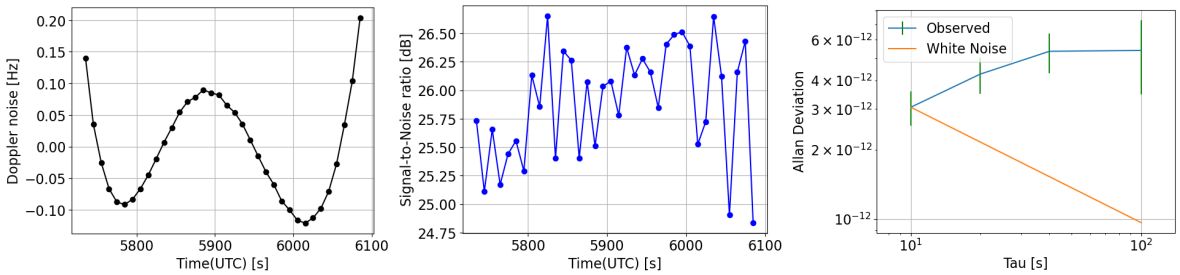

(a) Doppler noise as function of time. **(b)** Signal-to-noise ratio as function of time. **(c)** Modified Allan deviation.

Figure B.36: Real measurements observed from Tian Ma station at 01:35:05 UTC on the 22nd of October 2020.

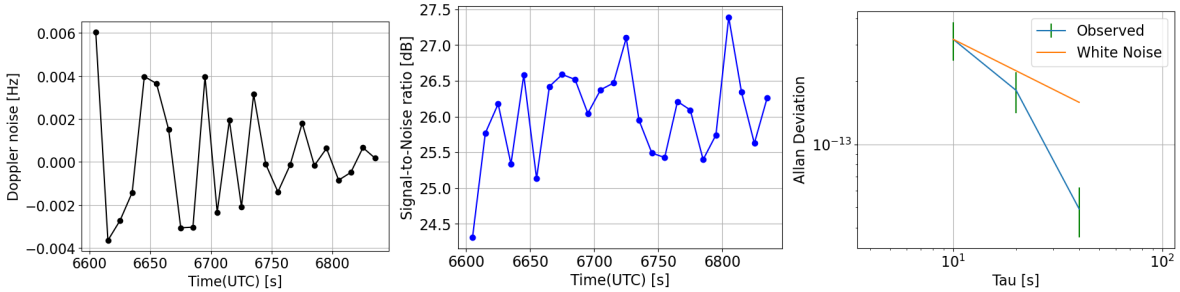

(a) Doppler noise as function of time. **(b)** Signal-to-noise ratio as function of time. **(c)** Modified Allan deviation.

Figure B.37: Real measurements observed from Tian Ma station at 01:50:05 UTC on the 22nd of October 2020.

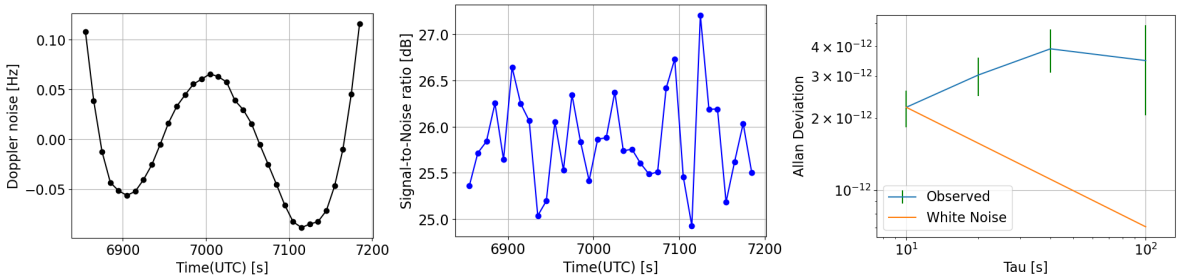

(a) Doppler noise as function of time. **(b)** Signal-to-noise ratio as function of time. **(c)** Modified Allan deviation.

Figure B.38: Real measurements observed from Tian Ma station at 01:54:15 UTC on the 22nd of October 2020.

B.3.9. WRT0

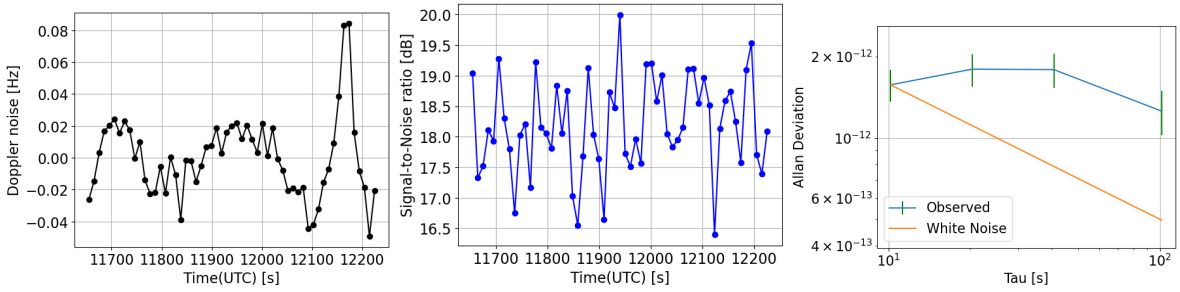

(a) Doppler noise as function of time. **(b)** Signal-to-noise ratio as function of time. **(c)** Modified Allan deviation.

Figure B.39: Real measurements observed from Dwingeloo station at 03:14:15 UTC on the 21st of October 2020.

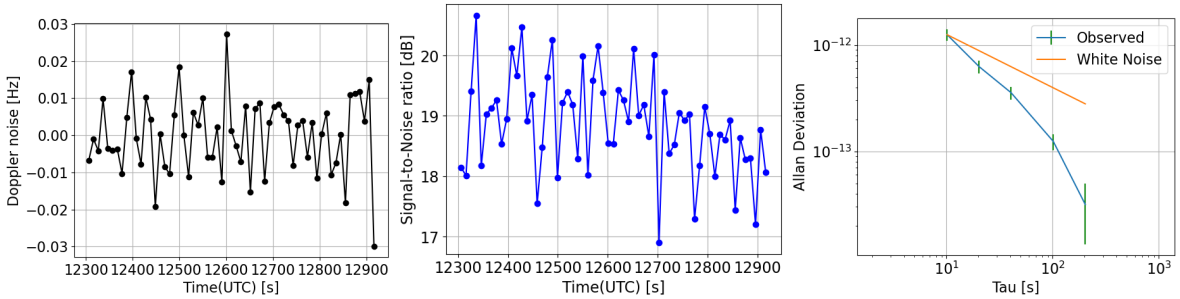

(a) Doppler noise as function of time. **(b)** Signal-to-noise ratio as function of time. **(c)** Modified Allan deviation.

Figure B.40: Real measurements observed from Dwingeloo station at 03:25:06 UTC on the 21st of October 2020.

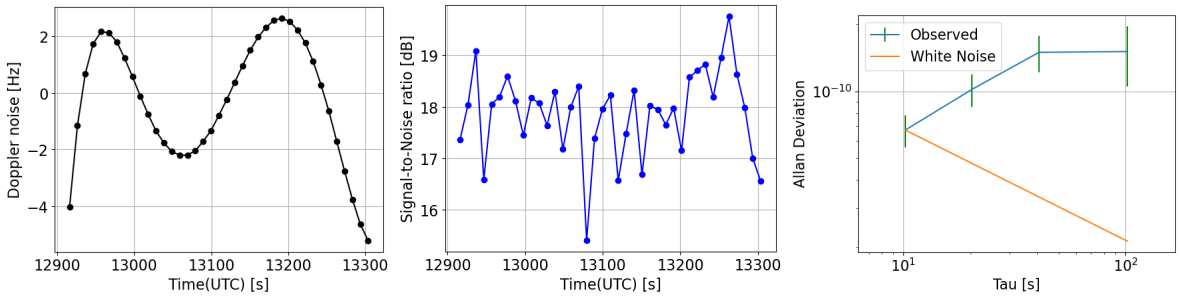

(a) Doppler noise as function of time. **(b)** Signal-to-noise ratio as function of time. **(c)** Modified Allan deviation.

Figure B.41: Real measurements observed from Dwingeloo station at 03:35:16 UTC on the 21st of October 2020.

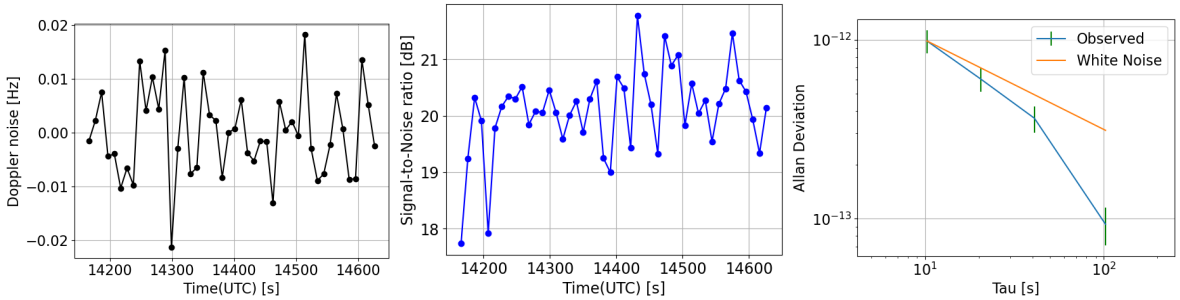

(a) Doppler noise as function of time. **(b)** Signal-to-noise ratio as function of time. **(c)** Modified Allan deviation.

Figure B.42: Real measurements observed from Dwingeloo station at 03:56:06 UTC on the 22nd of October 2020.

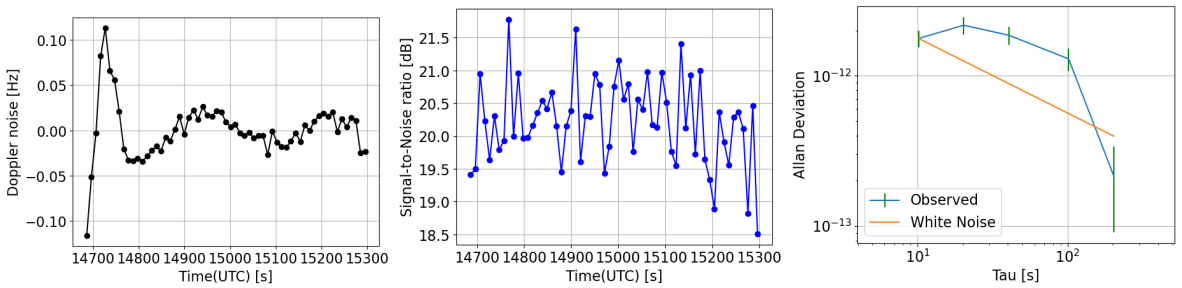

(a) Doppler noise as function of time. **(b)** Signal-to-noise ratio as function of time. **(c)** Modified Allan deviation.

Figure B.43: Real measurements observed from Dwingeloo station at 04:04:46 UTC on the 22nd of October 2020.

B.3.10. WETTZELL

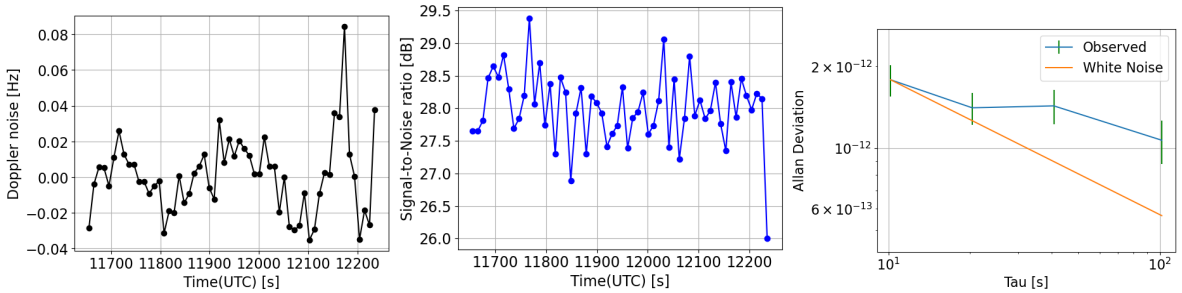

(a) Doppler noise as function of time. **(b)** Signal-to-noise ratio as function of time. **(c)** Modified Allan deviation.

Figure B.44: Real measurements observed from Wettzell station at 03:14:15 UTC on the 30th of May 2020.

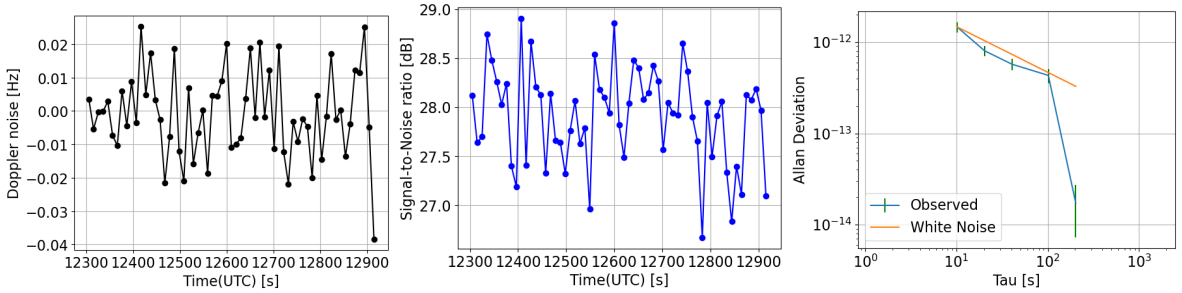

(a) Doppler noise as function of time. **(b)** Signal-to-noise ratio as function of time. **(c)** Modified Allan deviation.

Figure B.45: Real measurements observed from Wettzell station at 03:25:05 UTC on the 30th of May 2020.

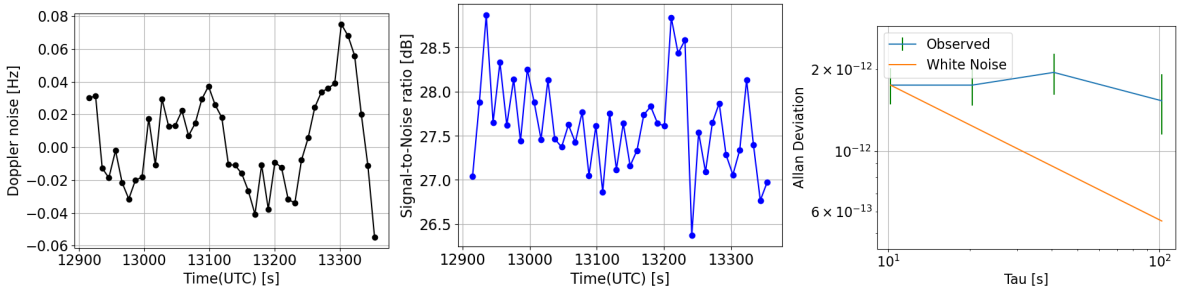

(a) Doppler noise as function of time. **(b)** Signal-to-noise ratio as function of time. **(c)** Modified Allan deviation.

Figure B.46: Real measurements observed from Wettzell station at 03:35:15 UTC on the 30th of May 2020.

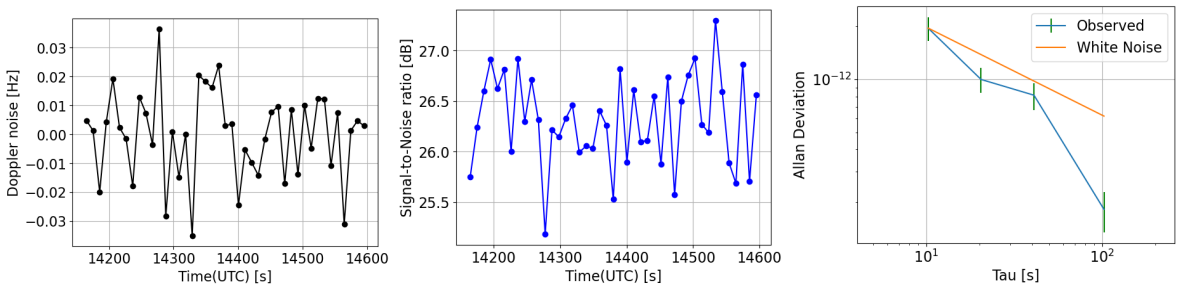

(a) Doppler noise as function of time. **(b)** Signal-to-noise ratio as function of time. **(c)** Modified Allan deviation.

Figure B.47: Real measurements observed from Wettzell station at 03:56:05 UTC on the 22nd of October 2020.

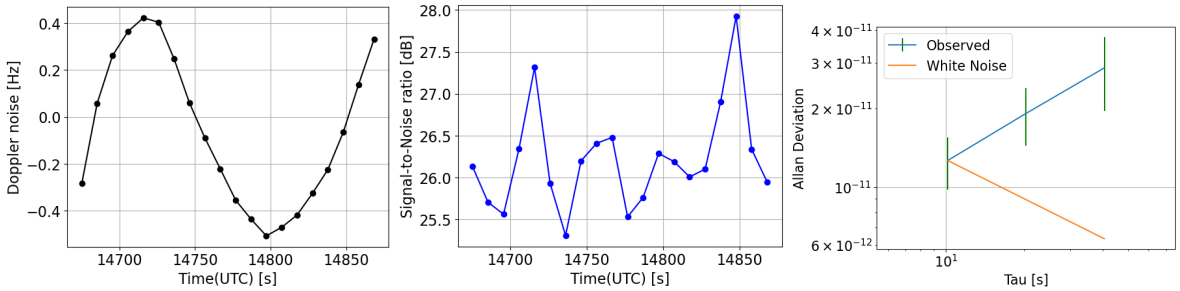

(a) Doppler noise as function of time. **(b)** Signal-to-noise ratio as function of time. **(c)** Modified Allan deviation.

Figure B.48: Real measurements observed from Wettzell station at 04:04:25 UTC on the 22nd of October 2020.

B.3.11. YEBES40M

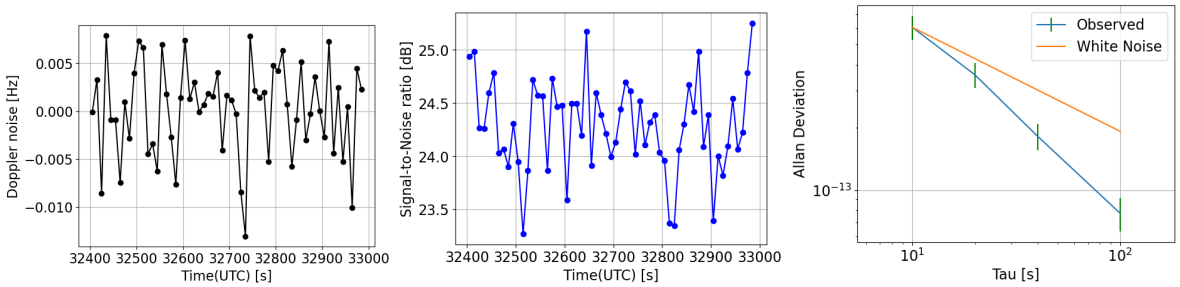

(a) Doppler noise as function of time. **(b)** Signal-to-noise ratio as function of time. **(c)** Modified Allan deviation.

Figure B.49: Real measurements observed from Yebes station at 09:00:05 UTC on the 29th of May 2020.

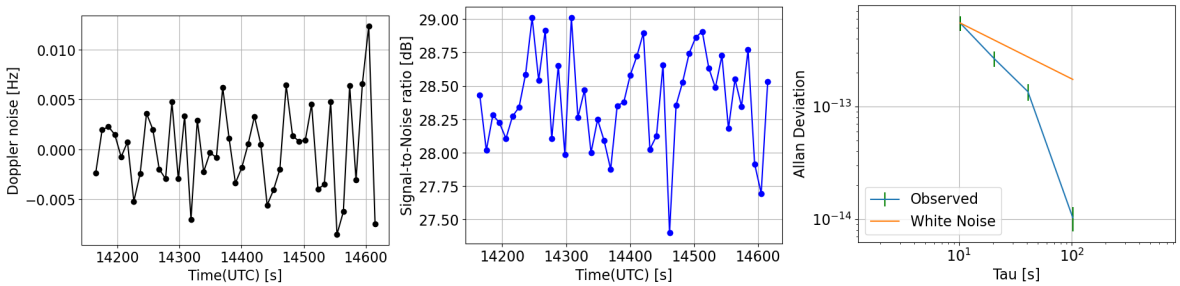

(a) Doppler noise as function of time. **(b)** Signal-to-noise ratio as function of time. **(c)** Modified Allan deviation.

Figure B.50: Real measurements observed from Yebes station at 03:56:05 UTC on the 22nd of October 2020.

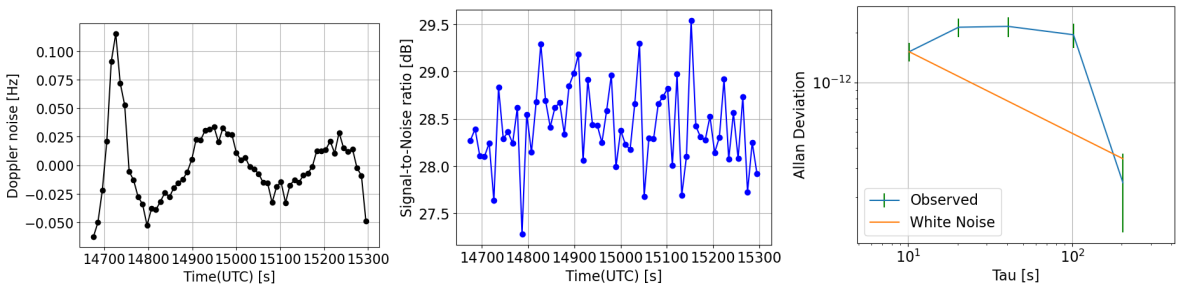

(a) Doppler noise as function of time. **(b)** Signal-to-noise ratio as function of time. **(c)** Modified Allan deviation.

Figure B.51: Real measurements observed from Yebes station at 04:04:35 UTC on the 22nd of October 2020.

C

TUDAT Implementations

In this appendix, the new lines of C++ code that have been developed are given here. The new TUDAT implementations have been pushed to the two main repositories of TUDAT[1] and are still in review for merging. Hopefully, these scripts are going to become available in the `develop` branch of TUDAT.

C.1. Maximum Elevation Angle Viability

The radio signal received by a tracking station cannot always be detected for all the elevation angles. This is because the station is pointing to a range of elevation angles where the signal power gain is the highest. This range of elevation angles is different between the RISE and LaRa instruments. The tracking for RISE is accomplished between 10° and 30° of elevation above the local horizon of the lander. Instead for LaRa, the observations are going to be detected between 35° and 45° of elevation (Peters et al. 2020). Fortunately, TUDAT has the functionality to insert visibility constraints to the tracking stations, also known as viability settings. A specific viability setting was missing in TUDAT, which was the maximum elevation angle viability function. Only the minimum elevation angle viability function was already defined in TUDAT.

For the maximum elevation angle viability function, six different files have been modified. The new implementations are shown with the red color in the below lines of code. In order to not copy the entire script file, the numbering on the left side is displayed.

C.1.1. `observationViabilityCalculator.h`

Inside the `ObservationViabilityType` enumeration, the `maximum_elevation_angle` has been added in the following way:

```
39 enum ObservationViabilityType
40 {
41 {
42    minimum_elevation_angle, //properties: no string, double = elevation angle
43    maximum_elevation_angle, //properties: no string, double = elevation angle
44    body_avoidance_angle,   //properties: string = body to avoid, double = avoidance angle
45    body_occultation        //properties: string = occulting body, no double
46 };
47 };
```

Then, a new C++ class, named `MaximumElevationAngleCalculator`, is built. This class allows to check whether an observation is possible based on the maximum elevation angle criterion as defined below:

```
166    std::shared_ptr< ground_stations::PointingAnglesCalculator > pointingAngleCalculator_;
167 };
168
169 //! Function to check whether an observation is possible based on maximum elevation angle criterion at one link end.
170 class MaximumElevationAngleCalculator: public ObservationViabilityCalculator
171 {
```

[1] https://github.com/tudat-team/tudat and https://github.com/tudat-team/tudatpy.

```
172 public:
173
174     //! Constructor.
175     /*!
176      * Constructor, takes a variable defining the geometry and the maximum elevation angle and current angle calculator.
177      * \param linkEndIndices Vector of indices denoting which combinations of entries from the linkEndIndices and
             linkEndTimes
178      * vectors to use for elevation angle calculator when isObservationViable is called. The second entry of the pair is
             the index
179      * of the target that is being observed from the ground station at which the elevation angle is check, the first
             entry is
180      * the index of the ground station at which the check is performed. From each entry of this vector, a vector is
             created for
181      * which the elevation angle is checked.
182      * \param maximumElevationAngle Minimum elevation angle that is allowed.
183      * \param pointingAngleCalculator Object to calculate pointing angles (elevation angle) at ground station
184      */
185     MaximumElevationAngleCalculator(
186             const std::vector< std::pair< int, int > > linkEndIndices,
187             const double maximumElevationAngle,
188             const std::shared_ptr< ground_stations::PointingAnglesCalculator > pointingAngleCalculator ):
189             linkEndIndices_( linkEndIndices ), maximumElevationAngle_( maximumElevationAngle ),
190             pointingAngleCalculator_( pointingAngleCalculator ){ }
191
192     //! Destructor
193     ~MaximumElevationAngleCalculator( ){ }
194
195     //! Function for determining whether the elevation angle at station is sufficient to allow observation.
196     /*!
197      * Function for determining whether the elevation angle at station is sufficient to allow observation. The input from
             which
198      * the viability of an observation is calculated are a vector of times and states of link ends involved in the
             observation.
199      * \param linkEndStates Vector of states of the link ends involved in the observation, in the order as provided by
             the of
200      * function computeObservationsAndLinkEndData of the associated ObservationModel.
201      * \param linkEndTimes Vector of times of the link ends involved in the observation, in the order as provided by the
             of
202      * function computeObservationsAndLinkEndData of the associated ObservationModel.
203      * \return True if observation is viable, false if not.
204      */
205     bool isObservationViable( const std::vector< Eigen::Vector6d >& linkEndStates,
206                               const std::vector< double >& linkEndTimes );
207 private:
208
209     //! Vector of indices denoting which combinations of entries of vectors are to be used in isObservationViable function
210     /*!
211      * Vector of indices denoting which combinations of entries from the linkEndIndices and linkEndTimes vectors to use
             for
212      * elevation angle calculator when isObservationViable is called. The second entry of the pair is the index of the
             target
213      * that is being observed from the ground station at which the elevation angle is check, the first entry is the index
             of the
214      * ground station at which the check is performed. From each entry of this vector, a vector is created for which the
215      * elevation angle is checked.
216      */
217     std::vector< std::pair< int, int > > linkEndIndices_;
218
219     //! Maximum elevation angle that is allowed.
220     double maximumElevationAngle_;
221
222     //! Object to calculate pointing angles (elevation angle) at ground station
223     std::shared_ptr< ground_stations::PointingAnglesCalculator > pointingAngleCalculator_;
224 };
225
226 double computeCosineBodyAvoidanceAngle( const Eigen::Vector3d& observingBody,
227                                         const Eigen::Vector3d& transmittingBody,
```

C.1.2. `createObservationViability.h`

Within the `ObservationViabilitySettings` class, there were two `ElevationAngleViabilitySettings` functions. In order to differentiate the maximum and minimum elevation angle viability settings, the functions for the minimum elevation angle viability setting have been renamed to `minimumElevationAngleViabilitySettings`. Additionally, two `maximumElevationAngleViabilitySettings` are created using the same structure as `minimumElevationAngleViabilitySettings`. This can be seen beneath:

```
87     double doubleParameter_;
88 };
89
```

```
inline std::vector< std::shared_ptr< ObservationViabilitySettings > > minimumElevationAngleViabilitySettings(
       const std::vector< std::pair< std::string, std::string > > associatedLinkEnds,
       const double elevationAngle )
{
   std::vector< std::shared_ptr< ObservationViabilitySettings > > viabilitySettingsList;
   for( unsigned int i = 0; i < associatedLinkEnds.size( ); i++ )
   {
       viabilitySettingsList.push_back(
                   std::make_shared< ObservationViabilitySettings >(
                   minimum_elevation_angle, associatedLinkEnds.at( i ), "", elevationAngle ) );
   }
   return viabilitySettingsList;
}

inline std::shared_ptr< ObservationViabilitySettings > minimumElevationAngleViabilitySettings(
       const std::pair< std::string, std::string > associatedLinkEnd,
       const double elevationAngle )
{
   return std::make_shared< ObservationViabilitySettings >(
          minimum_elevation_angle, associatedLinkEnd, "", elevationAngle );
}

inline std::vector< std::shared_ptr< ObservationViabilitySettings > > maximumElevationAngleViabilitySettings(
       const std::vector< std::pair< std::string, std::string > > associatedLinkEnds,
       const double elevationAngle )
{
   std::vector< std::shared_ptr< ObservationViabilitySettings > > viabilitySettingsList;
   for( unsigned int i = 0; i < associatedLinkEnds.size( ); i++ )
   {
       viabilitySettingsList.push_back(
             std::make_shared< ObservationViabilitySettings >(
                   maximum_elevation_angle, associatedLinkEnds.at( i ), "", elevationAngle ) );
   }
   return viabilitySettingsList;
}

inline std::shared_ptr< ObservationViabilitySettings > maximumElevationAngleViabilitySettings(
       const std::pair< std::string, std::string > associatedLinkEnd,
       const double elevationAngle )
{
   return std::make_shared< ObservationViabilitySettings >(
          maximum_elevation_angle, associatedLinkEnd, "", elevationAngle );
}

inline std::vector< std::shared_ptr< ObservationViabilitySettings > > bodyAvoidanceAngleViabilitySettings(
       const std::vector< std::pair< std::string, std::string > > associatedLinkEnds,
```

Moreover, the `createMaximumElevationAngleCalculator` function that creates the object to check if a maximum elevation angle condition is met for observation has been built as follows:

```
       const std::shared_ptr< ObservationViabilitySettings > observationViabilitySettings,
       const std::string& stationName );

//! Function to create an object to check if a maximum elevation angle condition is met for an observation
/*!
 * Function to create an object to check if a maximum elevation angle condition is met for an observation
 * \param bodies Map of body objects that constitutes the environment
 * \param linkEnds Link ends for which viability check object is to be made
 * \param observationType Type of observable for which viability check object is to be made
 * \param observationViabilitySettings Object that defines the settings for the creation of the viability check creation
 * (settings must be compatible with maximum elevation angle check). Ground station must ve specified by
 * associatedLinkEnd_.second in observationViabilitySettings.
 * \param stationName Name of the ground station for which calculator is to be computed (if no station is explicitly
      given in
 * observationViabilitySettings).
 * \return Object to check if a maximum elevation angle condition is met for an observation
 */
std::shared_ptr< MaximumElevationAngleCalculator > createMaximumElevationAngleCalculator(
       const simulation_setup::SystemOfBodies& bodies,
       const LinkEnds linkEnds,
       const ObservableType observationType,
       const std::shared_ptr< ObservationViabilitySettings > observationViabilitySettings,
       const std::string& stationName );

//! Function to create an object to check if a body avoidance angle condition is met for an observation
/*!
 * Function to create an object to check if a body avoidance angle condition is met for an observation
```

C.1.3. observationViabilityCalculator.cpp

A boolean function, named isObservationViable, for the MaximumElevationAngleCalculator class is developed. When the function returns True, it means that the observation is visible. The observation becomes not visible when the actual elevation angle is larger than the maximum elevation angle defined. The function is shown below:

```
73      return isObservationPossible;
74  }
75
76  //! Function for determining whether the elevation angle at station is sufficient to allow observation
77  bool MaximumElevationAngleCalculator::isObservationViable(
78          const std::vector< Eigen::Vector6d >& linkEndStates,
79          const std::vector< double >& linkEndTimes )
80  {
81      bool isObservationPossible = 1;
82
83      // Iterate over all sets of entries of input vector for which elvation angle is to be checked.
84      for( unsigned int i = 0; i < linkEndIndices_.size( ); i++ )
85      {
86          double elevationAngle = ground_stations::calculateGroundStationElevationAngle(
87                  pointingAngleCalculator_, linkEndStates, linkEndTimes, linkEndIndices_.at( i ) );
88
89          // Check if elevation angle criteria is met for current link.
90          if( elevationAngle > maximumElevationAngle_ )
91          {
92              isObservationPossible = false;
93          }
94      }
95
96      return isObservationPossible;
97  }
98
99  double computeCosineBodyAvoidanceAngle( const Eigen::Vector3d& observingBody,
100                                          const Eigen::Vector3d& transmittingBody,
101                                          const Eigen::Vector3d& bodyToAvoid )
```

C.1.4. createObservationViability.cpp

The header file (.h file) of createObservationViability.cpp has been also modified and their changes have been shown in Appendix C.1.2. The createMaximumElevationAngleCalculator function has been adjusted as well in the implementation file (.cpp file). This specific function creates an object to check if the constraint is met as seen here:

```
93      // Create check object
94      double minimumElevationAngle = observationViabilitySettings->getDoubleParameter( );
95      return std::make_shared< MinimumElevationAngleCalculator >(
96      getLinkStateAndTimeIndicesForLinkEnd(
97                  linkEnds,observationType, observationViabilitySettings->getAssociatedLinkEnd( ) ),
98              minimumElevationAngle, pointingAngleCalculator );
99  }
100
101 //! Function to create an object to check if a maximum elevation angle condition is met for an observation
102 std::shared_ptr< MaximumElevationAngleCalculator > createMaximumElevationAngleCalculator(
103         const simulation_setup::SystemOfBodies& bodies,
104         const LinkEnds linkEnds,
105         const ObservableType observationType,
106         const std::shared_ptr< ObservationViabilitySettings > observationViabilitySettings,
107         const std::string& stationName )
108 {
109     if( observationViabilitySettings->observationViabilityType_ != maximum_elevation_angle )
110     {
111         throw std::runtime_error( "Error when making maximum elevation angle calculator, inconsistent input" );
112     }
113
114     // If specific link end is specified
115     std::string groundStationNameToUse;
116     if( observationViabilitySettings->getAssociatedLinkEnd( ).second != "" )
117     {
118         groundStationNameToUse = observationViabilitySettings->getAssociatedLinkEnd( ).second;
119         if( groundStationNameToUse != stationName )
120         {
121             throw std::runtime_error( "Error when making maximum elevation angle calculator, inconsistent station input" );
122         }
123     }
124     else
125     {
```

```
126         groundStationNameToUse = stationName;
127     }
128
129     if( bodies.count( observationViabilitySettings->getAssociatedLinkEnd( ).first ) == 0 )
130     {
131         throw std::runtime_error( "Error when making maximum elevation angle calculator, body " +
132                                   observationViabilitySettings->getAssociatedLinkEnd( ).first + " not found." );
133     }
134
135     // Retrieve pointing angles calculator
136     std::shared_ptr< ground_stations::PointingAnglesCalculator > pointingAngleCalculator =
137             bodies.at( observationViabilitySettings->getAssociatedLinkEnd( ).first )->
138                     getGroundStation( groundStationNameToUse )->getPointingAnglesCalculator( );
139
140     // Create check object
141     double maximumElevationAngle = observationViabilitySettings->getDoubleParameter( );
142     return std::make_shared< MaximumElevationAngleCalculator >(
143             getLinkStateAndTimeIndicesForLinkEnd(
144                     linkEnds,observationType, observationViabilitySettings->getAssociatedLinkEnd( ) ),
145           maximumElevationAngle, pointingAngleCalculator );
146 }
```

When the maximum elevation angle viability setting (`maximum_elevation_angle` case) is utilized in the simulation, it is important to create a list of the ground station for which elevation angle check needs to be made. After this, each elevation angle is checked separately whether it met the maximum elevation angle criterion. The two vectors are defined below:

```
206                                 bodies, linkEnds, observationType, relevantObservationViabilitySettings.at( i ),
207                                  listOfGroundStations.at( j ) ) );
208                 }
209                 break;
210             }
211             case maximum_elevation_angle:
212             {
213                 // Create list of ground stations for which elevation angle check is to be made.
214                 std::vector< std::string > listOfGroundStations;
215                 for( LinkEnds::const_iterator linkEndIterator = linkEnds.begin( );
216                      linkEndIterator != linkEnds.end( ); linkEndIterator++ )
217                 {
218                     if( linkEndIterator->second.first == relevantObservationViabilitySettings.at( i
                            )->getAssociatedLinkEnd( ).first )
219                     {
220                         if( std::find( listOfGroundStations.begin( ), listOfGroundStations.end( ),
                                 linkEndIterator->second.second ) ==
221                             listOfGroundStations.end( ) )
222                         {
223                             listOfGroundStations.push_back( linkEndIterator->second.second );
224                         }
225                     }
226                 }
227
228                 // Create elevation angle check separately for eah ground station: check requires different pointing angles
                        calculator
229                 for( unsigned int j = 0; j < listOfGroundStations.size( ); j++ )
230                 {
231                     linkViabilityCalculators.push_back(
232                             createMaximumElevationAngleCalculator(
233                                 bodies, linkEnds, observationType, relevantObservationViabilitySettings.at( i ),
234                                 listOfGroundStations.at( j ) ) );
235                 }
236                 break;
237             }
238             case body_avoidance_angle:
239
240                 linkViabilityCalculators.push_back(
```

C.1.5. `unitTestObservationViabilityCalculators.cpp`

In order to build the unit test, the object of `maximumElevationCalculator` needs to be exposed with the functions defined in the previous subsections. The `maximumElevationCalculator` object is added in the following way:

```
108     std::shared_ptr< ObservationViabilityCalculator > minimumElevationCalculator =
109             std::make_shared< MinimumElevationAngleCalculator >(
110                 linkEndIndices, testAngle, pointingAngleCalculator );
111     std::shared_ptr< ObservationViabilityCalculator > maximumElevationCalculator =
112             std::make_shared< MaximumElevationAngleCalculator >(
```

```
                    linkEndIndices, testAngle, pointingAngleCalculator );
        std::shared_ptr< ObservationViabilityCalculator > bodyAvoidanceCalculator =
                std::make_shared< BodyAvoidanceAngleCalculator >(
                    linkEndIndices, testAngle, [=](const double){return testBodyState;}, "TestBody" );
```

After calling back the `MaximumElevationAngleCalculator` function, a unit test elevation angle is defined as follows:

```
            }
        }

        // Test elevation angle
        {
            double manualElevationAngle = mathematical_constants::PI / 2.0 -
                                          std::acos( manualGroundStationInertialPosition.normalized( ).dot(
                                                vectorToTarget.normalized( ) ) );

            // Compute viability and check against manual calculation
            bool isObservationViable = maximumElevationCalculator->isObservationViable(
                    linkEndStates, linkEndTimes );
            if( manualElevationAngle < testAngle )
            {
                BOOST_CHECK_EQUAL( isObservationViable, 1 );
            }
            else
            {
                BOOST_CHECK_EQUAL( isObservationViable, 0 );
            }
        }

        // Test avoidance angle
        {
            double manualAvoidanceAngle =
```

C.1.6. `expose_observation_setup.cpp`

All the previous scripts are inside the `tudat` folder. Since the simulation scripts are coded in PYTHON, exposure files are needed to call C++ functions from PYTHON. The exposure files are located in the `tudatpy` folder. The `maximum_elevation_angle` observation viability type is exposed as seen here:

```
  py::enum_< tom::ObservationViabilityType >(m, "ObservationViabilityType",
                                             get_docstring("ObservationViabilityType").c_str() )
          .value("minimum_elevation_angle", tom::ObservationViabilityType::minimum_elevation_angle )
          .value("maximum_elevation_angle", tom::ObservationViabilityType::maximum_elevation_angle )
          .value("body_avoidance_angle", tom::ObservationViabilityType::body_avoidance_angle )
          .value("body_occultation", tom::ObservationViabilityType::body_occultation )
          .export_values();
```

Moreover, the `elevation_angle_viability` function is renamed to `minimum_elevation_angle_viability`, and the `maximum_elevation_angle_viability` exposure is created as shown below:

```
            get_docstring("ObservationViabilityType").c_str() );


   m.def("minimum_elevation_angle_viability",
         py::overload_cast<
                const std::pair< std::string, std::string >,
                const double>(
                &tom::minimumElevationAngleViabilitySettings ),
         py::arg("link_end_id" ),
         py::arg("elevation_angle" ),
         get_docstring("elevation_angle_viability").c_str() );

   m.def("maximum_elevation_angle_viability",
         py::overload_cast<
                const std::pair< std::string, std::string >,
                const double>(
                &tom::maximumElevationAngleViabilitySettings ),
         py::arg("link_end_id" ),
         py::arg("elevation_angle" ),
         get_docstring("elevation_angle_viability").c_str() );
```

In case there are more than one link end, the exposure function for elevation angle viability is defined slightly different compared to the one for a single link end. When several link ends are utilized, the

exposure functions, `minimum_elevation_angle_viability_list` and `maximum_elevation_angle_viability_list`, are respectively built as seen beneath:

```
328         py::arg("occulting_body" ),
329         get_docstring("body_occultation_viability").c_str() );
330
331   m.def("minimum_elevation_angle_viability_list",
332         py::overload_cast<
333         const std::vector< std::pair< std::string, std::string > >,
334         const double >(
335         &tom::minimumElevationAngleViabilitySettings ),
336         py::arg("link_end_ids" ),
337         py::arg("elevation_angle" ),
338         get_docstring("elevation_angle_viability_list").c_str() );
339
340
341    m.def("maximum_elevation_angle_viability_list",
342         py::overload_cast<
343         const std::vector< std::pair< std::string, std::string > >,
344         const double >(
345         &tom::maximumElevationAngleViabilitySettings ),
346         py::arg("link_end_ids" ),
347         py::arg("elevation_angle" ),
348         get_docstring("elevation_angle_viability_list").c_str() );
```